Study of Rheological and Sintering Behavior of Iron-based Feedstock Used in Low-pressure Metal Injection Molding

by

Atefeh AYATOLLAHI TAFTI

MANUSCRIPT-BASED THESIS PRESENTED TO ÉCOLE DE TECHNOLOGIE SUPÉRIEURE IN PARTIAL FULFILLEMENT FOR THE DEGREE OF DOCTOR OF PHILOSOPHY
Ph.D.

MONTREAL, 12 FEBRUARY 2023

ÉCOLE DE TECHNOLOGIE SUPÉRIEURE
UNIVERSITÉ DU QUÉBEC

BOARD OF EXAMINERS (THESIS PH.D.)

THIS THESIS HAS BEEN EVALUATED

BY THE FOLLOWING BOARD OF EXAMINERS

Mr. Vincent Demers, Thesis Supervisor
Department of Mechanical Engineering, École de Technologie Supérieure

Mr. Vladimir Brailovski, Thesis Co-supervisor
Department of Mechanical Engineering, École de Technologie Supérieure

Mr. Handy Fortin Blanchette, President of the Board of Examiners
Department of Electric Engineering, École de technologie supérieure

Ms. Nicole R. Demarquette, Member of the jury
Department of Mechanical Engineering, École de technologie supérieure

Mr. Carl Blais, External jury member
Department of Mining, Metallurgical and Materials Engineering, Laval University

THIS THESIS WAS PRESENTED AND DEFENDED

IN THE PRESENCE OF A BOARD OF EXAMINERS AND PUBLIC

26 JANUARY 2023

AT ÉCOLE DE TECHNOLOGIE SUPÉRIEURE

ACKNOWLEDGMENT

Professor Vincent Demers, thank you very much for supporting and guiding me during my studies. Through your trust, I was able to build not only my knowledge but also my confidence as a researcher. The lessons I've learned from you will stay with me throughout my career.

Professor Vladimir Brailovski, during my Ph.D., I had the privilege of having you as my co-supervisor. Thank you very much for your insightful remarks, constructive criticisms, and precise scientific suggestions.

Rio Tinto Metal Powders, the co-partner and sponsor of this project, made all of this happen. Thanks to Guillem Vachon and Danny Plamondon in particular.

I want to express my utmost gratitude and thanks to Etienne Moquin, Francis Ares, Lounes Ouarab, Raphaël Côté, Rémi Recoquille, Seyed Mohammad Majdi, and Mohsen Mokhtabad-Amrei for their invaluable assistance during this project as well as all of my great colleagues at LAMSI, particularly Salah Eddine Brika, Anatolie Timercan, William Turnier, and Linh-Aurore Le Bras. Thank you all.

Without the technical support of Radu Romanica, Nabil Mazeghrane, Serge Plamondon, and Simon Laflamme, this project would not have been possible.

In addition, I wish to thank my amazing friends Nastaran Cheshmehkaboodi, Neda Mohammadian, and Farzaneh Vali Ghazvini, with whom I shared all that we were going through with laughter and hugs. Without you, I couldn't have done it.

To my beloved mother, father, sister, and brothers who have never wavered in their love for me.
دوستتون دارم.

To my Mom and Dad in my new home, Liz and Bob Merry, your unending love and support is why.

This thesis is dedicated to my best friend and the love of my life, Baxter, as a token of my appreciation and gratitude for all the love, support, understanding, and patience he has shown me during the time I was completely devoted to my studies.

Étude du comportement rhéologique et de frittage des mélanges à base de fer utilisées dans le moulage par injection des poudres métalliques à basse pression

Atefeh AYATOLLAHI TAFTI

RÉSUMÉ

Ce projet de recherche étudie la possibilité de produire des pièces moulées par injection des poudres métalliques (PIM) à faible coût à partir de poudres irrégulières à base de fer produites par la compagnie Rio Tinto Poudres Métalliques. Principalement des poudres de fer atomisées à l'eau avec différentes conditions de post-traitement (broyage, tamisage et recuit), compositions chimiques et tailles de particules ont été premièrement testées pour définir leur possibilité de produire des mélanges fluides. L'approche de moulage par injection à basse pression des poudre (LPIM) a été utilisée pour formuler un mélange possédant un chargement solide maximale. La meilleure poudre en termes de fluidité (c'est-à-dire une poudre non recuite de -45 µm) a été sélectionnée pour étudier l'effet de chaque constituent polymérique sur les propriétés rhéologiques du mélange, évaluer l'interaction poudre/liant, obtenir la meilleure formulation de liant et identifier le chargement solide le plus élevé (58 vol. %) de cette poudre. De plus, pour concevoir le cycle de déliantage (c'est-à-dire le déliantage thermique par média mèche) et définir la température de préfrittage (c'est-à-dire 600°C), la même poudre avec une formulation de liant optimale (c'est-à-dire 1 vol. % d'acide stéarique comme agent tensioactif, 2 vol. % d'éthylène-acétate de vinyle en tant qu'agent épaississant, 2 vol. % de cire de carnauba en tant qu'agent de rétrécissement et de la cire de paraffine (balance) en tant que support principal) ont été utilisés pour préparer le mélange pour l'injection des échantillons. Enfin, pour évaluer l'effet de la taille des particules et du niveau d'impuretés sur la moulabilité, la déliantabilité et la frittabilité des poudres de fer irrégulières, trois poudres, dont -45 µm (325 mesh), -25 µm (500 mesh) et -10 µm (1200 mesh), ont été utilisés. Les résultats ont révélé que les mélanges préparés à partir de ces trois poudres pouvaient atteindre une fluidité appropriée. De plus, les valeurs de densité, les propriétés mécaniques et la composition finale des pièces PIM produites à partir des mélanges formulés de poudre de -10 µm confirment que cette poudre est une alternative raisonnable aux poudres de fer disponibles dans le commerce en PIM.

Mots-clés : moulage par injection de poudre (PIM), moulage par injection de poudre à basse pression (LPIM), viscosité à l'état fondu, aptitude au moulage, poudre irrégulière, poudre à base de fer, déliantage thermique par média mèche, température de préfrittage, frittage, propriétés mécaniques

Study of Rheological and Sintering Behavior of Iron-Based Feedstock Used in Low-Pressure Metal Injection Molding

Atefeh AYATOLLAHI TAFTI

ABSTRACT

This research project investigates the possibility of producing low-cost petal injection molding (PIM) parts from irregular iron-based powders produced by Rio Tinto Metal Powders Company. Mainly water-atomized iron powders with different post-processing conditions (milling, sieving, and annealing), chemical compositions, and particle sizes were primarily tested based on the possibility of producing flowable feedstocks. The low-pressure powder injection molding (LPIM) approach was employed to formulate feedstock with maximum workable solid loading. The best powder in terms of flowability (i.e., unannealed -45 μm powder) was selected to study the effect of each binder ingredient on feedstock rheological properties, evaluate powder/binder interaction, achieve the best binder formulation, and identify the highest solid loading (58 vol. %) of this powder. Furthermore, to design the debinding cycle (i.e., wick thermal debinding) and define the presintering temperature (i.e., 600ºC), the same powder with optimal binder formulation (i.e., 1 vol. % stearic acid as a surfactant, 2 vol. % ethylene-vinyl acetate as a thickening agent, 2 vol. % carnauba wax as a shrinking agent, and paraffin wax (balance) as the main carrier) was used to prepare the feedstock for injecting test specimens. Finally, to evaluate the effect of particle size and impurity level on the moldability, debindability, and sinterability of irregular iron powders, three powders, including -45 μm (325 mesh), -25 μm (500 mesh), and -10 μm (1200 mesh), were used. The results revealed that feedstocks prepared from these three powders could achieve suitable flowability. Furthermore, the density values, mechanical properties, and final composition of PIM parts produced from feedstock prepared from -10 μm powder confirm that this powder is a reasonable alternative for commercially available iron powders in PIM.

Keywords: Powder injection molding (PIM), low-pressure powder injection molding (LPIM), melt viscosity, moldability, irregular powder, iron-based powder, thermal wick-debinding, pre-sintering temperature, sintering, mechanical properties

TABLE OF CONTENTS

LIST OF TABLES

Page

LIST OF FIGURES

Page

XX

LIST OF ABREVIATIONS

RTMP	Rio Tinto Metal Powders
PIM	Powder Injection Molding
MIM	Metal Injection Molding
CIM	Ceramic Injection Molding
LPIM	Low-Pressure Powder Injection Molding
HPIM	High-Pressure Powder Injection Molding
AM	Additive manufacturing
PW	Paraffin Wax
CW	Carnauba Wax
SA	Stearic Acid
EVA	Ethylene-vinyl Acetate
DSC	Differential Scanning Calorimetry
TGA	Thermogravimetric Analysis
SEM	Scanning Electron Microscope
vol. %	Volume percentage
wt. %	Weight percentage

LIST OF SYMBOLS

α_{STV}	Moldability index with sensitivity to shear rate, temperature, and viscosity
$\dot{\gamma}$	Shear rate (s^{-1})
η_{ref}	Reference viscosity (Pa·s)
ρ	Density (g/cm^3)
T	Temperature (°C)
n	Shear rate sensitivity
R	Gas constant (J/mol.K)
E	Flow activation energy (kJ/mol)
T_m	Melting temperature (°C)
V_S	Sample volume (cm^3)
V_C	Volume of calibrated sample cell (cm^3)
V_E	Volume of calibrated expansion cell (cm^3)
m	Mass (g)
ρ_A	Apparent density (g/cm^3)
d_{eq}	Equivalent diameter (μm).

INTRODUCTION

Owned by Rio Tinto Company, one of the largest minerals and metals companies operating in 40 countries worldwide, Rio Tinto Metal Powders (RTMP), formerly QMP, is a major iron and steel powder producer for the powder metallurgy industry. RTMP's water-atomized iron powder is a cost-effective and high-compressibility powder initially designed for high-density and high-strength press & sinter (i.e., conventional powder metallurgy) applications. However, with advanced processing techniques such as powder injection molding (PIM) and additive manufacturing (AM), the development of tailored powder specifications seems crucial for commercial expansion and adjusting the demand of this new market. Therefore, this thesis synthesis of a Ph.D. project carried out within the Memory Alloys and Intelligent Systems Laboratory (LAMSI) and Advanced Manufacturing Optimization Laboratory (LOPFA) at École de technologie supérieure (ÉTS) in partnership with RTMP to develop new powders and explore the manufacturability of iron powder for PIM technology.

The PIM technology combines the idea of plastic injection molding to fabricate complex shape components with the advantages of conventional powder metallurgy, offering high production volume with precise dimensions in the medical, automotive, and aerospace industries. The four major processing steps involve feedstock formulation, injection molding, debinding, and sintering. First, the metallic or ceramic powder is mixed with different thermoplastic polymers in a molten state to form a particle-filled polymeric matrix called feedstock. The molten feedstock is then injection molded into the mold cavity at a certain temperature and pressure to form the green part. Following its solidification, this green part is ejected from the mold, debound, and finally sintered to form the final metallic or ceramic part exhibiting the required density and mechanical properties. Depending on the feedstock formulation (i.e., proportion and characteristics of the polymeric binder mixture and powders), the feedstock viscosity defines both the injection molding parameters (temperature, pressure, and flow) and the debinding routes (media, temperature, and atmosphere) being used afterward. The objective of this study was to evaluate the manufacturability of metallic parts from the irregular iron-based

powders in terms of their moldability, debindability, and sinterability using an innovative low-pressure PIM approach.

A literature review will be the subject of the first chapter of this document, where different categories of the PIM process will be described and detailed. In addition, the powder specifications and their effect on different stages of the PIM process will be highlighted. Specifically, the existing achievements in applying irregular metal powders in PIM processing technology and PIM approaches for manufacturing metallic parts using iron powders are the basis for formulating the research problem that is the subject of the second chapter of this thesis. The third chapter details the methodology followed during this project while exposing the research approach, equipment, and characterization methods. The fourth to sixth chapters then establish three journal articles presenting the characterization of feedstock and its moldability, debindability, and sinterability. Finally, the last sections present the project's main conclusions and propose research recommendations for future works.

CHAPTER 1

LITERATURE REVIEW

The literature review presented in this chapter covers the state-of-the-art in manufacturing near net-shape metal parts using the low-pressure powder injection molding (LPIM) technique from moldability and sinterability points of view. The chapter begins with an overview of different sub-processing steps in powder injection molding (PIM) technology, where specific aspects regarding the feedstock formulation, injection, debinding, and sintering of metallic powders are detailed and followed by a brief comparison between the low- and high-pressure powder injection molding approaches, The following sections focus on the PIM of iron-based powders and the processability of irregular powders for LPIM application. Finally, recent works using irregular iron powders are reviewed and analyzed to define the basis required to formulate problems in the rapid fabrication of metallic parts from irregular iron-based powders via LPIM.

1.1 Overview of powder injection molding

Powder injection molding (PIM) is a cost-effective manufacturing technique that uses the concept of injection molding of plastic to form high-performance ceramic or metal parts in large and small production volume with high geometrical intricacy, dimensional precision without extensive machining in most cases, and outstanding mechanical properties compared to other conventional processing techniques (German & Bose, 1997). Figure 1.1 shows the different steps of PIM processing technology. In ceramic injection molding (CIM) and metal injection molding (MIM), as two main subcategories of PIM, ceramic or metallic powders are mixed with a polymeric binder to form a homogeneous powder/polymer mixture called feedstock (Figure 1.1a). The feedstock is then injected into the mold cavity at suitable injection pressure and temperature using a modified plastic injection-molding machine for injecting feedstock to form a green body (Figure 1.1b).

Following the injection and part ejection, the binder components need to be removed during the debinding process, where one of the main challenges is removing the binder without losing

the dimensional integrity of the green part. Therefore, only one or a combination of several techniques consisting of catalytic, solvent, or thermal debinding is used depending on the binder's nature and debinding rates (Figure 1.1c). The debound part, also called the brown part, is finally sintered at elevated temperatures under protective conditions to obtain a dense part typically > 95 % of the theoretical density, along with an excellent surface finish and tight tolerance (Figure 1.1d) (Dehghan-Manshadi, Bermingham, Dargusch, StJohn, & Qian, 2017; German & Bose, 1997; Gonçalves, 2001; González-gutiérrez, Beulke Stringari, Emri, Stringari, & Emri, 2012; Hamidi et al., 2017; Kang et al., 2012). During sintering, a shrinkage of about 15%–25% is expected. Although PIM is generally suitable for all shapes, the technique has some considerations in section thickness and is limited to relatively small dimensions. On the one hand, the thin sections (< 0.25 mm) may cause molding difficulties due to rapid cooling in the mold. On the other hand, since the binder removal rate is proportional to the square of the section thickness, most thicknesses are limited to under 25 mm with a total component volume below 100 cm^3 (Rak & Z. S. Rak, 1999).

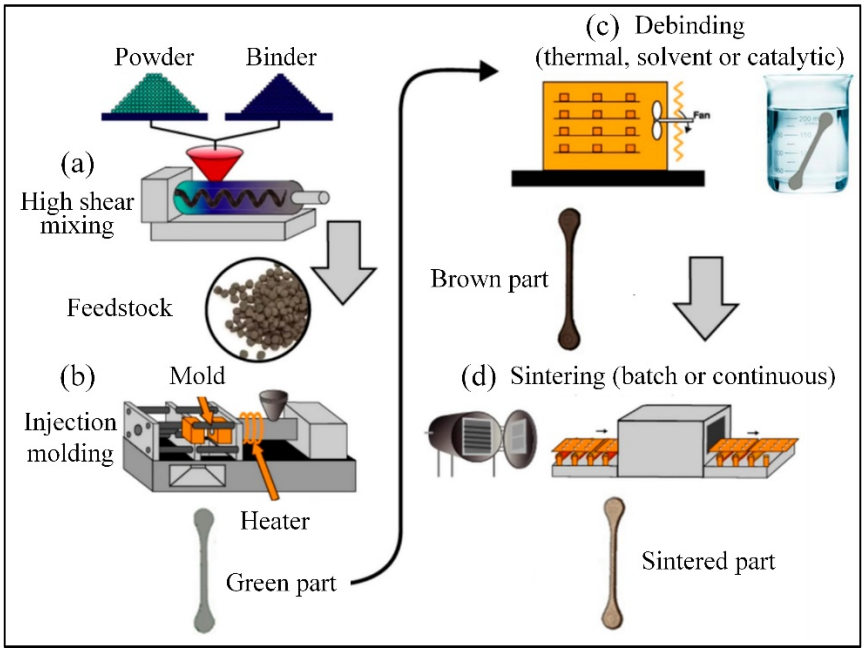

Figure 1.1 Steps of powder injection molding (PIM) technique
Taken from Neto et al. (2022)

1.1.1 Feedstock formulation and mixing

Feedstock formulations depend greatly on subtle factors such as powder and binder availability, mixing technology, powder-binder ratio, molding temperature, desired green strength, debinding technologies, sintering practices, and final properties. However, the key features and elements to consider are well established and documented by many research groups that can be the basis for developing new feedstocks. Some of those best practices are detailed in this section.

Metal powders

Even though many considerations regarding feedstock formulation and molding properties need to be considered to produce "a defect-free" green part, one should not underestimate the effect of powder characteristics coming directly from particles that are the smallest powder units that can no longer be subdivided by simple mechanical means. Powder bulk properties such as packing density and discrete attributes such as particle shape and size are parameters governing the fundamental aspect of a PIM process, such as critical solid loading, feedstock molding capability, and powder sinterability. In addition, the powder's physical characteristics themselves originate from the powder production routes.

Table 1-1 Powder attributes affecting PIM processing stages

PIM stage	**Physical and chemical properties**	**Powder attributes**
Mixing	Feedstock's rheological behavior, optimal solid loading, and homogeneity	Particle shape, size, size distribution, surface area
Molding	Feedstock's flowability	Particle shape and size
Debinding	Debinding rate and chemical composition of brown metallic part	Particle shape, size, and chemical composition
Sintering	Sintering rate, densification, mechanical properties, and chemical composition of sintered metallic part	Particle shape, size, size distribution, packing density, and chemical composition

Various powder characteristics influencing different stages of the PIM process are summarized in Table 1-1. For instance, from the molding perspective, the feedstock flowability is directly related to the particles' morphology and size. Ideally, the PIM of metals is realized with spherical and fine (< 20 μm) powders. Nonetheless, mainly to reduce the cost, irregular and coarse powders are of interest that could redefine the choices of binder, molding conditions, and debinding parameters.

Production of metallic powders for PIM process

Depending on the final part requirements, the metal powders produced by diverse production techniques can be potentially used in PIM technology. However, the production route can directly affect the raw material cost and powder features, such as impurity level, particle morphology, and size, which are significant considerations when selecting powders for PIM. Major powder production techniques, suitable metals, and powder size and morphology are summarized in Table 1-2 for different fabrication approaches (D. F. Heaney, 2019).

Table 1-2 Powder production techniques and attributes

Manufacturing method	Production cost	Particle size (μm)	Particle shape	Examples
Gas atomization	High	5-45	Spherical	Stainless steels, superalloys, titanium alloys, master alloy additives
Water atomization	Moderate	5-45	Semi-spherical/ irregular	Stainless steels, superalloys, master alloy additives
Plasma atomization	High	10-85	Spherical	Titanium and titanium alloys, nickel, zirconium, niobium, and tantalum.
Thermal decomposition	Moderate	0.2-20	Spherical, spiky	Iron, nickel
Chemical reduction	High/moderate	0.1-10	Angular, spherical	Tungsten, molybdenum

Figure 1.2a-c presents the schematic of different atomization techniques. Water and gas atomized powders are produced by forcing the molten metal or alloy through a nozzle where it is struck by high-pressure water (> 100 MPa) or powerful atomization gas (~ 0.5 - 4 MPa) after leaving the nozzle that breaks the molten ligament into fine droplets. Plasma atomization, on the other hand, uses argon plasma torches to atomize the metal wire (instead of the melt stream) into fine droplets. An example of the morphology of powders produced by these different atomization techniques is shown in Figure 1.2d-f, where the water-atomized powder is mostly irregular in shape, while gas and plasma-atomized powders are spherical. Generally, spherical powders are suitable in PIM due to their high packing density, which can be translated into high powder loading, lower binder content, and less shrinkage during the final sintering process. In counterpart, such kind of spherical powders are generally more expensive than the one produced by water atomization. In this respect and as water atomization is the core technology used for producing powders in this project's framework, specific details on this production technique is provided in the next section.

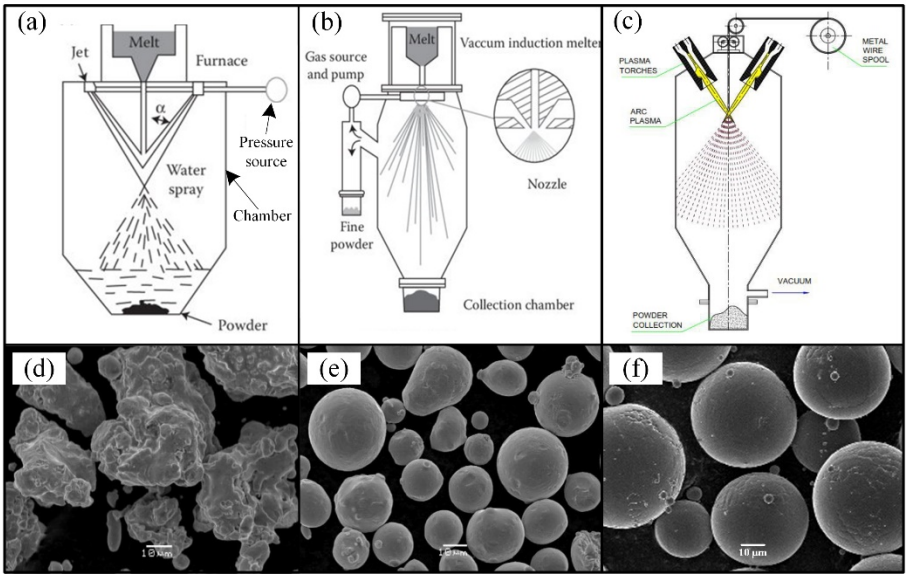

Figure 1.2 (a-c) Water, gas, and plasma atomization techniques for metal powder production, (d-f) water, gas, and plasma atomized powders morphology
Taken from Chen et al. (2018), Habibnejad-korayem, Zhang, & Zou (2021), and Wallner (2019)

Water atomized powders

Due to the high cooling rates and delayed spheroidization associated with the water strike, water-atomized powders tend to be irregular shape particles with an average particle size of < 45 μm (González-gutiérrez, Stringari, & Emri, 2012). As a result, coming directly from the fabrication route, the shape irregularity, specifically as the particle size increases, and a high level of impurity in the form of oxygen content as the particle size decreases are some of the main drawbacks of the water-atomized powders. Generally, high oxygen content comes from three main sources; (1) entrapped oxygen inside the particles during the rapid solidification that forms dissolved oxides, (2) discrete oxides initially present or form during the atomization in the composition that could create scattered oxide inclusions inside the particles or as fully oxidized particles, and (3) surface oxidation due to the interaction of water vapor with the melt during atomization that covers the entire particle's surface completely or partially formed oxide lump (Hariramabadran Anantha, 2012). Normally, surface oxidation contributes the most to the total powder oxygen content. Therefore, the efficient removal of oxides through the annealing process is the main concern since the surface oxide layer is considered a limiting factor for maintaining uniform interaction with polymers in the feedstock.

On the other hand, surface oxidation hinders the effective creation of sinter necks and full densification during sintering, which deteriorates the sintered part's mechanical properties. However, in some cases, the reduction of thermodynamically stable oxides (those rich in silicon, chromium, and manganese) is much harder during the annealing process. Therefore, the high oxygen content is a crucial issue for water-atomized powders that must be addressed and fully understood, specifically during the sintering of PIM parts. In addition, some research groups recently developed new techniques to decrease shape irregularity and increase the purity of water-atomized powders. For instance, Jie et al. (2018) developed an atomization apparatus that combines water atomization with the gas atomization technique that uses high-pressure (0.5 MPa) nitrogen gas and high-pressure (120 MPa) water to form the droplets to take advantage of both techniques. As a result, they produced spherical stainless steel powders with median particle diameters (D_{50}) between 8 and 13 μm. Besides, spheroidization of water-

atomized powders using different techniques is of interest to promote the powder packing density and flowability suitable for advanced manufacturing technologies (Bao, Yang, Wen, Guo, & Guo, 2021; Boisvert, Christopherson, Beaulieu, & L'Espérance, 2017). For instance, Park et al. (2020) used an inductively-coupled thermal plasma technique for the spheroidization of water-atomized 316L stainless steel powder. They confirmed that the spheroidization of this powder using a plasma power of 9 kW also reduced the average particle size and the oxygen concentration while the iron oxides in the powder completely disappeared. Despite efforts to improve irregular powder characteristics, using as-is water atomization remains one of the most common way to produce metal powder due to its high production rate and cost efficiency.

Binder systems

In PIM, a binder allows the shaping of metal or ceramic powders via injection molding and outlines the mixing, molding, and debinding processing practices. In addition, the binder governs the feedstock homogeneity, flowability, complete mold filling, and proper final burnout needed to achieve optimal part quality. Therefore, the binder systems essentially consist of different constituents; each plays a different role in the feedstock's quality. As schematically presented in Figure 1.3, different component of a conventional multi-component binder system is selected based on the sequences and practices during the debinding process.

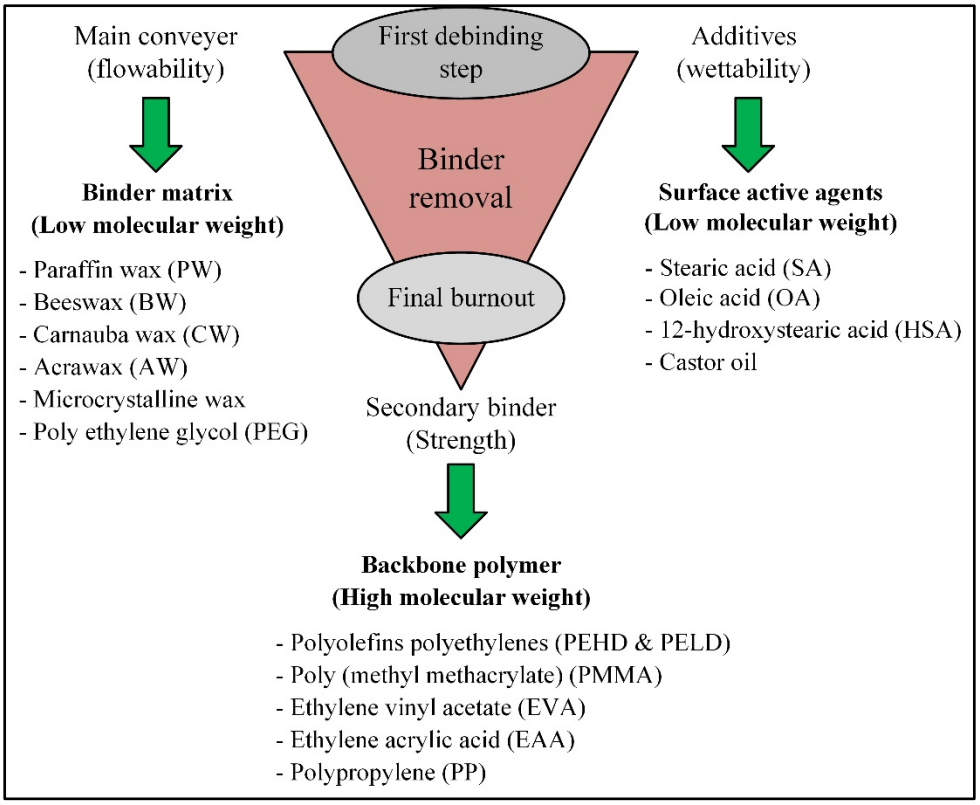

Figure 1.3 The main constituents of a binder system and example polymers

Generally, a typical binder system used in conventional PIM comprises a main carrier, a surface-active agent, and a backbone polymer. The primary binder or conveyer is responsible for the low viscosity of the feedstock, where paraffin wax (PW) is widely used in PIM as the main carrier due to low melting temperature (45-65°C). However, high PW content is improper due to its nonpolar nature, resulting in difficulties in dispersing the particles and de-agglomeration; consequently, risk of powder/binder separation at high shear rates and defective sintered part (Thomas-Vielma, Cervera, Levenfeld, & Várez, 2008). Therefore, recently water-soluble binders based on PEG have gained more interest in academic and industrial research. For instance, Hayat, Jadhav, Zhang, Ray, & Cao (2018) developed a new water-soluble binder system based on polyethylene glycol (PEG) as the main constituent for PIM of titanium powder. Another key component in a typical binder system is a surface-active agent. Surfactants such as stearic acid (SA) consist of a polar ester functional group adhering to the particle surface via dipole-dipole attractive forces and an oriented molecular chain

extending into the binder matrix. Therefore, by decreasing interparticle friction and enhancing the particles' dispersion in the binder, the addition of surfactant improves feedstock homogeneity during the mixing and decreases the viscosity, increasing the optimal solid loading. The last essential constituent in the binder system is a thermoplastic polymer, such as ethylene-based copolymers (e.g., ethylene vinyl acetate (EVA) and polypropylene (PP)) with high molecular weight and high melting point, which act as a backbone and enhance green strength. In addition, the backbone polymer remains in partially debound parts until the final burnout stage to hold particles together before the initial sintering stage.

It should be noted that while most of the conventional binder systems used in PIM consist of secondary binders as the main constituent, some are composed solely of waxes and additives and do not contain formally backbone polymers. In this case, the binder is removed in a single thermal cycle and pre-sintered at the same time to provide the part with adequate strength prior to the sintering process. This approach, which has extensively been used for CIM, has recently gained more research interest for the fabrication of MIM parts. Therefore, depending on the binder systems and from the injection perspective, the PIM process is divided into two main categories: low-pressure powder injection molding (LPIM) and high-pressure powder injection molding (HPIM) and as shown in Figure 1.4a-b, respectively.

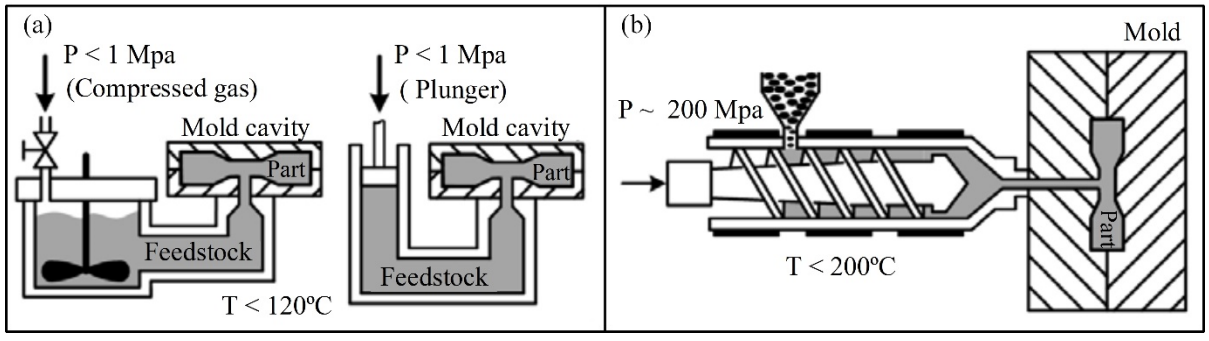

Figure 1.4 Comparison between (a) LPIM and (b) HPIM injection processes

1.1.2 Injection molding

From the molding perspective, although the core processing stages of HPIM and LPIM processes are similar, due to inherent differences in many aspects and real practices in binder formulation and feedstock characteristics, the molding and tooling in these two subcategories of PIM are entirely different. The main difference between these two processes originates from the pressure required during the injection operation. In the first case, the backbone binder used in HPIM (e.g., polyethylene and polypropylene) results in high feedstock viscosity, requiring an injection pressure of up to 200 MPa and temperature between 150 to 250ºC. In the second case, the low molecular weight binder used in LPIM (e.g., paraffin wax, beeswax, carnauba wax) produces a low-viscosity feedstock requiring an injection pressure below 1 MPa and a temperature range from 60 to 100ºC (Gonçalves, 2001).

Therefore, LPIM demonstrates considerable processing benefits compared to the conventional HPIM technology, including a decrease in injection equipment size as well as a decrease in tooling size, directly resulting in a cost-effective technology for producing small and complex shape parts, either in high or low production volumes (i.e., mass customization). However, the main drawback of the macro LPIM is the higher tendency of these feedstocks to the separation of the binder from the powder during the injection process, which deteriorates feedstock stability and can cause incomplete or heterogeneous mechanical properties in the sintered part (Gelin, Barriere, & Song, 2009; Rak & Z. S. Rak, 1999). It is important to mention that when the debinding process is completed, both PIM components might have similar sintering cycles depending on the characteristics of the powder used and the final desired mechanical properties. Table 1-3 summarizes the main parameters of the two processes.

Table 1-3 Comparison between LPIM & HPIM processes

Technology	**HPIM**	**LPIM**
Feedstock viscosity during injection (Pa·s)	< 1000	< 10
Injection temperature (ºC)	150 - 250	60 - 100
Maximum injection pressure (MPa)	200	< 1
Tool costs	High	Low
Tool wear	High	Low
Bum-out of binder (ºC)	>450	<250
Production volume	High	High and low
Segregation risk	Non	High

In PIM, moldability represents the capability of a molten feedstock to fill a mold cavity that should be assured before the injection molding process. Although many different properties, such as specific heat, thermal conductivity, and melt elasticity, can affect moldability, the most fundamental parameter governing the feedstock's behavior during injection molding is melt viscosity, where the lowest viscosity without the occurrence of binder/powder separation during the injection molding and risking the feedstock's homogeneity is always favorable for appropriate mold filling. However, the viscosity is highly affected by variations in shear deformation rate and temperature. Ideally, the feedstock viscosity should decrease quickly with an increasing shear rate during the injection required for producing complex and delicate parts. Also, the feedstock's viscosity should not be sensitive to small fluctuations in temperature that result in sudden viscosity changes. Consequently, different analyses need to be done on the molten feedstock to quantify the adequate molding properties directly linked to its rheological properties. Accordingly, during the rheological evaluation of any given feedstock, the effect of powder characteristics, binder formulation, and powder: binder ratio (defined as solid loading) on the combination of different parameters must be well understood.

Weir's moldability index (1963) as one of the tools that were initially developed to assess the molding properties of polymers is gathering different rheological parameters in one experimental model and has been extensively used to assess the moldability of ceramic- (Agote et al., 2001; Lenk & Krivoshchepov, 2004; Liu, 1999), composite- (Khakbiz, Simchi, & Bagheri, 2005), and metallic-based (Huang & Hsu, 2009) feedstocks as well. In weir's model,

the key rheological parameters concerning the feedstock's viscosity and flow behavior such as shear rate and temperature sensitivities are obtained experimentally to quantify optimized feedstock formulation and optimal solid loading. For example, Hausnerova, Mukund, & Sanetrnik (2017) used the Weir model to study the effect of powder particle size and shape on the moldability of stainless steel feedstocks. Also Claudel, Mohamed, Thierry, & Jean-Claude (2017) studied the effect of temperature on the moldability of Inconel feedstocks using the same methodology. The spiral flow test is another widely used tool to evaluate a feedstock's moldability through small-scale injections. Using this tool, it is possible to estimate the effect of feedstock's features, such as solid loading and injection parameters, such as mold temperature, injection pressure, and speed, on the moldability of a given feedstock.

Although it is possible to reduce the production cost using the LPIM technology, since the injection molding takes place at a much lower pressure and temperature than HPIM, the technique's application for manufacturing metallic parts is still relatively new and requires more research. Therefore, by developing low-viscosity feedstocks for injection at low pressures, this project emphasizes the LPIM approach.

1.1.3 Debinding process

In conventional HPIM, the binder is removed in two steps. First, more than 95% of the primary binder constituents (i.e., main carrier and surfactants) are removed at low temperatures by solvent extraction using n-Heptane (K. K. Rane & Date, 2020) or supercritical carbon dioxide (Royer, Barriere, & Bienvenu, 2018) or a catalyst such as highly concentrated nitric acid (Attia, Hauata, Walton, Annicchiarico, & Alcock, 2014), depending on the binder system and powder characteristics. Then, during a thermal debinding cycle, at higher temperatures (i.e., 400 to 650 ºC), the backbone polymer responsible for shape retention of the partially debound part is removed, and in some cases, the part is pre-sintered (up to 900 ºC) to provide enough brown strength prior to the sintering process or simply successively debound and pre-sintered using a continuous process (Hayat et al., 2018; J. M. Park et al., 2018). Figure 1.5a illustrates an example of the two-step solvent-thermal process for debinding iron-nickel-based green parts

(M. Ali et al., 2019). Figure 1.5a (i) shows the binder distribution consisting of PW, SA, and PP in the green body. First, during the solvent extraction, PW and SA from the part's surface dissolve into an n-heptane solution and toward the inner part due to the capillary forces leaving a network of fine pore channels, some traces of PW and SA, and unchanged PP. Then, as shown in Figure 1.5a (iii) and (iv), during the thermal debinding step, the decomposition of polypropylene at 600ºC for 120 min in an argon gas atmosphere completes. The most important consideration, specifically in the PIM of metal powders, is the binder removal, without leaving residue upon decomposition that can affect the final part's magnetic, electric, physical, and mechanical properties. Therefore, the debinding process must be carefully designed to minimize undesirable chemical reactions.

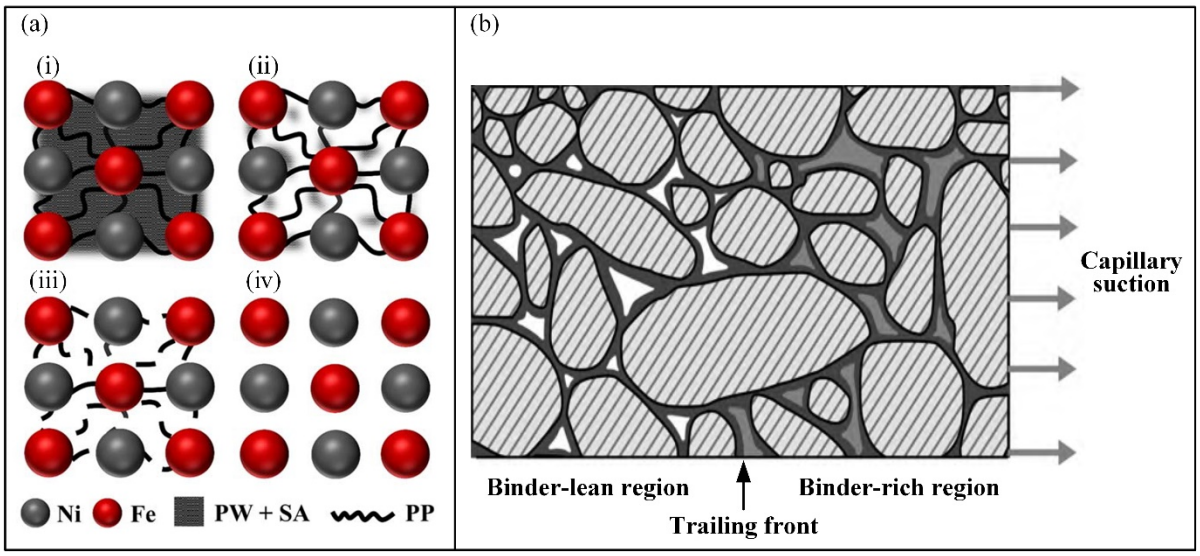

Figure 1.5 (a) Schematic illustration of two-step conventional binder removal; (i) before and (ii) after solvent debinding, (iii) during and (vi) after thermal debinding Taken from Ali et al. (2019), and (b) sketch of capillary suction in single-step wick thermal debinding debinding
Taken from Gorjan, Dakskobler, & kosmač (2010)

In LPIM, the debinding kinetic is different since the binder, which consists mainly of paraffin wax, is removed using single-step thermal debinding where in the absence of a backbone polymer that would hold the particles together, the debound part is extremely spongy and fragile. Therefore, one highly effective way to avoid the formation of defects and crack in the

brown part during the binder removal is using thermal wick-debinding to provide enough support. As pioneers, Bandyopadhyay and French (1993) used alumina and silicon nitride as two fine and coarse porous setters for thermal wick-debinding. Figure 1.5b illustrates the distribution of binder during a wick thermal debinding. In wick debinding, the mobile binder is extracted from the larger pores into the powder bed by capillary suction due to the pressure gradient and immobile binder that forms a thin film on the particles' surface that is removed during the final burnout stage creating two distinct regions inside the part during the debinding process (Gorjan et al., 2010). Although thermal wick-debinding is widely used in industrial settings for the fabrication of CIM parts, the details of the process have largely remained proprietary and have not been reported in the open literature. In addition, the performance or success indicators of this debinding approach for metallic part are simply absent from the scientific documentation. Therefore, developing this technique at ÉTS was one of the main objectives of this project.

1.1.4 Sintering and sintered part properties

Total interficial energy reduction is the main sintering driving force. that occurs via basic sintering phenomena namely densification and grain growth that are shown in Figure 1.6a. The total energy reduction ($\Delta(\gamma A)$) can be expressed as:

$$\Delta(\gamma A) = \Delta\gamma A + \gamma\Delta A \tag{1.1}$$

where γ is specific surface energy and A total interface area and as schematically presented in Figure 1.6a, the changes in γ is due to densification and in A due to grain coarsening. In fact, smaller size powder particles provide higher surface energy and higher densification (Fedorchenko & Skorokhod, 1967). Therefore, understanding of the mechanisms and variales involved in densification and grain growth is nessasary to obtain higher densities and enhanced mechanical properties.

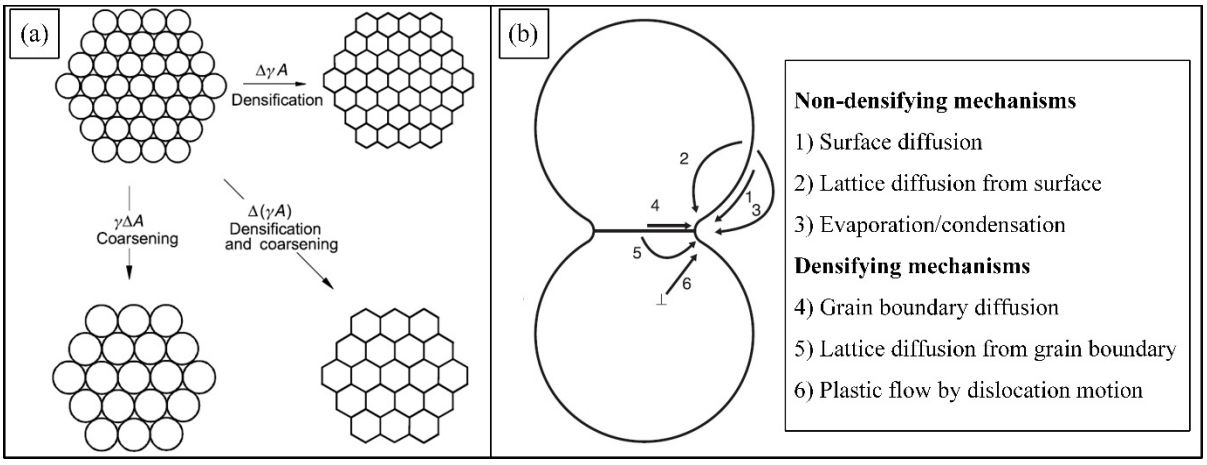

Figure 1.6 Schematic representation of (a) basic densification and coarsening phenomena occurring under the driving force for sintering
Taken from Kang et al (2008) and
(b) sintering non-densifying and densifying mechanisms
Taken from Rahaman (2010)

Figure 1.6b shows six different mass transportation mechanisms for a two particle model from which grain boundary diffusion, lattice diffusion from the grain boundary to the neck, and plastic flow by dislocation motion cause neck growth as well as densification Similar to conventional HPIM, solid-state diffusion mechanisms are responsible for sintered densification. During sintering, surface transport mechanisms provide for neck initiation and bulk transport processes for neck growth, leading to the surface energy reduction and fabrication of fully dense PIM part (i.e., up to a final average density of 98%). However, depending on the material being sintered, one or a couple of those mechanisms may be dominated during the sintering. Previous studies have shown that powder characteristics such as chemical composition, particle size, and particle shape and sintering parameters such as heating and cooling rate, temperature, and atmosphere can affect the final microstructure, sintered density, and mechanical properties (Ji, Loh, Khor, & Tor, 2001; Ma, Qin, Zhang, Zhang, Tian, Zhang, Li, et al., 2013; Song-lin et al., 2003; Y. Zhang et al., 2018). For instance, as shown in Figure 1.7a-d for Fe-50Ni parts sintered under different atmospheres, the grain size, pores, and microstructures differ. It can be seen that the sample sintered in hydrogen has fewer pores and larger grain size where the presence of interstitial impurities such as C, O, and

N restrict grain growth of the samples sintered in a vacuum or inert gas (Ma, Qin, Zhang, Zhang, Tian, Zhang, Li, et al., 2013).

As another example, Figure 1.7e-f shows the effect of sintering temperature on sintered microstructure where an increase in the sintering temperature from 1300 to 1400°C for stainless steel sintered part increases densification and pore isolation (German, 2016). Generally, sintered properties of PIM parts are superior to those of PM parts. Figure 1.7g-h show the microstructure of stainless steel parts produced by PM and PIM. Although the two microstructures have identical porosity (i.e., 8%), the pores' morphology and distribution are completely different, predominantly affecting the final mechanical properties (Yoon, Lee, Ahn, Lee, & Lee, 2003).

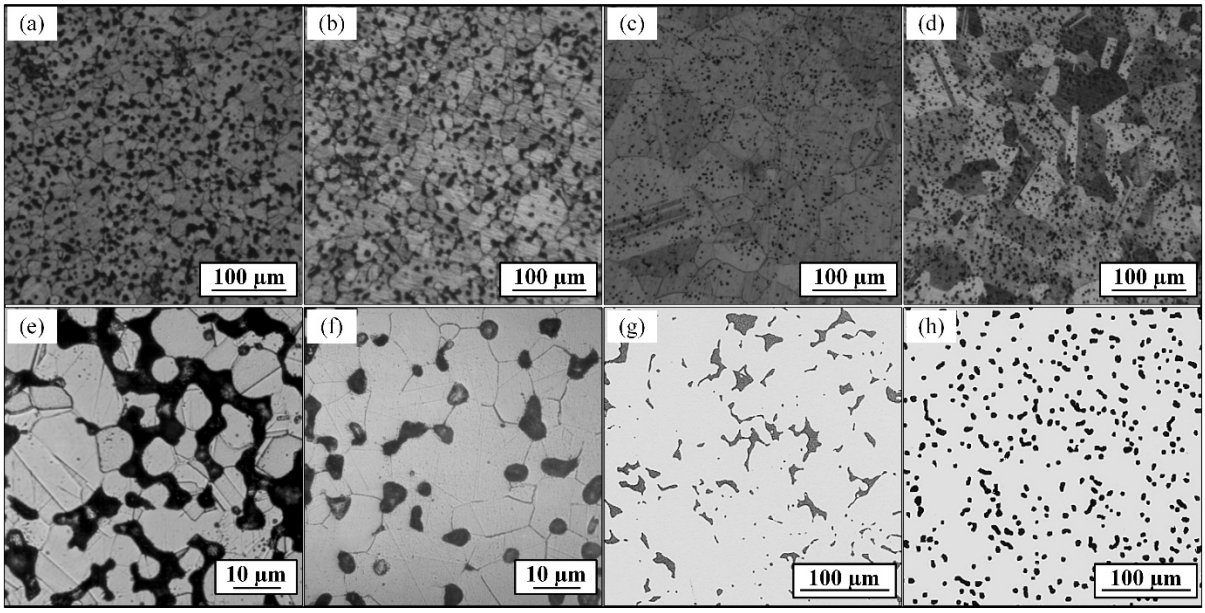

Figure 1.7 Microstructures of Fe-50Ni alloy sintered in (a) argon, (b) nitrogen,(c) hydrogen, and (d) vacuum atmosphere
Taken from Ma et al.(2013),
microstructures of 316L SS sintered at (e) 1300°C and (f) 1400°C
Taken from German (2016) and
microstructure of 316L SS produced by (g) PM and (h) PIM technologies
Taken from Yoon et al. (2002)

Nonetheless, unlike PM parts, surface oxidation is still one of the main considerations during the sintering of metallic PIM parts. After debinding, the brown part is essentially loosely packed powder structures prone to surface oxidation due to the highly porous surface. Therefore, a carefully controlled sintering atmosphere such as high vacuum, nitrogen, or hydrogen, depending on the metal's reactivity, is essential to overcome this issue (Hrubovčáková & Harvanová, 2011). Also, sintered densification of PIM parts is accompanied principally by relatively large shrinkage. For example, for a feedstock with a solid loading of about 60 vol. %, a shrinkage of around 15% is expected in the final sintered part (German & Bose, 1997). Consequently, most common defects, such as cracks or inhomogeneity in sintered density or mechanical properties, are related to poorly controlled shrinkage that needs to be considered during the earlier stages of PIM design.

1.2 PIM of iron-based powders

Iron powders are widely used in different industrial sectors, from biodegradable stent in medical implants to magnetorheological fluids in aerospace, with major powder metallurgy (PM) applications in automotive, electrical, and electronics industries and a global market size of USD 1.8 billion in 2021, projected to reach USD 2.4 billion by 2028 (Industry Research, 2022). Nevertheless, the estimated share of iron powders in the PIM industry is close to 6 000 tonnes per annum (TPA) and still minimal, about 32% of all PIM metal powder sales (Williams, 2018). Yet, the demand for PIM iron powder is forecasted to grow due to new applications in electrical, electromagnetic, and alternative energy industries (Moon, Dwarapudi, Sista, Kumar, & Sinha, 2021).

In this context, spherical carbonyl iron powders (CIP) with fine particle size (D_{50} = 4 to 7 µm) are the main source iron powder for the PIM industry. This powder is produced by thermal decomposition technique and invented by BASF company that is commercially available from 1925 (Friederang & Schlegel, 1999), Some of the major "PIM" grades (i.e., the particle size and particle size distribution are tailored for PIM application) CIPs are summarized in Table 1-4 (J. Shu & Koehler, 2017), with BASF still being the largest manufacturer.

Table 1-4 Some of the major producers of PIM-grade carbonyl iron powder

Company	Country	Grade	D_{50} (μm)	Chemical composition			
				Fe_{min} (%)	C_{max} (%)	O_{max} (%)	N_{max} (%)
BASF	Germany	CIP OM	3.9-5.2	97.8	0.75-0.90	0.15-0.40	0.65-0.90
BASF	Germany	CIP CC	3.8-5.3	99.5	0.05	0.18-0.35	0.01
Sintez-CIP	Russia	BC	<6.0	99.0	0.02-0.1	0.30	0.1
Tianyi	China	YMIM70	<4.0	Bal.	0.68-0.70	0.30	0.7
Tianyi	China	YMIM90	<5.0	Bal.	0.76-0.90	0.60	0.9
Jinchuan	China	F02	<5.5	99.0	0.1	0.3	0.1
Yuean	China	HY1	<5.5	99.5	0.03	0.3	0.1

Generally, CIP forms the basis for most PIM parts made from iron, iron-nickel, and those alloys produced by master alloy mixtures; therefore, plenty of research is available on different aspects of PIM technology using this powder. The earliest research goes back to 1989 when Hens et al. (Hens, Lin, German, & Lee, 1989) studied the effect of different binder constituents on the molding properties of PIM iron-based feedstocks. They confirmed that while a higher PP content (40 wt. %) as a backbone polymer does not significantly increase the molded part's green strength, adding SA as a surfactant agent decreases the viscosity and enhances the feedstock moldability. Japka and German (Japka & German, 1992) developed several feedstocks from three different PIM grade CIPs and an identical binder formulation consisting of PW, PP, CW, and SA with solids loading from 60 to 66 vol. %. They studied the effect of powders characteristics on maximum solid loading, sintered density, mechanical properties, and microstructure. Hsu et al. (Hsu, Lin, & Lo, 1996) studied the effect of four different waxes consisting of paraffin wax (PW), polyethylene wax (PEW), carnauba wax (CW), and acrawax (AW) as the main binder component in binder systems composed of only wax and low-density polyethylene (LDPE) on feedstock's molding performance, debinding, and sintering properties of CIP injected pars. They confirmed that in the absence of surfactants, the polar waxes such as AW or CW have better interactions with iron powder resulting in feedstocks greater shear thinning and lower flow activation energy but higher viscosity than nonpolar waxes.

More recently, with increasing development and demand for micro-components, CIP has also gained more popularity for producing micro-PIM components. For instance, Choi et al. (Choi, Park, Hong, Lee, & Lee, 2017) studied the rheological behavior iron-based feedstocks containing of micro- and nano-iron powders and demonstrated that this powder mixture could increase the solid loading up to 72 vol. %. Simultaneously, the employment of extremely fine and expensive spherical powders increases the production cost significantly since the powder potentially represents up to 50% of the total manufacturing cost. Therefore, using alternative cost-efficient iron powders such as water-atomized iron powders has been of interest for decades in PIM industry. More recently, different aspects of PIM technology in feedstock moldability, debindability, and sinterability have been investigated using CIP and other iron powders as the base powder or in mixtures with other powders.

Along with moldability, numerous attempts have been made to determine the effect of debinding and sintering parameters on final sintered part quality. For instance, Hartwig and Schroeder (Hartwig & Schroeder, 2012) studied the effect of reducing (H_2) and inert (Ar) atmospheres on carbon and oxygen evolution during thermal debinding and sintering of two feedstocks with the solid loading of 55 vol.%, consisting of two PIM grade CIP (i.e., non-reduced and reduced) and a PW-binder system containing polyethylene (PE) as a backbone polymer. Using a mass spectrometer coupled directly to the furnace, they monitored the evolution of volatile gas species generated during the thermal debinding and sintering processes. They concluded that debinding/sintering in the hydrogen atmosphere completely decarburized parts made from two grades of CIP. However, in the case of the argon atmosphere, reduced CIP interacts with the binder and picks up carbon during binder decomposition even at debinding temperatures below 600°C that, during sintering in the hydrogen atmosphere, gets rid of it in the form of methane. Li et al. (Li, Huang, & Qu, 1999) demonstrated that PIM technology could produce new alloys (e.g., Fe-2Ni) from mixing CIP and carbonyl nickel powders. Mariot et al. (Mariot, Leeflang, Schaeffer, & Zhou, 2016) used CIP to develop degradable biomaterials for stent applications. They showed that a feedstock of 66 vol. % solids loading (above the critical loading) exhibited the highest elongation and acceptable in-vitro degradation rates.

Also, some research groups have studied the production of PIM iron or iron-based parts from powder mixtures (coarse and irregular with fine and spherical) for cost reduction. For instance, Wang and Hon (J. S. Wang & Hon, 1999) studied the effect of using powder mixtures from CIP (D_{50}= 5µm) and coarse water atomized iron powders (D_{50}= 84µm) as base powder and 4 wt.% copper as a sintering aid on feedstock's solid loading and final sintered density and mechanical properties. They concluded that while low solid loading of about 42 vol. % is expected for feedstocks prepared from coarse powders and wax-based binder, the solid loading could increase to about 72 vol. % for the powder mixture due to higher packing density associated with mixing two different sizes of powders. Also, they confirmed that the PIM parts produced from a powder mixture with 30 wt. % CIP has a relative density of 84% and better mechanical performance than the parts produced with 20 wt. % of the same powder. The state of the art on iron-based feedstock used in PIM show that CIP powder is undoubtedly the most used powders. However, PIM process using irregular shape iron powders has been only studied in HPIM and never considered in LPIM process.

1.3 LPIM of irregular powders

The LPIM of high-performance ceramics such as springs, electrical insulators, and semiconductors has been around for several decades (Edirisinghe & Evans, 1986; Krindges, Andreola, Perottoni, & Zorzi, 2008). However, this fascinating processing technique for the fabrication of metal parts from metallic powder is still limited with a few work on feedstock moldability (Ghanmi & Demers, 2021; Liberati et al., 2006), the design and building the laboratory-scale LPIM injection machines (Gonçalves, 2001; Lamarre, Demers, & Chatelain, 2017), and appealing research on fabrication of LPIM metallic components. For example, Julien and Després (Julien & Després, 2006) developed an LPIM feedstock from Inconel powder and successfully manufactured aerospace turbine blades with fine microstructure, a sintered density of 96.3% theoretical density, and a carbon content of 0.01%. LPIM is an ideal fabrication technique where fabrication of smaller batch sizes (i.e., 5,000-10,000) parts associated with the aeronautic, automotive, and biomedical applications from superalloys,

titanium alloys, and precious metals is inevitable. (Rei, Milke, Gomes, Schaeffer, & Souza, 2002).

On the other hand, most of the work done on LPIM of metallic feedstocks is focused on spherical metal powders, and LPIM of irregular metal powders is very little reported in the literature. For instance, Moghadam et al. (Moghadam, Fayyaz, & Ardestani, 2021) studied the processability of an irregular hydride-dehydride titanium powder shown in Figure 1.8a in terms of feedstock moldability, or debound and sintered part quality. The feedstock texture and viscosity profiles for two different solid loadings are shown in Figure 1.8b and c. Although the viscosity of the feedstock is relatively lower than those of conventional feedstocks, the viscosity profiles were obtained at 165 °C, which is relatively high for LPIM feedstocks. Also, even though the viscosity profiles could be obtained for the higher solid loadings (i.e., 60 and 65 vol. %), only the feedstock with the solid loading of 53 vol. % could be used to fabricate defect-free green parts. Also, due to the high percentage of LDPE in the binder system (27 wt. %), the debinding was done in two solvent/thermal steps similar to those have been used for conventional PIM that promote the impurities such as C, N, and O contents of the sintered parts. Nonetheless, this work proves that the LPIM of irregular metal powders is generally possible but needs more investigation.

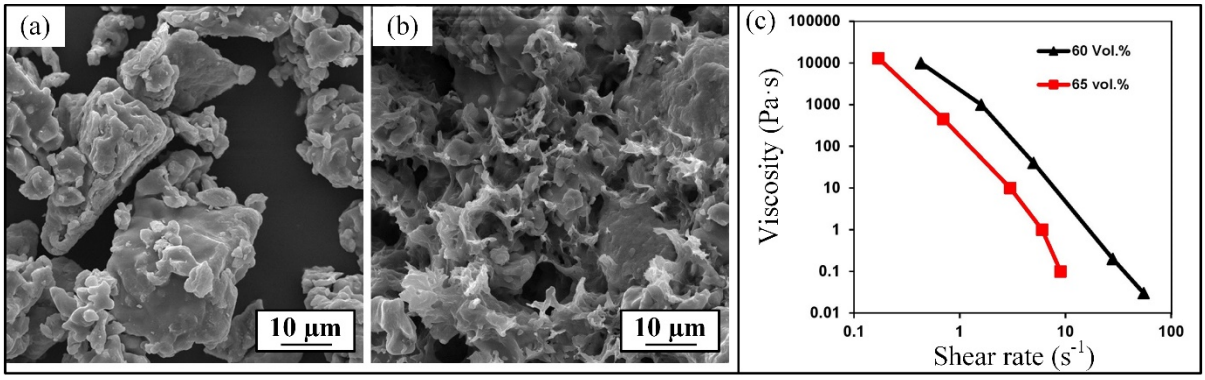

Figure 1.8 (a) Titanium powder morphology, (b) feedstock texture, and (c) feedstock viscosity profiles
Taken from Moghadam et al. (2021)

In the framework of the current project and as another example for LPIM of irregular powders, Majdi et al. (Majdi, Tafti, Demers, Vachon, & Brailovski, 2022) studied the effect of particle shape and size of three irregular water-atomized iron powders and spherical CIP on maximum solid loading and sintered density. Using a pycnometer density approach, they confirmed maximum solids loading of the irregular iron powders varying between 56 to 58 vol. % and 62 vol. % for CIP. Furthermore, the LPIM binder system consisting of PW, CW, SA, and EVA used in this study produced low-viscosity feedstocks where the viscosity of all feedstocks at 80 ºC was below 10 Pa·s at a reference shear rate of 100 s^{-1} as shown in Figure 1.9a. Furthermore, using thermogravimetric analysis (TGA) shown in Figure 1.9b, they confirmed that a single thermal wick debinding process at 450ºC could fully extract and decompose binder, whereas in the absence of backbone polymer ramp up to the pre-sintering temperature of 650 ºC required to provide the brown part with enough strength (Figure 1.9c). Also, the samples sintered at 1250ºC under a hydrogen atmosphere produced a relative sintered density of 83% for the fine irregular iron powder. Although the results were promising for the fabrication of metal parts from irregular iron-based powders via the LPIM approach, the effect of binder constituents of feedstock quality and overall moldability of the feedstock, as well as final part mechanical properties, have not been reported in the research mentioned above work.

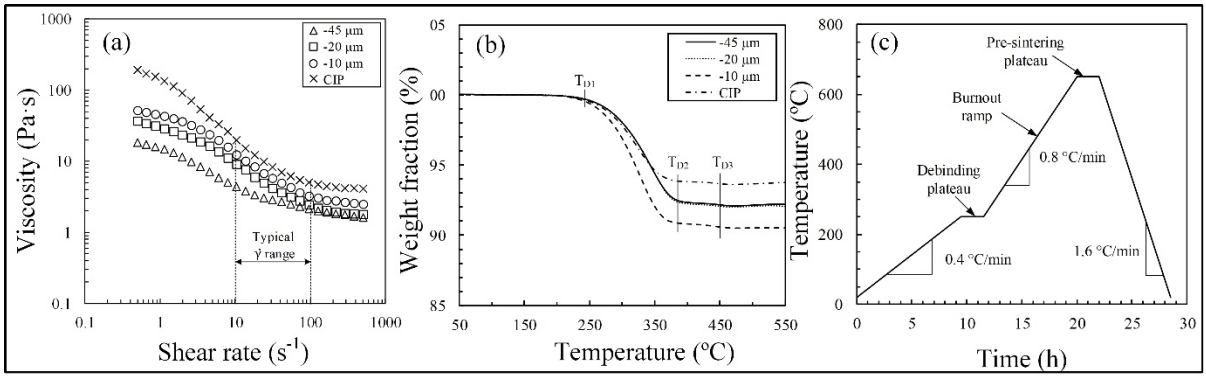

Figure 1.9 (a) Feedstocks viscosity profiles, (b) TGA micrograph of feedstocks, and (c) debinding cycle
Taken from Majdi et al. (2022)

CHAPTER 2

RESEARCH PROBLEM AND OBJECTIVES

2.1 Problem statement

Notwithstanding the above in the literature section, irregular iron powders, a significant cost-effective material in PIM industry, have received limited attention from researchers. Specifically, the knowledge of LPIM application to irregular powders to produce intricate metallic parts is scarce. LPIM has been a cost-effective manufacturing technique for producing near net-shape ceramic components for more than four decades. Nonetheless, LPIM of metals is still in its infancy and remains a manufacturing method with a low technological readiness. Although this fascination technique has gained more attention during the last few years through the development and characterization of metallic feedstocks such as titanium (Ghanmi & Demers, 2021) or tool steel (Liberati et al., 2006), the current understanding of the fabrication of metallic components is still limited. Therefore, there is a gap in the knowledge of LPIM processing for this metallic powder in the literature that requires more detailed investigation. In addition, the documented literature is missing the molding properties, debindability, and sinterability of LPIM feedstocks formulated from irregular metallic powders.

2.2 Objectives

The main objective of this research is to investigate the processability of water-atomized iron feedstock via LPIM and quantify the performances of the manufactured metallic parts. To that end, the following sub-objectives will be reached:

- Develop a new feedstock formulation adapted to LPIM of irregular metallic powders.
- Assess the molding performance of low-viscosity iron-based feedstocks.
- Design a thermal wick-debinding cycle based on binder burnout and a pre-sintering approach.

- Study the influence of powder characteristics and sintering parameters on the final density, microstructure, and mechanical properties.

CHAPTER 3

METHODOLOGY

Each article describes and details the methodology used for each project stage (Chapters 3-5). In addition, a brief overview of the material selection, the description of research facilities, and the equipment used, the characterization methods, and the process parameters are provided in this chapter.

3.1 Materials

3.1.1 Iron powder production and selection

During the first phase of the powder selection, RTMP iron powders were produced starting with water-atomized unannealed powders that were further attrition milled and sieved. Some lots were annealed while other remain in their unannealed state. However, during the preliminary feedstock preparation, annealed powders could not be successfully loaded into the binder system even at a solid loading as low as 50 vol. % due to their poor flowability, this powder was thus simply eliminated and was not used in this study. During the second phase of the project, unannealed iron-based powders were selected and successfully be loaded to higher solid loading (close to 60 vol. %). The specifications of the selected powders are summarized in Table 3-1.

Table 3-1 Iron powder's physical and chemical properties

Description	-45 µm	-25 µm	-10 µm
Condition	Unannealed	Unannealed	Unannealed
Carbon (%)	2.934	2.806	2.649
Sulfur (%)	0.005	0.005	0.006
Oxygen (%)	4.100	4.710	6.030
Nitrogen (%)	0.008	0.008	0.010
Pycnometer density (g/cm^3)*	7.4	7.1	6.9
D_{10} (µm)	2.6	2.4	1.7
D_{50} (µm)	13.8	10.9	7.0
D_{90} (µm)	35.9	24.6	16.4

3.1.2 Binder constituent

This study used five different polymers as binder constituents based on their extensive use in the PIM and LPIM processes. PW was used as the main carrier to ensure proper feedstock fluidity, SA was used as a surfactant agent to improve feedstock homogeneity and binder-powder interaction, and EVA was used as a thickening agent to decrease the risk of segregation and increase the feedstock stability and homogeneity during the mixing and injection and increase the green strength of the injected part. In addition, the CW and BW were also used to study the specific effect of these constituents on the rheological properties of the feedstock since these polymers are naturally available, environmentally friendly, and inexpensive. The specifications of the binder constituents are summarized in Table 3-2.

Table 3-2 Characteristics of binder constituents

Constituent	Melting point (ºC)	Density (g/cm^3)	Supplier
Paraffin wax (PW)	54.0	0.90	Sigma- Aldrich
Beeswax (BW)	65.0	0.96	Sigma- Aldrich
Carnauba wax (CW)	84.5	1.00	Sigma- Aldrich
Stearic acid (SA)	67.0	0.90	Sigma- Aldrich
Ethylene-vinyl acetate (EVA)	49.0	1.00	DuPont Elvax

3.2 Characterization methods

This section details the different techniques used to characterize the raw materials, feedstock, debound parts, and sintered parts produced via the LPIM approach.

3.2.1 Powder and binder characterization

The particle shape and particle size distribution (PSD), along with the binder formulation, are the most relevant characteristics driving the feedstock properties at the mixing and injection phases and the quality of debound and sintered parts. Based on a dry powder system and Fraunhofer optical diffraction model, PSD was quantified using a laser diffraction particle size analyzer (Beckman Coulter LS 13-320) as shown in Figure 3.1a . Fraunhofer's theory assumes

that the laser beam is parallel while the detector is at a very large distance compared to the diffracting particle's size (Eshel, Levy, Mingelgrin, & Singer, 2004). Therefore, this instrument is suitable for precisely measuring the particle size distribution as low as 400 nm. As illustrated in Figure 3.1b-c, small particles diffract light at a higher angle, and large particles diffract light at a lower angle, which then the energy diffracts off the particles and detecting scattering patterns determine the PSD through high-, medium-, and low-angle light-sensitive detectors. The main advantages of this technique include short analysis time (10 min per sample), high repeatability, and the needed small sample size (~1 g).

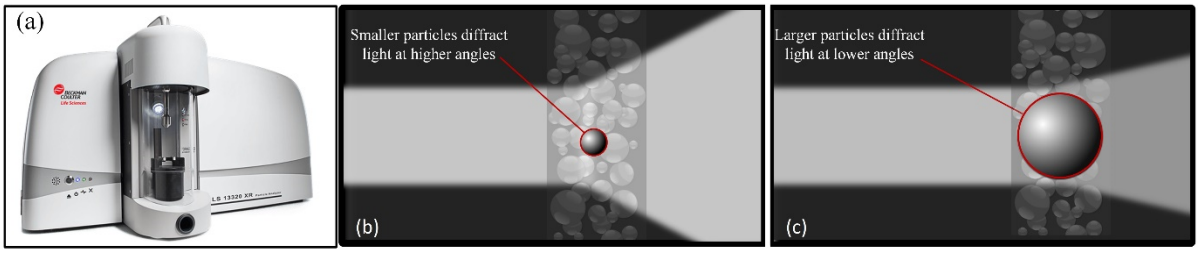

Figure 3.1 (a) Representation of diffraction patterns in laser diffraction particle analyzer at (b) high and (c) low angles for small and large particles, respectively

A scanning electron microscope (SEM, Hitachi 3600N, shown in Figure 3.2a) was used to evaluate the particles' morphology. The fundamental components of a typical SEM are shown in Figure 3.2b. The basic principles of the SEM involve the creation of a finely focused beam of electrons through emission from an electron source. The energy of the electrons beam, E_0, is typically between 0.1 to 30 keV. After emission from the source and acceleration to high energy, the electron beam is modified and focused by one or two condenser lenses (i.e., electromagnetic lenses), which reduce the beam diameter and scan the focused beam in a raster (x-y) pattern to place it sequentially at a series of closely spaced discrete locations on the specimen. The interaction between the primary electrons and specimen surface produces two outgoing electron products as follows; first, the ejected electrons from atoms in the sample that escape from the specimen's surface are called secondary electrons (SEs) that produce a mostly topographic image of the sample, and second, the electrons that reflect off of the surface and deeper from within the sample after experiencing scattering and deflection by the electric fields

of the atoms in the sample called backscattered electrons (BSEs). In this project, the secondary electron detector was used to observe the dry powder, the debound network and the metallographic analysis after sintering.

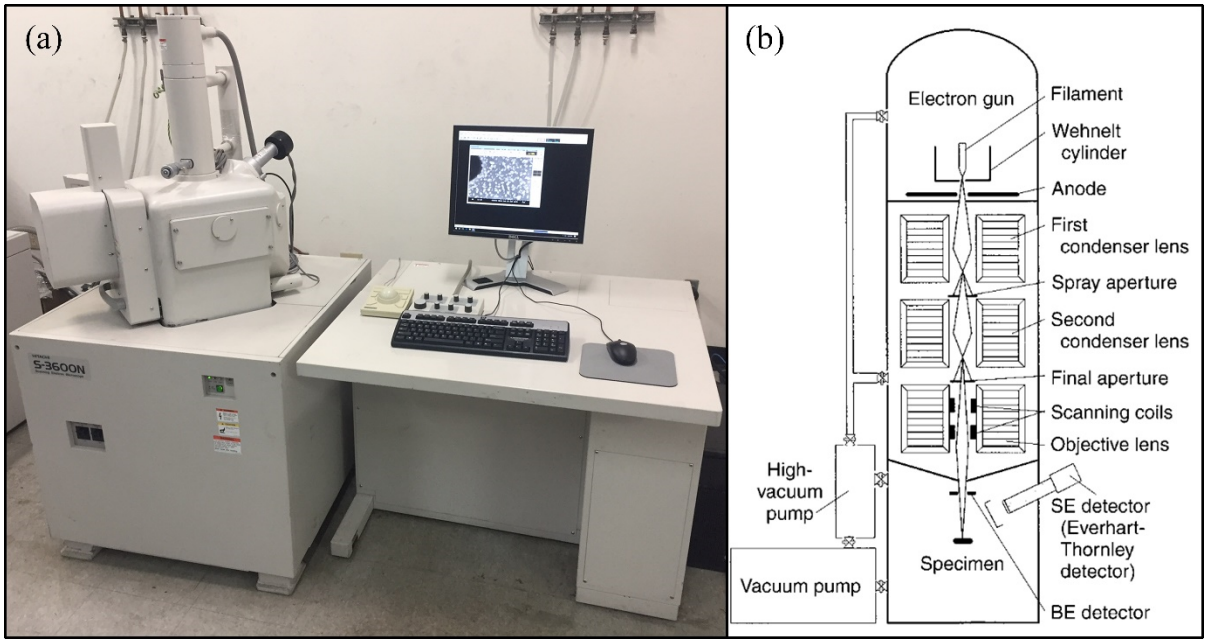

Figure 3.2 (a) SEM Hitachi 3600N used in this project and (b) simplified schematic representation of a typical scanning electron microscope
Taken from Exner & Weinbruch (2004)

The true density values (also called skeletal density and absolute density) of powders, binders, and feedstocks were obtained according to ASTM standard (ASTM B923-16, 2016) using an AccuPyc II 1340 (Micromeritics, Norcross, GA, USA) pycnometer shown in Figure 3.3a. From the mass previously measured using a precision balance, the pycnometer measured the volume occupied by a specimen using the helium gas displacement volume illustrated in Figure 3.3b. The instrument has two chambers inside the system, one for the sample (sample chamber) and the other for the gas pressurization (expansion chamber). Once the sample is placed in the sample chamber, several purging (5 to 10 cycles) is performed, ensuring both the sample and the instrument are cleaned of any other gases that otherwise interfere with the accuracy of the measurement before proceeding with the analysis. The first stage of the analysis is to fill the sample chamber with helium gas undertaken to the pre-specified pressure of around 20 psig.

The pressure is then allowed time to equilibrate and is recorded as the first pressure (P_1) with the transducer. The expansion valve is then opened, and the gas flows from the sample chamber through the expansion chamber. After the pressure is allowed to equilibrate again, it is recorded as the second pressure (P_2). Finally, using equation (3.1), values of P_1 and P_2 are then applied to the rearrangement of Boyle's law ($P \propto \frac{1}{V}$) as follows:

$$V_S = V_C - \frac{V_E}{\frac{P_1}{P_2} - 1} \tag{3.1}$$

where V_S is the sample volume, V_C is the volume of the calibrated sample cell, and V_E is the volume of the calibrated expansion cell. Then, using the measured mass (m), the true density (ρ_A) is ultimately calculated as follows:

$$\rho_A = \frac{m}{V_S} \tag{3.2}$$

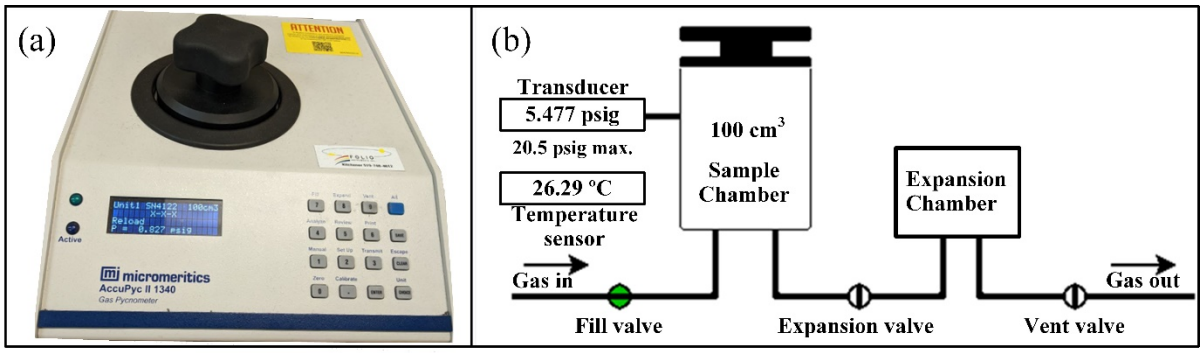

Figure 3.3 (a) AccuPyc II 1340 used in this project and (b) schematic representation of the helium gas pycnometer system

3.2.2 Thermal characterization of feedstock

In this work, a thermoanalytical characterization of the feedstock was performed using two techniques in which the feedstock's melting point (T_m) and degradation temperatures (T_D) were determined. On the one hand, T_m is linked to the change from solid to liquid state that defines the mixing and molding temperature limits. On the other hand, T_D quantifies the burnout start

and finish temperatures that can be used to tailor the debinding cycle. T_m and T_D were quantified using differential scanning calorimetry (DSC) and thermogravimetric analysis (TGA).

Differential scanning calorimetry (DSC) analysis

DSC is a thermoanalytical method that provides qualitative and quantitative information about endothermic and exothermic reactions as well as heat capacity or physical/chemical changes within a material according to temperature. Figure 3.4a shows the Perkin Elmer Pyris 1 DSC device (Perkin Elmer, Waltham, MA, USA) used in this project to quantify each binder constituent and feedstock melting point. According to ASTM D3418-21 standard (ASTM International, Materials, & ASTM International, 2012), the binder or feedstock sample with a mass of around 10 mg was encapsulated in a standard aluminum hermetic pan before being placed into the instrument cell, as illustrated in Figure 3.4b. Two sequential temperature scans were performed from 20 to 100 ºC with a heating rate of 10 ºC/min under a dry nitrogen gas flow of 50 ml/min. Based on the power consumption principle, the amount of energy absorbed or released by the sample is finally reported in a DSC thermogram, as shown in Figure 3.4c, recorded from the second heating cycle. The first heating scan (not shown in the figure) that is affected by the production and the sample's mechanical and thermal history is used to erase the thermal history, allow the molecules to reach a near-optimal molecular orientation, and maximize the thermal contact between the pan and the specimen. The peaks' orientation in the endothermic direction in Figure 3.4c indicates the different melting points first (T_m = 32.8 and 57.7°C, for instance) for this specific feedstock. In this specific example, the mixing and injection molding must be performed at temperatures higher than 57.7°C to ensure that these operations are done in the liquid state. At the same time, the part must be demolded at a temperature below 32.8°C to prevent sticking and maximize the shape retention of the molded part.

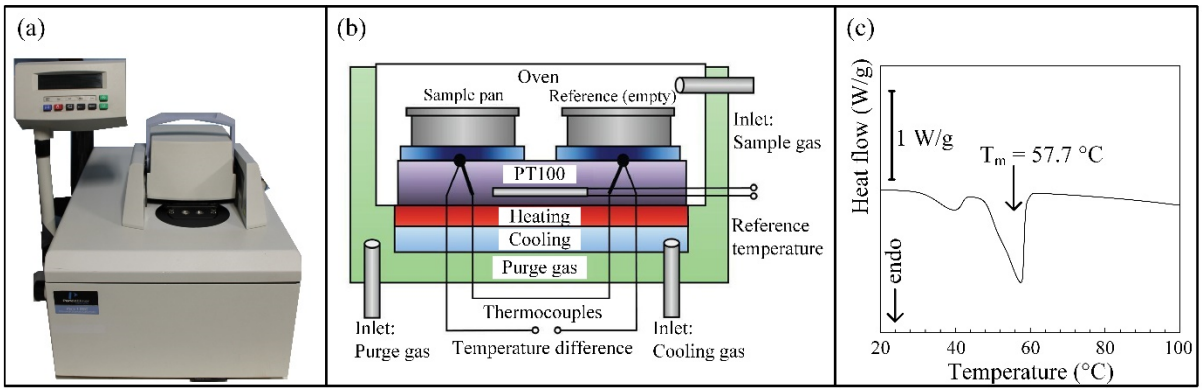

Figure 3.4 (a) Perkin Elmer Pyris 1 DSC used in this project,
(b) schematic representation of DSC cell
Taken from Bhowmick, Sengodan, & Thangavel (2014),
and (c) a typical DSC curve of a feedstock
Taken from Majdi et al. (2022)

Thermogravimetric analysis (TGA)

TGA is a thermoanalytical technique that provides qualitative or quantitative information about the decomposition, oxidation, or thermal stability of a material by monitoring mass change (loss or gained) as a function of temperature (dynamic mode) or time (isothermal mode) in the desired inert or reactive atmosphere (Leng, 2008). Figure 3.5a shows an STA 8000 (Perkin Elmer, Waltham, MA, USA) used in this work to quantify T_D start and finish. In this test, a 10 mg specimen was placed in a standard platinum pan and heated up from 100 to 600°C using a heating rate of 10 °C/min under argon gas at a flow rate of 60 ml/min. The schematic diagram of this TGA apparatus is also shown in Figure 3.5b, where as the sample's temperature gradually rises in the furnace, the changes in weight are measured on an analytical balance outside the furnace. The TGA thermogram is a graphical representation of the mass change, and it is normally plotted with the weight fraction on the vertical axis and temperature (T) or time (t) on the horizontal axis.

In PIM, TGA on binder constituents and feedstock is used to predict binder decomposition behavior and design the debinding cycle (Hwang & Tsou, 1992). For the example presented in Figure 3.5c, the mass loss that represents the decomposition of individual binders SA, PW, and

EVA starts at 150, 160, and 280°C, and ends at 380, 470, and 480°C, respectively. In addition, on the same graph, the change in weight fraction for feedstock corresponds to the initial (T_{D1}) and final (T_{D2}) temperatures of binder burnout at 250 and 380°C, respectively. As a result, T_{D1} represents the lowest temperature at which the onset of a mass change was detected, and T_{D2} represents the lowest temperature by which the binder decomposition and final burnout have been completed (Majdi et al., 2022). The TGA profile obtained for the feedstock shows a remaining weight fraction of around 90 wt. %, corresponding to the powder's relative weight initially contained in the mixture.

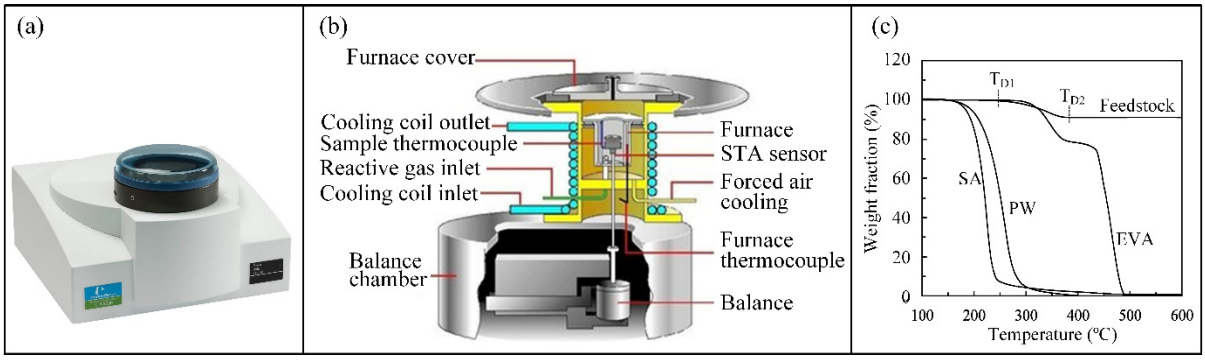

Figure 3.5 (a) Simultaneous thermal analyzer (STA 8000) used in this project,
(b) cross-section representation of a TGA instrument
Taken from the technical structure of STA8000 (2022),
and (c) a typical TGA thermogram of binder constituents and feedstock
Taken from Majdi et al. (2022)

3.2.3 Rheological properties of the feedstock

In PIM, the study of melt flow behavior is essential to predict a given feedstock's molding capability (i.e., moldability). In other words, the rheological characterization of feedstocks provides a means of evaluating homogeneity, stability, and lot-to-lot variability crucial during the feedstock formulation, mixing, and injection molding stages. Although generally, the viscosity profiles of all feedstocks cannot be measured using a single piece of equipment at different shear rates, as illustrated in Figure 3.6, the viscosity responses can be quantified at different shear strain rates using rotational or capillary rheometers where for the shear rate

range between 10^{-1} and $1s^{-1}$ the rotational rheometer under steady-state shearing conditions is more accurate. A rotational rheometer under oscillating shear conditions can be used for less viscose feedstocks, whereas a high-pressure capillary rheometer is utilized for higher viscosity feedstocks.

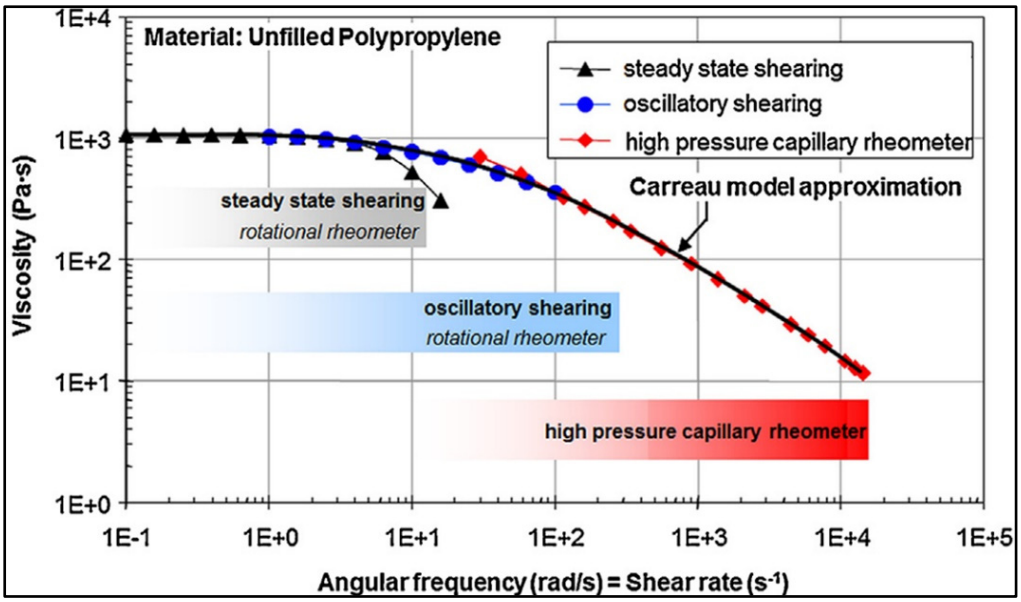

Figure 3.6 Application of different rheometers for different shear rate ranges
Taken from Kukla, Duretek, Gonzalez-Gutierrez, & Holzer (2017)

Contrary to the feedstock used in conventional PIM, in LPIM, a rotational rheometer can obtain the whole viscosity profile. Figure 3.7a shows the rotational rheometer MCR 302 (Anton Paar, Graz, Austria) used in this study. This rheometer is equipped with a concentric-cylinder geometry (CC-17), schematized in Figure 3.7b, and a Peltier temperature-controlled measuring system (C-PTD 200). Based on the Searle principle, the sample is positioned in the measuring gap between the fixed measuring cup and the motor-driven rotating bob (Song & Peng, 2008), and due to the cup's large outer surface, the sample temperature can be easily controlled from the outside. Generally, the concentric-cylinder (CC) geometries are the most suitable low-viscosity feedstocks used in LPIM. Indeed, this viscosity range is adapted to the low torque possible with a rotational rheometer but not the high force experienced with a capillary rheometer. The rotational speed produces the motor torque that overcomes the sample's

viscous forces and measures its dynamic viscosity. According to Newton's viscosity law, the dynamic viscosity (η) can be expressed as follows:

$$\eta = \frac{\tau}{\dot{\gamma}} \tag{3.3}$$

where τ is the shear rate, and γ̇ is the shear strain rate. Therefore, the instrument automatically converts the measured torque into shear stress using calibrated factors linked with the bob-cup geometry and the mandrel rotational speed into the shear rate, the latter usually imposed during the test. In our study, shear rates ranging from 0.5 to 1000 s^{-1} were pre-set, and the feedstock viscosity was measured at temperatures typically between 80 to 100ºC. Figure 3.7c presents typical viscosity profiles obtained on LPIM feedstock, where solid loading and temperature influence is clearly seen. Shear thinning flow behavior is typical for PIM feedstocks where at higher shear rates, viscosity decreases.

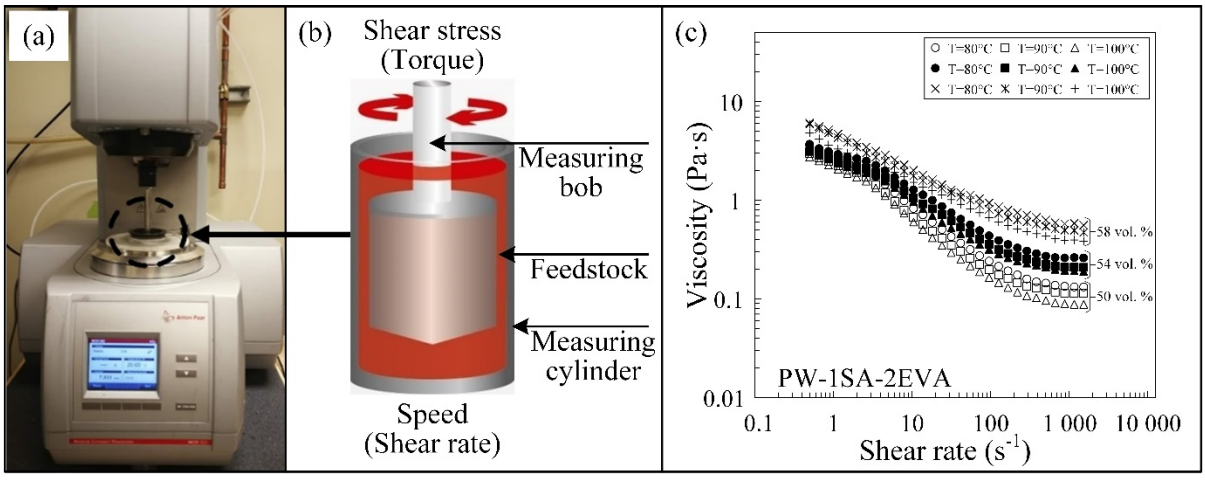

Figure 3.7 (a) Rotational rheometer, (b) cross-sectional view of the measurement area, and (c) typical viscosity curve as a function of shear rate

3.2.4 Feedstock formulation, mixing, and injection

During feedstock formulation, the precise amount of each constituent mass was measured using the analytical balance Sartorius SECURA324-1S (readability 0.1 mg) presented in Figure 3.12b, while density values were obtained at room temperature using a helium gas pycnometer as described above. Also, the volume fraction of powder was calculated using the following equation:

$$vol.\% = \left[1 + \left(\frac{\rho_{powder}}{\rho_{binder}}\right)\left(\frac{1}{wt.\%} - 1\right)\right]^{-1} \quad (3.4)$$

where vol. % is the volume fraction powder, wt. % is the weight fraction of powder, and ρ is the density of the powder or the binder reported in Table 3-2. The constituents were then mixed in a mechanical mixer and transferred into the injection press to be blended under vacuum. The low-pressure injection molding press used in this project is presented in Figure 3.8a. The schematic of the main components of injection is shown in Figure 3.8b.

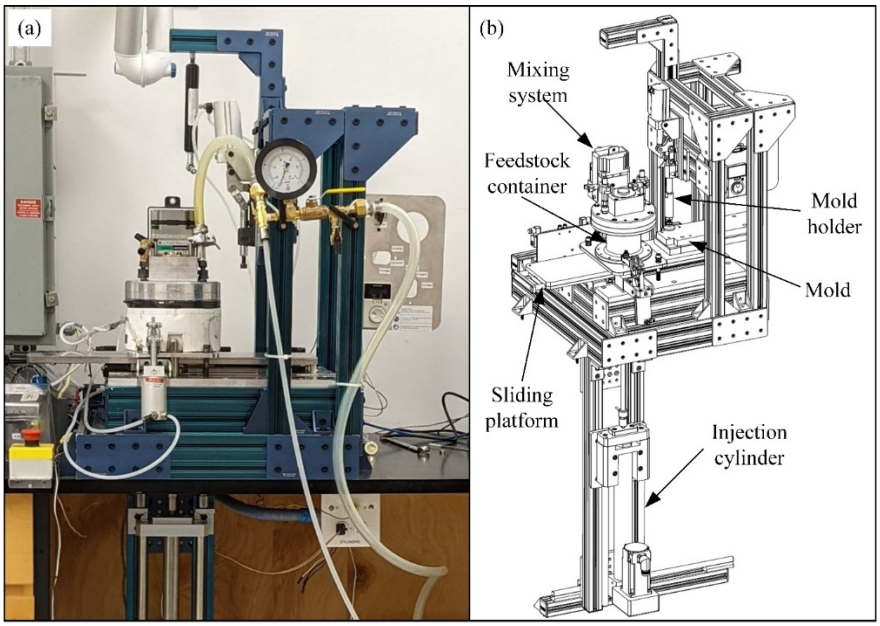

Figure 3.8 (a) Low-pressure injection molding machine made at ETS, and (b) schematic of the injection components

The injection molding press was used to inject the three green shapes illustrated in Figure 3.9. The spiral mold (Figure 3.9a) was used to quantify the feedstocks' moldability based on the injected length. To that end, the injection distance (L) was calculated using equation (3.5) of the Archimedean spiral, where a is the starting point of the spiral, b is the increment of the spiral divided by 2π, c is the number of turns of the spiral and θ is the angle in radians (in this study the mold used implies a = 4.7 mm and b = 1.516 mm).

$$L = \int_0^{c.2\pi} \sqrt{(a + b \cdot \theta)^2 + b^2}\, d\theta \tag{3.5}$$

Real-scale injections into the complex shape mold shown in Figure 3.9b were carried out to demonstrate the potential of LPIM technology to produce complex shape green parts from ready-made feedstocks. Finally, the rectangular mold shown in Figure 3.9c was used to inject rectangular samples for the debinding and sintering processes described below.

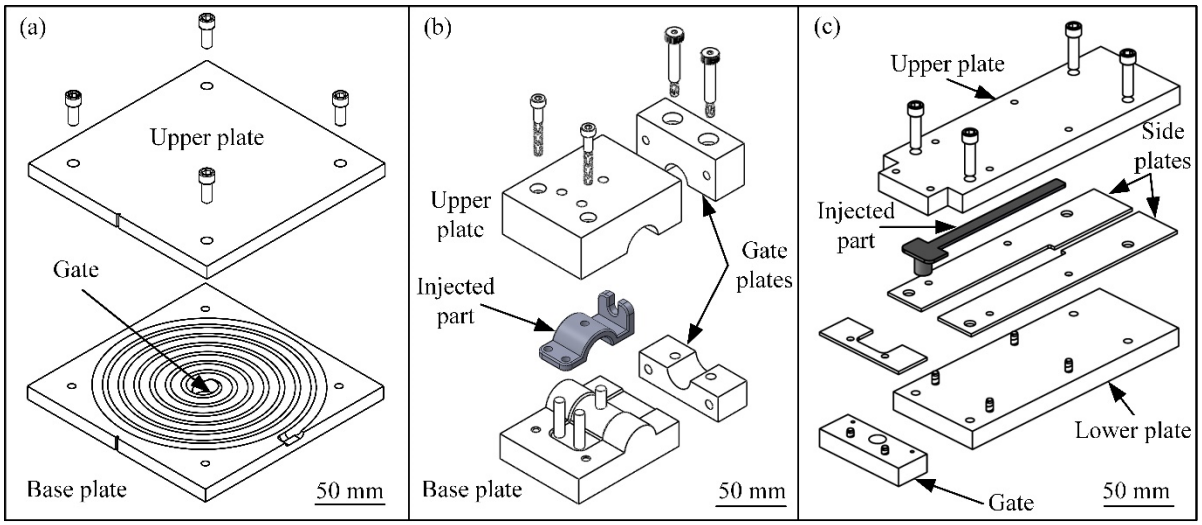

Figure 3.9 Schematic representation of the molds used in this project: (a) spiral, (b) complex geometry, and (c) rectangular molds

In the thermal wick-debinding process, the rectangular green parts were buried under loose alumina powder supported by a metallic container (also named boat), as shown in Figure 3.10a. The alumina powder was sieved using a standard mesh #18 and a vibration machine to minimize powder agglomeration. The alumina was used as a wicking agent and as a support

media for the metallic part before reaching the pre-sintering temperature. The boats were then placed in a metallic retort where the air was pumped out and flushed with argon gas (repeated five times) before setting a constant argon flow rate of 15 l/min applied during the debinding process. The retort was finally introduced in a Nabertherm N 41/H furnace shown in Figure 3.10b and heated up to 250°C for the capillary extraction of the binder during the thermal wick debinding and up to 650°C during the final burnout of the binder and also pre-sintering of the weak debound structures for a total cycle of about 23 hours (details presented in Figure 3.10c). Following debinding treatment, the parts were taken off the alumina, air cleaned, and then settled on a dense alumina setter before being sintered at high temperatures over different times. To that end, the CM furnace model 1516 presented in Figure 3.10d (available at RTMP) was programmed using the cycles shown in Figure 3.10e to sinter parts under a pure hydrogen atmosphere.

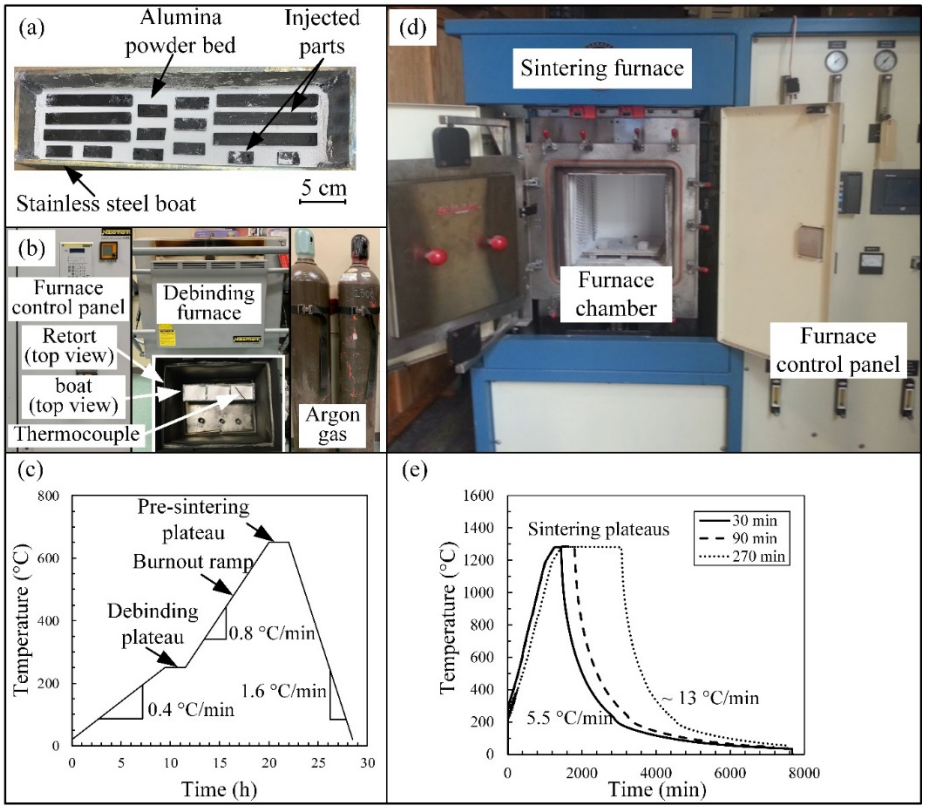

Figure 3.10 Overview of (a) thermal wick-debinding cell, (b) debinding furnace and placement of the debinding cell, (c) typical debinding and presintering cycles, (d) sintering furnaces, and (e) typical sintering cycles with different sintering times

3.2.5 Debound and sintered specimen characterization

The chemical composition is one of the most important attributes controlling the microstructure and, ultimately, the final mechanical properties of the PIM parts. Therefore, chemical analyses of debound and sintered parts were performed by a Leco analysis using the CS-200 (LECO, St. Joseph, MI, USA) and TC-500 (LECO, St. Joseph, MI, USA) analyzers shown in Figure 3.11a-b. These two analyzers, available at RTMP, were used for quantifying the evolution of carbon and oxygen. As schematized in Figure 3.11c-d, 1 to 5 g of metallic sample, usually mixed with an accelerator to hasten the combustion process, was inserted into a ceramic or graphite crucible and was heated above 1500ºC in high-performance furnaces (induction or impulse). The generated gases (i.e., CO_2, SO_2, H2O, and N_2) were then analyzed by non-dispersive infrared or thermal conductivity detectors, where the quantity of each element was accurately quantified. Also, the debound bonding networks along the cross-section were observed using the same SEM described above.

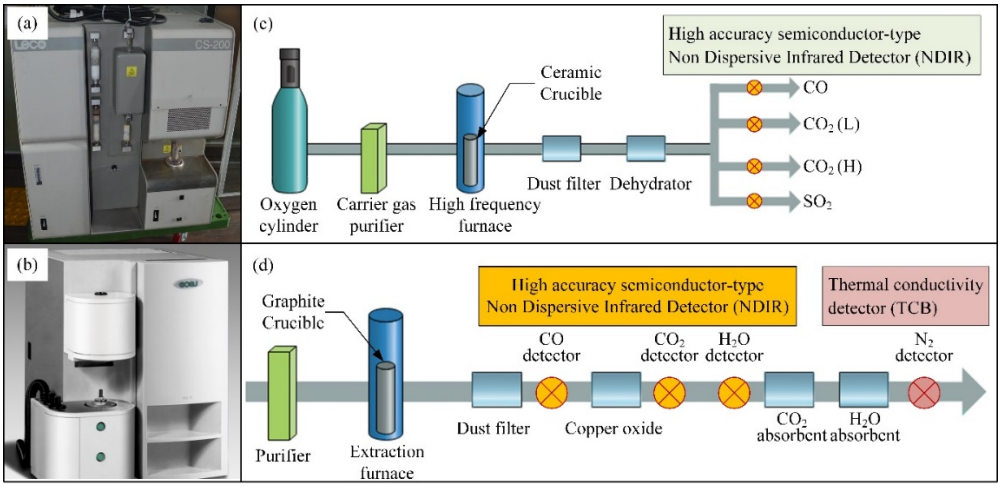

Figure 3.11 LECO elemental analysis instruments (a) carbon/sulfur analyzer (CS-200), (b) oxygen/nitrogen (TC-500) and synopsis of key components of (c) carbon/sulfur analyzer and (d) oxygen/nitrogen analyzer
Reproduced from HORIBA Scientific (2019)

The sintered density was measured using the oil-impregnation method based on Archimedes' principle according to MPIF standard 42 (Standard & Methods, 2016). First, the dry mass (*g*)

of the sintered specimen was measured, then the specimen was immersed in a beaker filled with impregnating oil (Shell Tellus S3 M32) and placed in a vacuum oven (shown in Figure 3.12a), where the pressure was reduced to 20 kPa during 2 hours at room temperature. Finally, the oil-impregnated and in-water masses were measured using Archimedes' setup (shown in Figure 3.12b) and the sintered density was calculated using equation 3.6.

$$\text{Sintered density, } (\rho s) = \frac{A\rho_W}{B - C} \tag{3.6}$$

where A is the dry mass (before oil impregnation), B is the oil-impregnated mass, C is the mass of impregnated sample in water, and ρw is the water density.

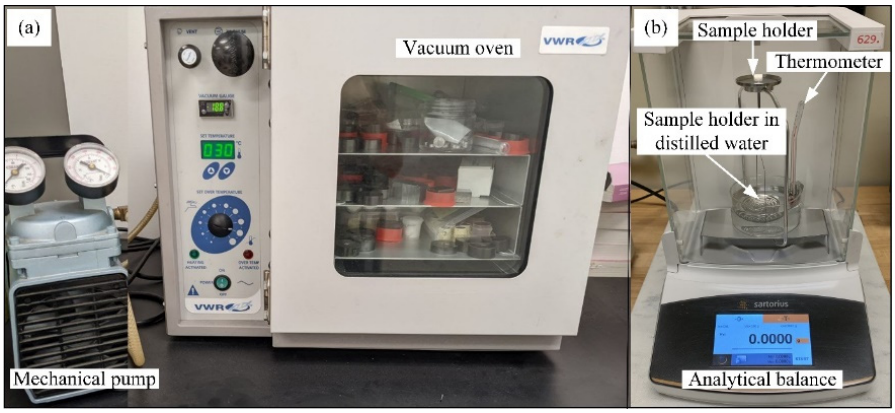

Figure 3.12 Sintered density measurement (a) vacuum oven and (b) Archimedes setup

Metallographic analyses were performed on cross-sections of the sintered specimens mounted in the conductive resin Technotherm 3000 using a hot mounting machine (Figure 3.13a), mechanically grounded using SiC papers with grits ranging from P120-P2400, cleaned using ethanol in an ultrasonic bath, mirror polished with diamond particles of 6, 3, and 1 μm, and then observed using optical and LEXT OLS4100 laser confocal microscopes (Figure 3.13b). For the microstructure observation, the specimens were chemically etched in 2 vol. % Nital solution (2 ml of concentrated nitric acid in 98 ml of ethyl alcohol) and observed using the same LEXT OLS4100 laser confocal microscope. In addition, a quantitative assessment of

average pore size and circularity in sintered specimens was performed using Dragonfly software (Object Research Systems, QC, Canada).

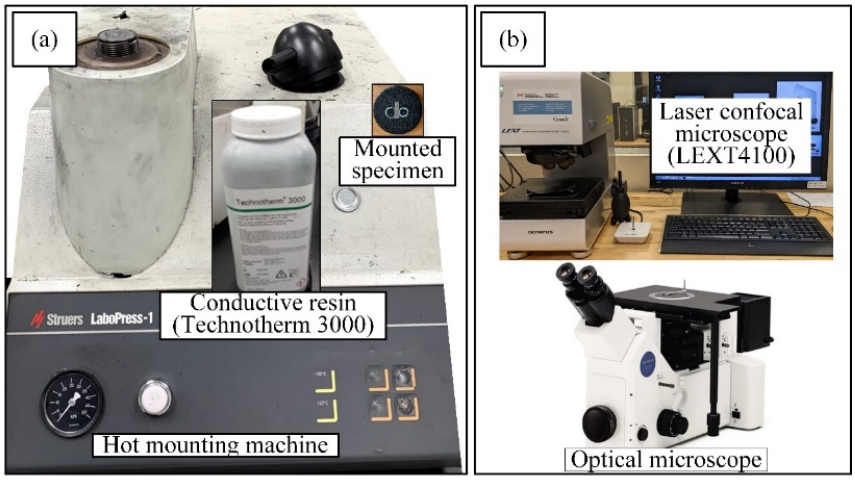

Figure 3.13 (a) Hot mounting machine and conductive resin, and (b) laser confocal and optical microscopes at ÉTS

From the rectangular sintered bars, dogbone shape tensile specimens shown in Figure 3.14a were machined as per MPIF Standard 10 (“Standard Test Methods for Metal Powders and Powder Metallurgy Products,” 2016) as illustrated in Figure 3.14b. Tensile testing was carried out using a material testing system Alliance RF/200 (MTS, Eden Prairie, MN, USA) equipped with an MTS 634.12e-54 extensometer, as shown in Figure 3.14d. An MTS 10 kN load cell (p/n 4501030) and a crosshead speed of 0.15 mm/min were used during tensile tests. Three to five replicates were done for each fabrication condition (i.e., a total of 27 specimens were tested).

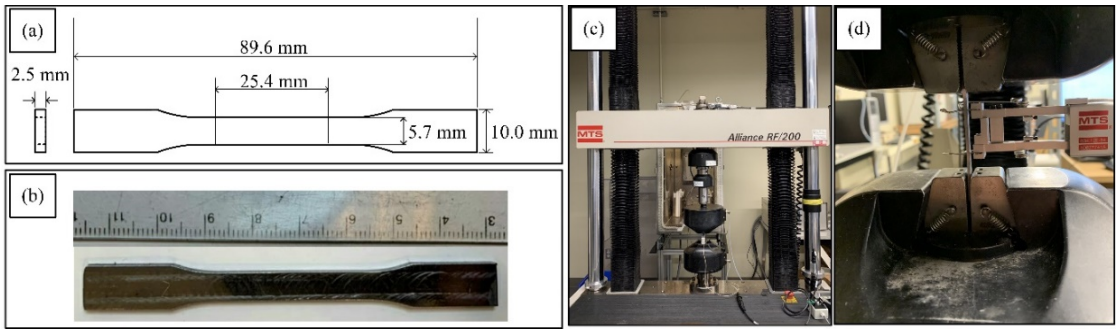

Figure 3.14 (a) Sketch of the tensile specimen, (b) machined tensile specimen from the rectangular sintered sample, (c) general view of the tensile test machine, and (d) zoom in on the specimen gauge section showing the jaws and extensometer

CHAPTER 4

EFFECT OF BINDER CONSTITUENTS AND SOLIDS LOADING ON THE RHEOLOGICAL BEHAVIOR OF IRREGULAR IRON-BASED FEEDSTOCKS

A. A. Tafti [a], V. Demers [b], G. Vachon [c], V. Brailovski [b]

[a, b] Department of Mechanical Engineering, École de Technologie Supérieure, 1100 Notre-Dame West, Montréal, Quebec, Canada, H3C 1K3
[c] Research and Development, Rio Tinto Metal Powders, 1625 route Marie-Victorin, Sorel-Tracy, Quebec, Canada, QC J3R 4R4

Paper published in *Journal of Manufacturing Science and Engineering,* October 2020

4.1 Abstract

This work presents an experimental approach employed to evaluate the influence of binder constituents and solids loading on the rheological behavior and molding properties of irregular shape iron-based feedstocks used in low-pressure powder injection molding. Thirty-six (36) different feedstocks formulated from one new in-development iron-based powder and different wax-based binder systems (paraffin wax with surfactant and thickening agents) were obtained for solids loading varying from 50 to 68 vol. %. The viscosity profiles were experimentally measured at different temperatures using a rotational rheometer to quantify each ingredient's threshold proportions in the binder systems, identify the best feedstock candidates, and calculate their moldability indices, which were finally validated using real-scale injections. Results confirmed that the best feedstock formulation was the one containing paraffin wax with 1 vol. % stearic acid used as a surfactant, 2 vol. % ethylene-vinyl acetate used as a thickening agent, and 2 vol. % carnauba wax used as a shrinking agent. An irregular shape iron-based feedstock with a maximum solids loading of 58 vol. % was successfully injected.

Keywords: powder injection molding (PIM), viscosity, feedstock, moldability, irregular powder, iron powder, binder

4.2 Introduction

Powder injection molding (PIM) has been used extensively to produce small-to-medium size complex-shaped metal or ceramic parts with good surface finishes and acceptable tolerances in a cost-effective way (Aslam, Ahmad, Yusoff, et al., 2016; German & Bose, 1997; M. M. Rueda et al., 2017). In PIM, the powder is mixed with a multi-component polymer blend known as the binder to form a feedstock that is injected into a mold cavity at a temperature ensuring its molten state and flowability. The injected component is then debound using a solvent, catalytic, or thermal debinding process; finally, it is sintered to promote solid-state diffusion of powder particles in order to densify the part and obtain a final strength and density close to that of the equivalent wrought material (Omar, Ibrahim, Sidik, Mustapha, & Mohamad, 2003; Pachauri & Hamiuddin, 2016; L. Zhang et al., 2015). One of the most critical stages driving successful molding is the feedstock formulation. This stage determines the wettability, flowability, complete mold filling, powder-binder homogeneity, and proper final binder burnout needed to achieve optimal part quality.

In PIM, moldability represents the capability of a molten feedstock to fill a mold cavity. It depends on the feedstock rheological behavior, primarily determined by the binder system and its interaction with the powder particles. A typical binder consists of a primary constituent mainly composed of waxes and several additives, such as surfactants and dispersants; there is also a secondary constituent composed of long-chain or backbone polymers. Each binder constituent plays a specific role in promoting feedstock stability, moldability, and homogeneity. Each PIM process falls under one of two different technologies: high-pressure powder injection molding (HPIM) and low-pressure powder injection molding (LPIM), depending on the process' binder systems. In HPIM, the feedstock viscosity is mainly defined by its secondary binder constituents and varies from 100 to 1000 Pa·s; it also requires high molding pressures (20 to 200 MPa) and temperatures (100 to 200°C). The subsequent debinding is generally performed in two steps, during which the primary and backbone constituents are usually removed using solvent and thermal treatment. Since LPIM feedstocks, for their part, do not contain such backbone polymers, their viscosity is determined by the

waxes and short-chain polymers varying between 1 and 50 Pa·s and requires lower molding pressures (0.5 to 5 MPa) and temperatures (60 to 120°C) than HPIM. During debinding, all binders contained in LPIM green parts are generally removed in a single step using the wicking debinding approach (Gorjan et al., 2010; Toy, Palaci, & Baykara, 1995).

Independently of the injection and debinding techniques used in HPIM or LPIM, the debound parts are finally sintered using a high-temperature furnace under vacuum, reactive, or protective atmospheres. Although the PIM process is well adapted for producing metallic and ceramic components, nearly 90% of global production capacity is dedicated to metal part manufacturing, known as the metal injection molding (MIM) process (D. F. Heaney, 2019). In this context, iron-based powders are widely used in the MIM processes due to their soft magnetic properties. They are further also used as cost-effective raw materials in master alloys for the fabrication of intricate parts in the medical and electronic sectors (Demétrio et al., 2013; Friederang & Schlegel, 1999; Ma, Qin, Zhang, Zhang, Tian, Zhang, Li, et al., 2013; Ma, Qin, Zhang, Zhang, Tian, Zhang, & Qu, 2013).

Without a doubt, spherical carbonyl iron powders (CIP) dominate the MIM market for this material. As a pioneer in developing CIP for MIM, Hens et al. (Hens et al., 1989) studied the impact of binder constituents on the final part properties. They confirmed that the high content of a backbone polymer does not significantly increase the green strength of molded parts, whereas the surfactant agent enhances the feedstock moldability. A decade later, Li et al. (Li et al., 1999) demonstrated that MIM technology can be used to produce new alloys (e.g., Fe-2Ni) from an initial premix of CIP and pure nickel powders. Ahn et al. (Ahn, Park, Lee, Atre, & German, 2009) compared one CIP with several stainless steel feedstocks to evaluate their rheological and thermal properties. They confirmed that the binder system's influence on the feedstock's rheological behavior is predominant, while the thermal stability of the feedstock is mostly determined by powder selection. Mariot et al. (Mariot et al., 2016) used CIP in the development of degradable biomaterials for stent applications and showed that a feedstock of 66 vol. % solids loading (above the critical loading) exhibited the highest elongation and acceptable in-vitro degradation rates. CIP has also been used extensively for the production of

micro-PIM components (Choi, Lyu, Lee, & Lee, 2014; Q. Wang, Yin, Qu, & Johnson, 2009; You, Choi, Yoon, & Lee, 2012). For instance, Choi et al. studied the rheological behavior of a trimodal particle size (micro-size combined with nano-size) iron powder feedstock and demonstrated that a critical solid loading as high as 72 vol. % can be achieved while producing a homogeneous sintered microstructure (Choi et al., 2017). The above efforts to maximize the mechanical properties of MIM iron-based parts primarily involved using spherical powders in feedstock and the arbitrary and non-systematic selection of binder constituents.

Since the powder potentially represents up to 50% of the total manufacturing cost, the use of more economical water-atomized powder presents an interesting opportunity to reduce the cost of MIM parts (German, 2003). Unfortunately, to our knowledge, scant attention has been paid to the suitability of an irregular water-atomized iron powder for MIM in the literature, even though examples of such considerations exist. For example, Rane et al. (Kedarnath K. Rane & Date, 2014) compared the flowability of high-viscosity feedstocks prepared from spherical and irregular powders and found that lubricants, such as graphite, can be added to the irregular powder to reduce the inter-particle friction and improve the feedstock moldability. More recently, Ali et al. (M. Ali & Ahmad, 2020) proposed fabricating soft magnetic Fe-50Ni alloys from an initial blend of irregular pure iron and spherical pure nickel powders. After determining the optimal solids loading at 58 vol. %, the authors confirmed that a mixture containing irregular iron and spherical nickel powders in a 1-to-1 ratio could successfully be injected. Finally, over the past two decades, significant progress has been demonstrated with respect to the LPIM of irregular ceramic powders (Hausnerova, Kasparkova, & Hnatkova, 2016; Hidalgo, Jiménez-Morales, & Torralba, 2012; Tseng, Liu, & Hsu, 1999; Wen, Liu, Xie, Lou, & Yang, 2018).

Notwithstanding the above, the use of irregular water-atomized iron powder in LPIM and the impact of each binder constituent on the moldability of powder-binder mixtures has never been demonstrated. Therefore, this study aims to develop new iron-based feedstocks and investigate

the effect of binder constituents and solids loading on the flow properties of irregular iron-based feedstocks in the context of their use in the LPIM process.

4.3 Experimental procedures

4.3.1 Materials

The metal powder used in this study, provided by Rio Tinto Metal Powders (Sorel-Tracy, QC, Canada), is an in-development, primarily water-atomized iron powder. A high-energy milling process was used to further reduce the particle size distribution (PSD), followed by screening using a 325 mesh to eliminate particles over 45 μm in size. A scanning electron microscope (SEM, Hitachi 3600, secondary electron detector) and a laser diffraction particle sizing analyzer (Coulter LS13 320 Beckman) were used to evaluate the powder morphology and quantify the particle size distribution, respectively. The powder particles exhibited irregular and angular morphology generally expected of powders produced by water atomization (See Figure 4.1a). The irregular powder shape is generally due to the high water pressure and cooling rate associated with this low-cost large volume atomization approach. The particle size distribution characterized by D10, D50, and D90 of 1.8, 16.6, and 44.1 μm, respectively, were extracted from the cumulative particle size distribution curve reported in Figure 4.1b.

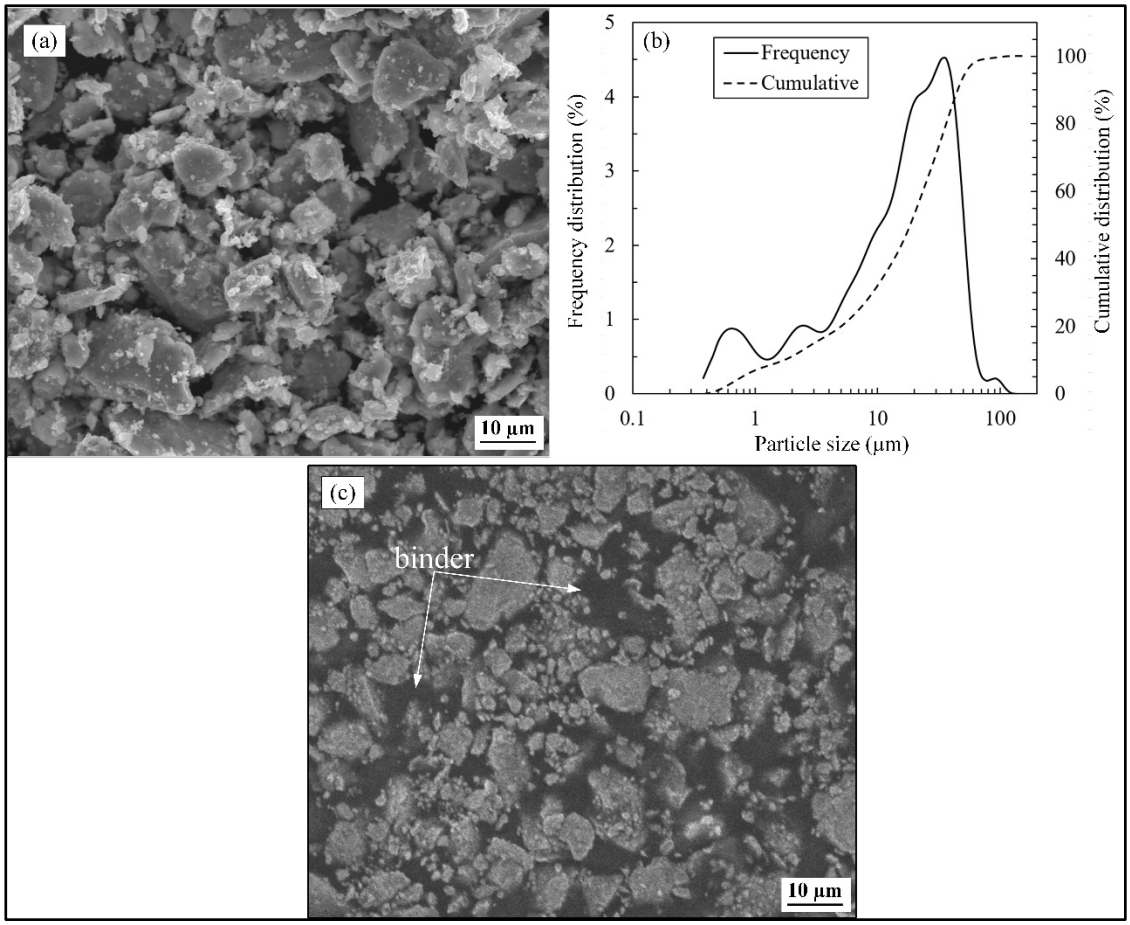

Figure 4.1 (a) SEM micrograph of iron powder, (b) powder particle size distribution curves, and (c) SEM micrographs of a typical PW-1SA-2EVA Feedstock

The binder was formulated from paraffin wax (PW) used as the main carrier, and four other additives: stearic acid (SA), beeswax (BW), ethylene-vinyl acetate (EVA), and carnauba wax (CW). These polymeric constituents were selected due to their extensive use in LPIM to form a homogeneous powder-binder mixture as illustrated in Figure 4.1c. The density of the metallic powder, binder, and feedstock formulations was measured using an AccuPyc II 1340 helium gas pycnometer according to the ASTM B923-16 standard (ASTM B923 - 16, 2016), while the melting point of each binder constituent was evaluated using a Perkin Elmer Pyris 1 Differential Scanning Calorimetry (DSC) according to the ASTM D3418-15 standard (Materials, 2015). The powder and binder characteristics are reported in Table 4-1.

Table 4-1 Characteristics of feedstock constituents

Constituent	Melting point (°C)	Density (g/cm3)	Source
Iron powder	-	7.4	Rio Tinto Metal Powders
Paraffin wax (PW)	54.0	0.90	Sigma-Aldrich
Beeswax (BW)	65.0	0.96	Sigma-Aldrich
Stearic acid (SA)	67.0	0.90	Sigma-Aldrich
Ethylene-vinyl acetate (EVA)	49.0	1.00	DuPont Elvax, MFI=52 g/10min, VA comonomer content= 40%
Carnauba wax (CW)	84.5	1.00	Sigma-Aldrich

4.3.2 Feedstock Formulation, Characterization, and Injection.

In this work, 36 different feedstocks were formulated by varying the binder constituents, their proportions, and solids loading (Table 4-2). Based on trends discovered in our previous work (G. Ali, Demers, Côté, & Demarquette, 2020; Demers, Turenne, & Scalzo, 2015), these specific feedstock formulations were selected to capture (if applicable) threshold proportions triggering the expected effects (e.g., surfactant or thickening effects), which are generally affected by binders solubility. The mixtures are referenced by their polymer volume fractions (vol. %) determined at room temperature. For example, feedstock #1 (49.9PW-0.1SA) is a mixture containing 50.0 vol. % of powder with 49.9 vol. % of paraffin wax (PW) and 0.1 vol. % of stearic acid (SA). During the development phase of the feedstock formulations (identified as phase #1 in Table 4-2), the solids loading was set at 50 vol. % of powder while the binder constituents were systematically varied one at a time to determine the effect of each constituent. Note that this solids loading represents a typical value for irregular powders used in LPIM (Deng et al., 2019; Hnatkova, Hausnerova, & Filip, 2019).

Table 4-2 Volume fractions of the powder and polymers used for feedstock formulations

Phase	Feedstock #	Solid Loading (vol. %)	Feedstock identification	Vol. %				
				Paraffin wax (PW)	Stearic acid (SA)	Beeswax (BW)	Ethylene vinyl acetate (EVA)	Carnauba wax (CW)
#1	1	50	49.9PW-0.1SA	49.9	0.1	-	-	-
	2		49.8PW-0.2SA	49.8	0.2	-	-	-
	3		49.5PW-0.5SA	49.5	0.5	-	-	-
	4		49.0PW-1.0SA	49.0	1.0	-	-	-
	5		48.0PW-2.0SA	48.0	2.0	-	-	-
	6		45.0PW-5.0SA	45.0	5.0	-	-	-
	7		40.0PW-10.0SA	40.0	10.0	-	-	-
	8		49.8PW-0.2BW	49.8	-	0.2	-	-
	9		49.5PW-0.5BW	49.5	-	0.5	-	-
	10		49.0PW-1.0BW	49.0	-	1.0	-	-
	11		48.0PW-2.0BW	48.0	-	2.0	-	-
	12		45.0PW-5.0BW	45.0	-	5.0	-	-
	13		40.0PW-10.0BW	40.0	-	10.0	-	-
	14		48.8PW-1SA-0.2EVA	48.8	1.0	-	0.2	-
	15		48.5PW-1SA-0.5EVA	48.5	1.0	-	0.5	-
	16		48.0PW-1SA-1.0EVA	48.0	1.0	-	1.0	-
	17		47.0PW-1SA-2.0EVA	47.0	1.0	-	2.0	-
	18		46.0PW-1SA-3.0EVA	46.0	1.0	-	3.0	-
	19		45.0PW-1SA-4.0EVA	45.0	1.0	-	4.0	-
	20		44.0PW-1SA-5.0EVA	44.0	1.0	-	5.0	-
	21		46PW-1SA-2EVA-1CW	46	1	-	2	1
	22		45PW-1SA-2EVA-2CW	45	1	-	2	2
	23		42PW-1SA-2EVA-5CW	42	1	-	2	5
	24		37PW-1SA-2EVA-10CW	37	1	-	2	10
#2	25	50	49PW-1SA	49	1	-	-	-
	26	54	45PW-1SA	45	1	-	-	-
	27	58	41PW-1SA	41	1	-	-	-
	28	50	47PW-1SA-2EVA	47	1	-	2	-
	29	54	43PW-1SA-2EVA	43	1	-	2	-
	30	58	39PW-1SA-2EVA	39	1	-	2	-
	31	50	45PW-1SA-2EVA-2CW	45	1	-	2	2
	32	54	41PW-1SA-2EVA-2CW	41	1	-	2	2
	33	58	37PW-1SA-2EVA-2CW	37	1	-	2	2
	34	60	35PW-1SA-2EVA-2CW	35	1	-	2	2
	35	64	31PW-1SA-2EVA-2CW	31	1	-	2	2
	36	68	27PW-1SA-2EVA-2CW	27	1	-	2	2

The binder constituents and range of proportions were selected based on their extensive use in the LPIM process (Amin, Jamaludin, & Muhamad, 2009; Gonçalves, 2001; Rei et al., 2002). Paraffin wax (PW) was used as the carrier binder to ensure the fluidity of the feedstocks. The surfactant agent is a secondary constituent added to the carrier binder to increase the powder-binder interaction, promote the homogeneity of the mixture, and decrease the viscosity of the feedstock. Stearic acid (SA) is undoubtedly the most commonly used surfactant agent (Fan et al., 2013; Hu, Liu, & Xie, 2016; Novak, Vidovič, Sajko, & Kosmač, 1997). However, due to

the robust coupling effect of SA, with its polar/nonpolar natural ends, the addition of large quantities of this constituent may lead to a higher residual carbon content due to its adsorption on the powder surface (LI, LIU, LUO, & YUE, 2007). In this context, the resulting bonding created by SA on the particle surface may decrease the debinding rate (Herranz, Nagel, Levenfeld, & Zauner, 2004; Tseng et al., 1999). Furthermore, as the quantity of SA increases, its evaporation during the mixing stage produces microscopic bubbles that must be removed from the feedstock by an extensive vacuum cycle before injection (Chan & Lin, 1995; Lin & German, 1994; Janete Eunice Zorzi, Perottoni, & Jornada, 2003). Therefore, the surfactant performance of beeswax (BW) for this irregular iron-based powder was also investigated. Accordingly, the proportion of surfactants (SA or BW) in paraffin wax (PW) was varied from 0.1 to 10 vol. % to determine the threshold ratio promoting the flowability of the powder.

In LPIM, ethylene-vinyl acetate (EVA) is generally used in small quantities to thicken the feedstock and tailor the viscosity to a level that maintains the feedstock homogeneity. From a molding perspective, the quantity of this thickening agent should be high enough to minimize the segregation phenomenon occurring before or during injection due to gravity and/or shear deformation rate gradients; it should also be low enough to maintain the feedstock viscosity as low as possible to guarantee high flowability. EVA was thus added into the PW-SA binder in proportions varying from 0.2 to 5 vol. % while molding performance was studied by monitoring viscosity evolution at constant and varying shear rates. Generally used in LPIM feedstocks to increase the green strength, carnauba wax (CW) also exhibits a shrinking effect, facilitating part demolding after injection. Different proportions of CW, ranging from 1 to 5 vol. %, were thus added to PW-SA-EVA binder formulations to quantify its impact on viscosity.

Finally, following the moldability study described below, three specific binder formulations were selected to optimize the solids loading and determine the moldability performances of the respective feedstocks (identified as phase #2 in Table 4-2). Accordingly, additional feedstocks with solids loading ranging from 50 to 68 vol. % were formulated, characterized using a pycnometer to identify the critical powder contents and calculate their moldability indices.

The feedstock viscosity was measured using an Anton Paar MCR 302 rotational rheometer and a concentric cylinder cell (C-PTD200) with a Peltier temperature-controlled measuring system at temperatures ranging from 70 to 100°C and shear rates ranging from 0.5 to 2000 s^{-1}. This temperature range was selected to calculate the activation energy for viscous flow, as described below. The minimum and maximum temperatures for the rheological tests were set respectively at 70°C (i.e., slightly higher than the melting point) to guarantee the molten state of feedstocks, and at 100 °C, to avoid feedstocks evaporation. At low solid loading (i.e., 50 vol. % of powder), all rheological tests were performed at 70°C to prevent any binder degradation. At high solid loading (i.e., 58 vol. % of powder), the viscosity measurements and injection tests were performed at 90°C; (injection of such highly loaded feedstocks at temperatures lower than 90°C was not possible).

Considering the low viscosity of LPIM feedstocks, which makes them practically impossible to test using the capillary rheometer approach, they were tested using the concentric cylinder configuration, which allows obtaining well-defined shear stress and shear rate values with such feedstocks (Shaw, Ph, Kulkarni, & Shaw, 2015). First, the feedstock, cylinder, and container were preheated according to the method developed in a previous study (Fareh, Demers, Demarquette, Turenne, & Scalzo, 2017) to prevent segregation that may occur during testing. The viscosity profiles were then used to study the impact of the binder constituents, select three feedstock formulations, calculate the moldability index, and predict the molding capability of these selected feedstocks. A laboratory-scale injection press described in another work (Lamarre et al., 2017) was finally used to inject feedstocks into the spiral mold cavity illustrated in Figure 4.2a, and moldability predictions were validated using the injected lengths calculated from the Archimedean spiral equation (equation 4.1). During injections, the mold and feedstock temperatures were set at 45 and 90°C, respectively.

$$L = \int_0^{c.2\pi} \sqrt{(a + b \cdot \theta)^2 + b^2}\, d\theta \tag{4.1}$$

where L is the injected length, a is the starting point of the spiral (a = 4.7 mm), b is the spiral increment divided by 2π (b = 1.51 mm), c is the number of turns, and θ is the angle in radians.

The injections were also performed into a typical geometry bracket mold reported in Figure 4.2b to observe the filling performance of the selected feedstocks.

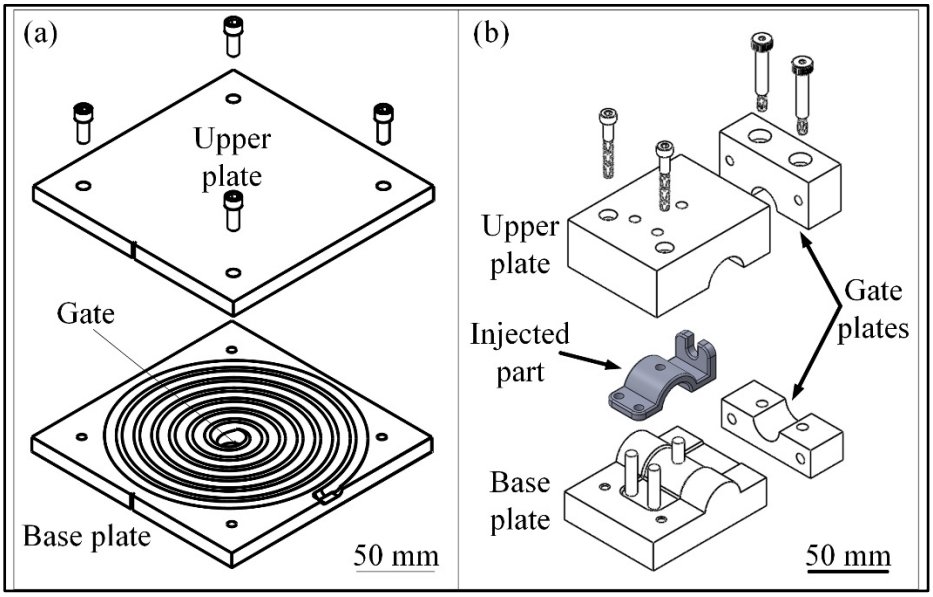

Figure 4.2 Schematic illustrations of the mold cavities for (a) spiral and (b) bracket geometries, both injected into a mold at 45 °C, using a feedstock at 90 °C

4.4 Results and discussion

4.4.1 Development and selection of binder formulations

Influence of the surfactant agents on viscosity

For a single constituent PW-based feedstock (i.e., a powder content at 50 vol. % containing no SA or no BW), the feedstock behaved like a quasi-solid for which the melt viscosity could only be measured at high temperatures. The reference viscosity profile for a feedstock containing only PW is identified as 50PW (Ref) in Figure 4.3a-b, where it is shown for reference only since it was measured at 120°C. The viscosity of all feedstocks decreases with an increase in the shear rate, which corresponds to the shear thinning behavior attributable to the breaking up of agglomerates, particle ordering, and binder molecule alignment with the flow (Foong &

Tam, 1998). This rheological behavior is generally suitable for LPIM since it results in a low viscosity, promoting high moldability during the injection stage (i.e., at high shear rates), and a high viscosity, minimizing segregation during the solidification stage (i.e., at low or zero shear rates).

The addition of only 0.1 vol. % of SA clearly decreases the viscosity of the single-wax feedstock and promotes feedstock flowability (Figure 4.3a). The flowability of this mixture continues to be improved with an addition of 0.2 vol. % SA in PW, but beyond this, any further increase produces no significant effect on the feedstock viscosity or on the shape of the viscosity profile. This result confirms that a value of about 0.2 vol. % represents the threshold proportion of SA in PW, which provides suitable lubricity and wettability of the irregular iron particle surface.

Similarly, BW was added to the wax-iron-based feedstocks to evaluate the effect of this constituent on viscosity. This constituent is reported in the literature to be used either as a surfactant or as a primary binder component (Karatas, Kocer, Ünal, & Saritas, 2004). At a solids loading of 50 vol. %, a minimum of 0.2 vol. % of BW was required in PW to achieve feedstock flowability (Figure 4.3b). As such, the feedstocks containing less than 0.1 vol. % of BW were too thick to be tested at that nominal solids loading. A further increase in BW produced a significant decrease in feedstock viscosity up to 2 vol. %, and a similar rheological performance was observed with additions of this surfactant agent up to 5 vol. %. However, a further increase in BW from 5 to 10 vol. % caused a slight increase in viscosity. This behavior could partially be explained by the de-agglomeration of fine particles, which may result in a slight but measurable increase in viscosity.

The results summarized in Figure 4.3c confirm that at shear rates typically experienced by LPIM feedstock during the injection phase (i.e., ~220 s^{-1}), the surfactant performance of SA is higher than that of BW. For the irregular shape wax-iron-based feedstock, the addition of only 0.2 vol. % SA into PW produces a similar effect on viscosity as the addition of 2 vol. % BW. Therefore, SA was selected as the best surfactant to be used for the subsequent feedstock

formulations. However, 0.2 vol. % of SA is difficult to experimentally control as it leads to inaccuracies related to small measured quantities, and would seem to be solids loading-dependent since additional tests (not shown in this study) confirmed that this quantity of SA was insufficient to provide appropriate lubricity at solids loading higher than 50 vol. %. Since further additions of SA did not affect the viscosity during these initial experiments, the SA proportion was set at 1 vol. % for the formulation of the subsequent feedstocks prepared in this study (i.e., feedstocks #14 to 36 in Table 4-2). Note that this threshold proportion of stearic acid creating the surfactant effect on the iron-based powder is lower as compared to the optimal amount of 2.2 vol. % proposed by Auscher et al. (Auscher, Fulchiron, Fougerouse, Périé, & Cassagnau, 2017) for zirconia-based feedstocks. However, the threshold value determined experimentally in this study is similar to the one assessed theoretically by Ali et al. (2020) to form a monolayer adsorption on stainless steel powder surface.

Repeatability measurements were performed with one feedstock (i.e., feedstock #4), and the results reported in Figure 4.3d confirmed that the average viscosity at a reference shear rate of 100 s^{-1} is about 0.3 Pa·s with a standard deviation of ±0.009 Pa·s. Since these five viscosity profiles were obtained using five different feedstock samples (i.e., one sample represents a quantity of molten feedstock poured in the rheometer, tested, and took off from rheometer), the difference in the viscosity measured was considered to be relatively small and statistically insignificant. In this context, any measurable variations in viscosity higher than ±0.009 Pa·s produced by changes in the constituent proportions were considered true variations in viscosity.

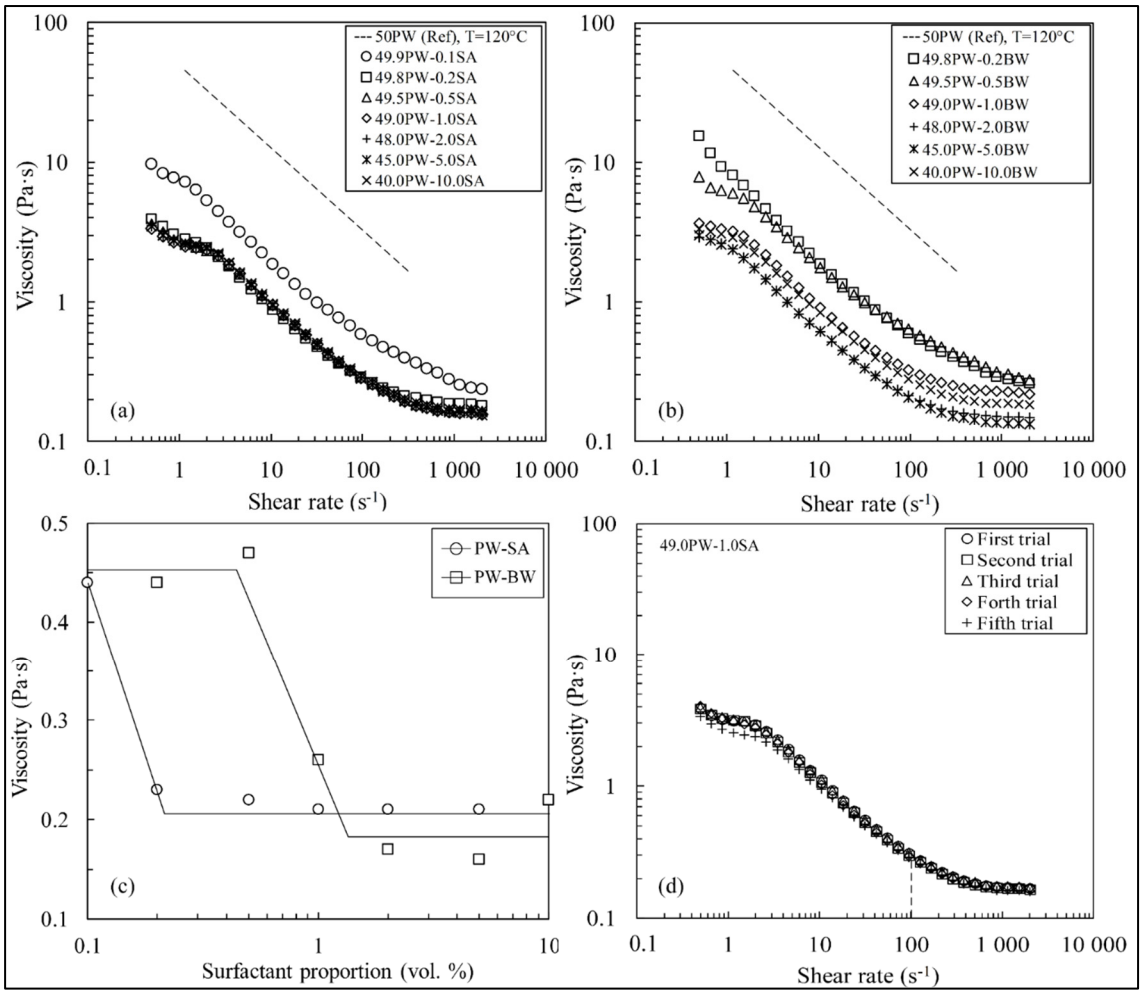

Figure 4.3 Viscosity profiles of the feedstocks formulated from (a) PW and SA, (b) paraffin wax and BW, and (c) evolution of the viscosity values at a reference shear rate of 220 s^{-1} for different surfactant proportions (solids loading=50 vol.% of powder; feedstock temperature=70 °C), and (d) repeatability of the viscosity measurements for 49.9PW-1.0SA feedstock

Influence of thickening agent on viscosity and segregation

As illustrated in Figure 4.4a, an increase from 1 to 5 vol. % of EVA in the PW-SA binder produces a proportional increase in viscosity values. Additional rheological tests were performed for feedstocks containing 0.2 to 5 vol. % EVA at a constant shear rate of 100 s^{-1} to investigate the segregation phenomenon (Figure 4.4b). Based on a testing approach developed in a previous study (Fareh et al., 2017), the testing time (60 min) and temperature (90°C) were purposefully selected to amplify the segregation phenomenon. For low EVA contents (i.e.,

open marks in Figure 4.4b designating an EVA proportion ≤ 1 vol. %), the viscosity initially remains low and constant over a time, varying from 20 to 35 minutes, depending on the EVA content, and then starts increasing until the end of the test.

During a rheological test performed on a non-thixotropic fluid, an increase in viscosity is generally explained by a separation of the powder from the binder, which produces a binder-rich area at the top region of the rheometer cup and a powder-rich area at the middle and bottom regions of the rheometer cup. Since the middle testing zone becomes richer in powder, the overall viscosity measured with the concentric cylinder cell (C-PTD200) is increased (M. Rueda, Fulchiron, Cassagnau, Prebé, & Martin, 2016). This phenomenon can be also observed using SEM technique and measured using thermogravimetric analysis where the solid loading locally increases within segregated zones (Demers, Fareh, Turenne, Demarquette, & Scalzo, 2018). For high EVA contents (i.e., black marks in Figure 4.4b designating an EVA proportion ≥ 2 vol. %), the viscosity remains almost constant over time and the vertical position of each curve depends on the EVA proportion. The wave shapes and slight decrease in viscosity visible on a few curves can be attributed to the intrinsic heterogeneity of the mixture combined with the difficulty of the measurement equipment to maintain perfectly constant temperatures over long testing periods. Considering these slight variations in the curves as measurement artifacts, 2 vol. % EVA is the lowest value minimizing segregation while having a limited detrimental effect on viscosity.

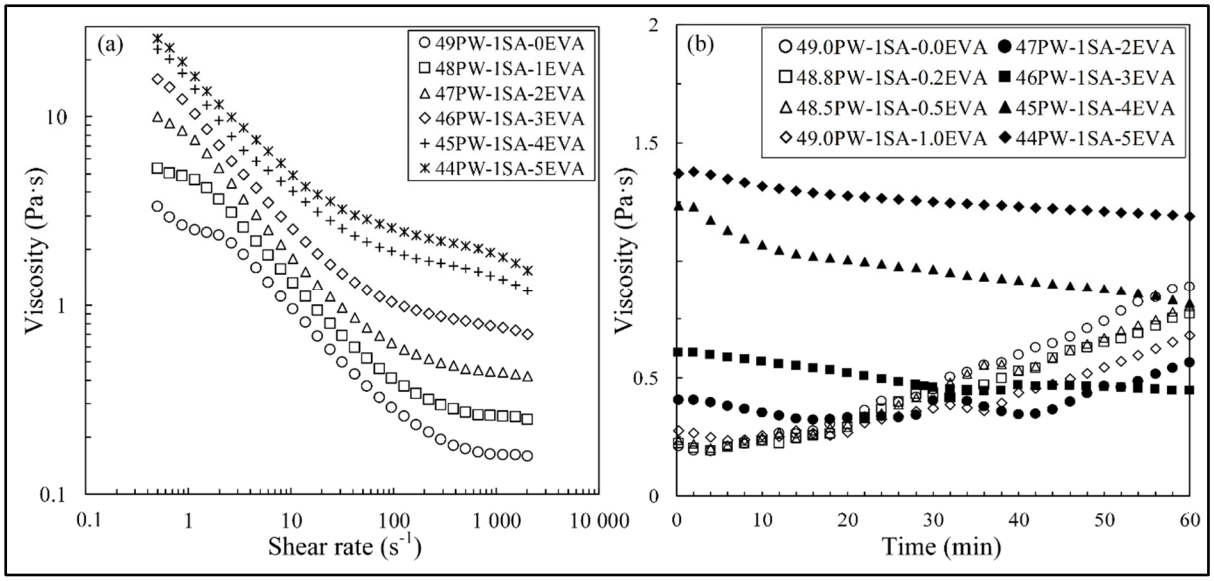

Figure 4.4 (a) Viscosity profiles of feedstocks formulated from PW-SA-EVA (solids loading=50 vol. %; feedstock temperature=70 °C) and (b) evolution of viscosity measured at $\dot{\gamma}$ increased to 90 °C to promote the segregation phenomenon

Influence of shrinking agent on viscosity

Compared to the reference PW-1SA-2EVA-0CW feedstock, adding up to 2 vol. % of CW produces no measurable change in the viscosity profile, but any further beyond that increase leads to an increase in overall mixture viscosity, as is shown in Figure 4.5. All feedstocks exhibit a suitable shear thinning behavior, confirming that this constituent can be added into LPIM iron-based feedstock in proportions equal to or below 2 vol. % with no detrimental effect on the shape of the viscosity profile or on the feedstock viscosity. A future investigation on the effect of CW on the green strength and debinding behavior (out of the scope of the current study) is required to validate this shrinking agent's threshold proportion in low-viscosity binders.

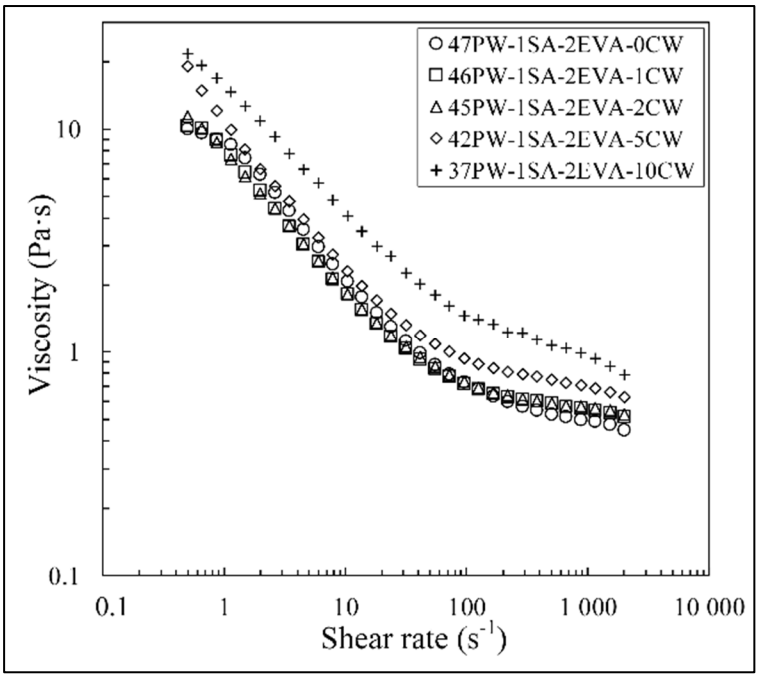

Figure 4.5 Viscosity profiles of feedstocks formulated from PW-1SA-2EVA and CW (solids loading=50 vol. %; feedstock temperature=70 °C)

4.4.2 Influence of solids loading on moldability

Quantification of maximum solids loading

Based on the feedstock development results presented above (Figure 4.3 to Figure 4.5), three binder formulations were selected to quantify the influence of the solids loading on moldability. The first PW-1SA feedstock was selected for its low viscosity values driving its high moldability potential. Since this high flowability mixture may suffer from segregation, two other feedstocks, PW-1SA-2EVA and PW-1SA-2EVA-2CW, containing thickening and shrinking agents, were also selected. Using these three binder formulations, the solids loadings were set at 50, 54, and 58 vol. % to quantify the influence of the powder volume fraction on moldability. The maximum solids loading was assessed from the evolution of the pycnometer density according to the solids loading reported in Figure 4.6. Each feedstock density was

measured three times using different samples. However, since the standard deviation of density is relatively low (0.003 g/cm^3) on average, it was decided not to report it in Figure 4.6.

For this irregular iron powder, the highest solids loading appears to be between 58 and 60 vol. %, as measured densities of ≥ 60 vol. % solids loading clearly diverge from the theoretical values (i.e., this deviated value generally indicating that the particles are closely packed but lack of binders leads to void formation). Since an abnormally high feedstock temperature of 110°C was required to formulate and blend the critical solids loading at 60 vol. %, and any increase in temperature (required for the Weir index calculation) may promote evaporation and/or chemical degradation of these kinds of wax-based binders, the maximum solids loading was set at 58 vol. %, i.e., 2 vol. % below the critical solids loading.

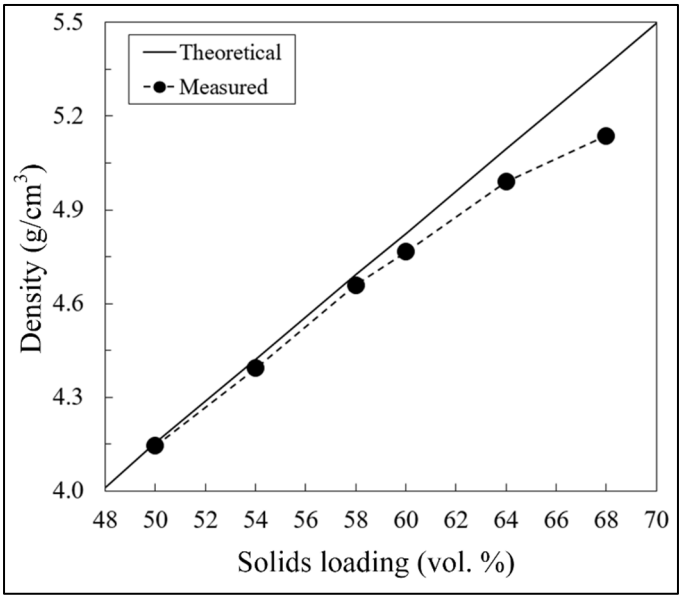

Figure 4.6 Determination of the critical solids loading using the PW-1SA-2EVA-2CW feedstock

Calculation of the moldability index

The influence of the solids loading on viscosity is presented in Figure 4.7 for the three selected binder formulations. All viscosity profiles exhibit the expected shear thinning behavior, regardless of the powder volume fraction. Although an increase in solids loading from 50 to

58 vol. % resulted in a three- to four-fold increase in viscosity, the overall viscosity remained relatively low (i.e., < 3 Pa·s) for shear rates corresponding to typical LPIM injection (e.g., 100 < $\dot{\gamma}$ < 500 s^{-1}).

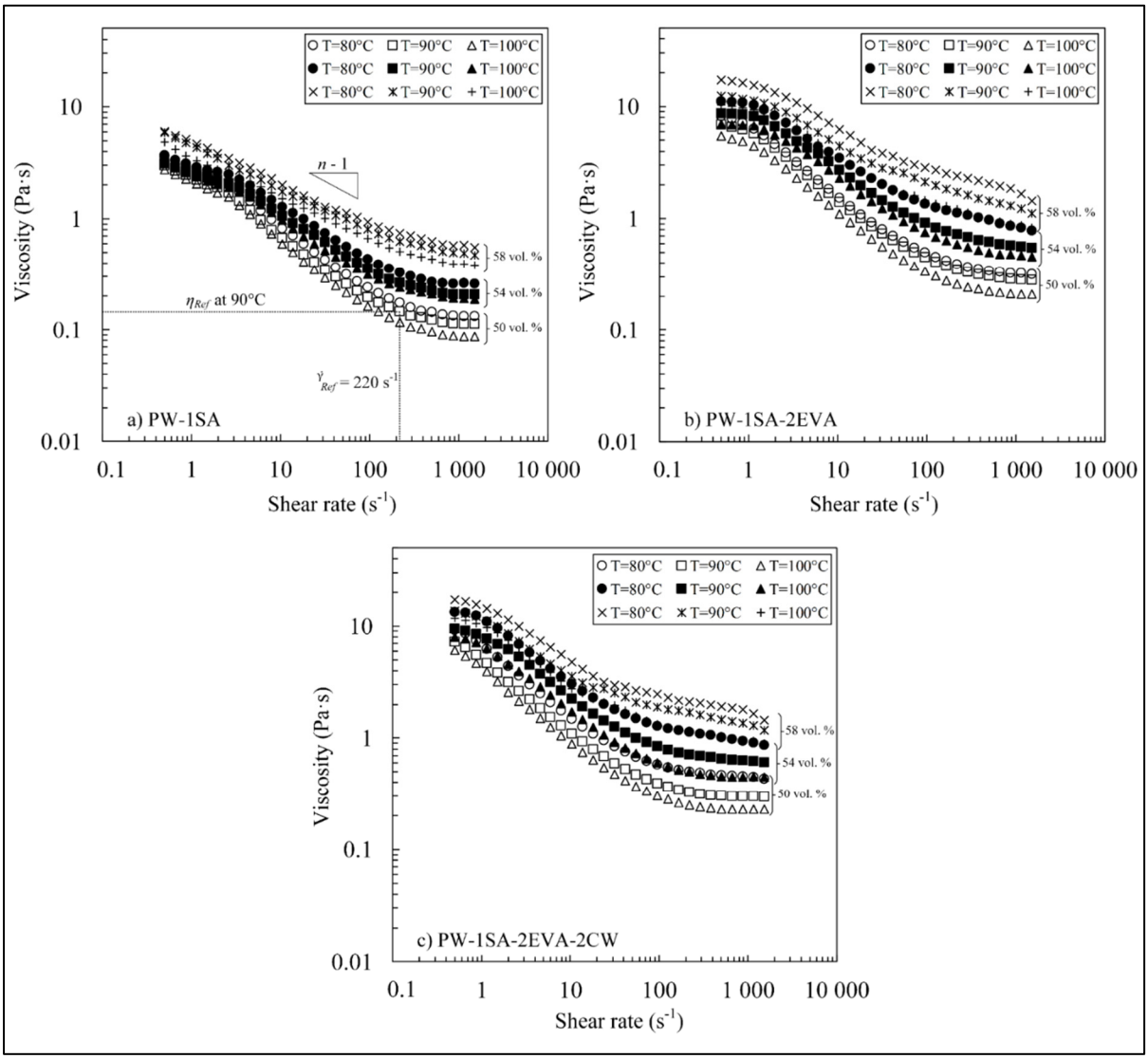

Figure 4.7 Impact of solids loading on viscosity profiles for the three binder formulations: (a) PW-1SA, (b) PW-1SA-2EVA, and (c) PW-1SA-2EVA-2CW

The Weir moldability index was calculated using equation (4.2) (Weir, 1963). The rheological parameters are extracted from the viscosity profiles in Figure 4.7.

$$\alpha_{STV} = \frac{|n-1|}{\eta_{Ref}.{}^{E}/_{R}} \tag{4.2}$$

where α_{STV} is the moldability index, η_{Ref} is the reference viscosity, n is the flow behavior index, E is the flow activation energy, and R is the gas constant. The η_{Ref} extracted directly from the viscosity profile at a shear rate typically experienced by the feedstock ($\dot{\gamma}$ = 220 s^{-1} assessed by simulations using Moldflow), as illustrated in Figure 4.7a at 90°C for the feedstock at 50 vol. % solids loading. *n* is measured by the slope of shear-thinning behavior, as indicated in Figure 4.7a. *E* is quantified by the degree of the temperature sensitivity to the feedstock viscosity and derived from the slope of the Napierian logarithmic, plotting viscosity against the inverse of temperature as presented in Figure 4.8. These three rheological parameters are summarized in Table 4-3.

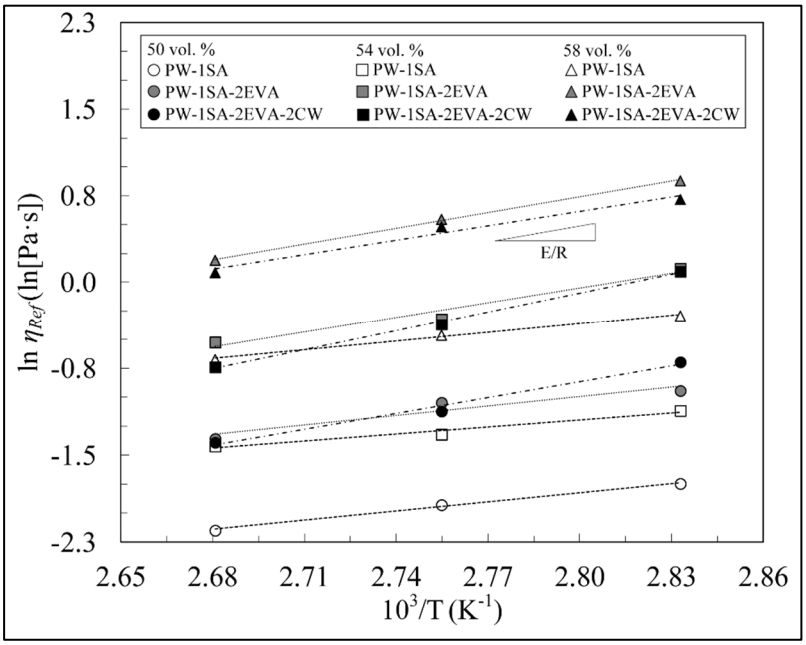

Figure 4.8 Feedstock viscosity as a function of temperature for the three selected binder formulations with different solids loadings (values plotted at $\dot{\gamma}$=220 s^{-1})

Table 4-3 Values of the rheological parameters η_{Ref}, n, and E

Binder formulation	Solids loading (vol. %)	Reference viscosity, η_{Ref} (Pa·s)	Flow behavior index, n	Activation energy, E (kJ/mol)
PW-1SA	50	0.1	0.48	22.0
	54	0.3	0.54	16.7
	58	0.6	0.66	20.9
PW-1SA-2EVA	50	0.3	0.52	22.5
	54	0.7	0.55	35.5
	58	1.6	0.66	37.8
PW-1SA-2EVA-2CW	50	0.3	0.57	38.0
	54	0.7	0.59	45.5
	58	1.6	0.72	34.7

The moldability indices calculated for each feedstock at different solids loadings are presented in Figure 4.9a. From a molding perspective, the best feedstock candidate corresponds to the highest moldability index value (i.e., to the lowest value of η_{Ref}, n, and E, concurrently). In this study, the PW-1SA feedstock produced the best moldability characteristics, while the other two feedstocks showed comparable moldability indices. As expected, the moldability index decreases as the solids loading increases and the EVA is introduced to the feedstock. It is interesting to note that although the PW-1SA-2EVA and PW-1SA-2EVA-2CW feedstock families produced similar moldability indices, the shear sensitivity indices and the flow activation energies reported in Table 4-3 are quite different.

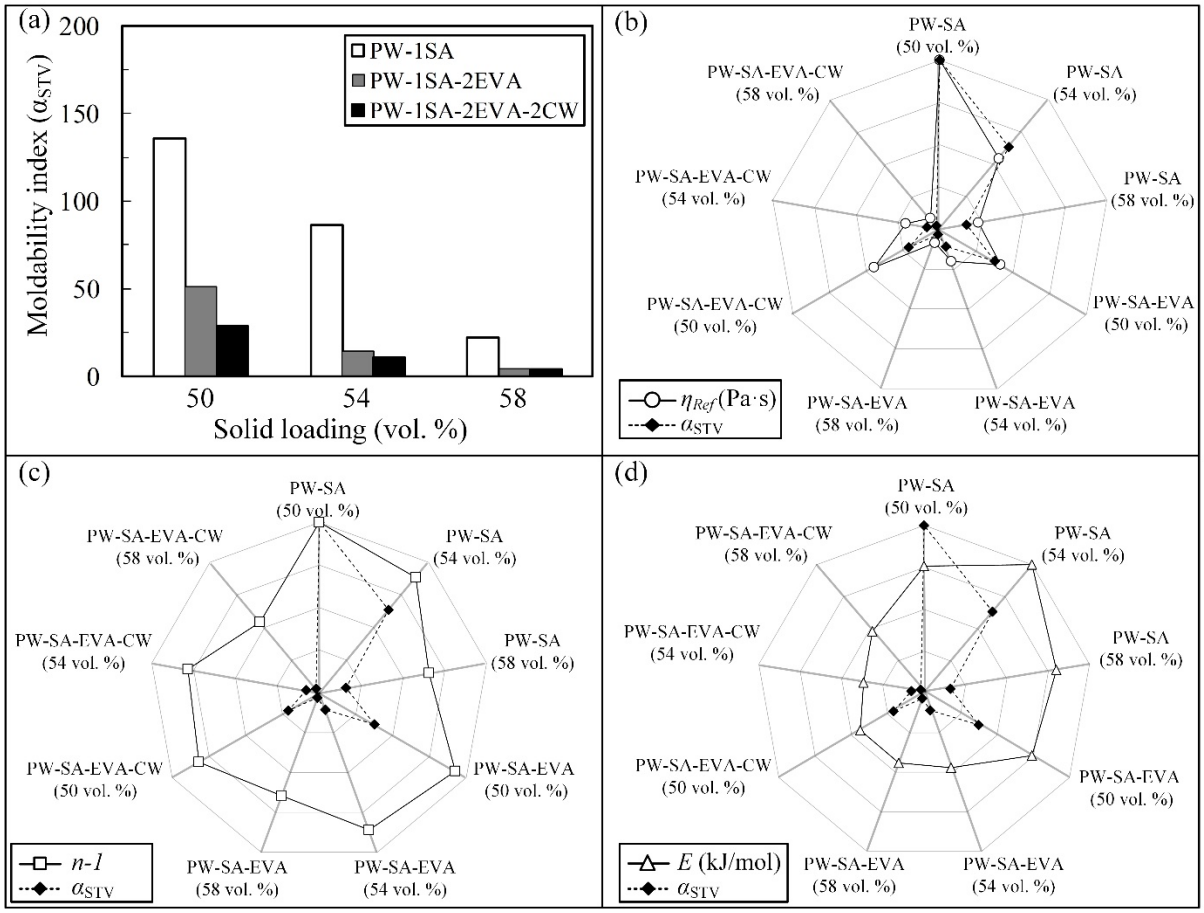

Figure 4.9 (a) Moldability indices for the selected feedstocks at different solids loadings, and (b–d) radar diagrams comparing the rheological parameters η_{Ref}, $n-1$, and E with the moldability indices

These rheological parameters were normalized concerning their best values for comparison purposes and plotted against the moldability indices in the radar diagrams shown in Figure 4.9b-d. Therefore, the external envelope and the center of the radar diagrams represent each parameter's best and worst values, respectively. The similar radar patterns drawn by the parameters α_{STV} and η_{Ref} in Figure 4.9b confirm that the viscosity values are strongly correlated with the moldability index, while that is not the case for the shear rate sensitivity index (n), as well as for the flow activation energy (E), as depicted in Figure 4.9c-d. In other words, the moldability indices used to predict the molding capability of feedstocks seem to be mostly driven by the reference viscosity (η_{Ref}).

Validation of the moldability predictions

The feedstock moldabilities predicted by the Weir index were validated using real-scale injections into a spiral mold. The injections were repeated three times for each feedstock condition, and the average injected lengths were compared with the moldability indices in Figure 4.10a. As expected, the higher the solids loading, the lower the feedstock moldability (indicated by the arrow direction in Figure 4.10) was shown to be. Interestingly, the similar injection capabilities predicted by the moldability indices obtained with the PW-1SA-2EVA and PW-1SA-2EVA-2CW feedstocks were confirmed by the comparable injected lengths. Surprisingly, the PW-1SA feedstock exhibiting the highest moldability indices produced injected lengths similar to those of other feedstocks.

According to the results reported by Mangels concluding that the injected length is inversely proportional to the viscosity of the LPIM feedstock (Mangels & Williams, 1983), the average injected lengths were plotted against the viscosity in Figure 4.10b to confirm this theory. As for previous results, it seems that the correlation between the viscosity and molding capability remains weak since modifications to the binder constituents (i.e., PW-1SA feedstock) result in significant viscosity variations, without any real changes in injection lengths. The differences observed between these two rheological models and the experiment suggest that the interaction between the feedstock and the mold is not taken into account in Weir's model, or the viscosity measurements, such as the thermal exchange, friction, solidification, etc., could play a significant role in real-scale injection results. This hypothesis will be validated using a different mold and feedstock characteristics in future work.

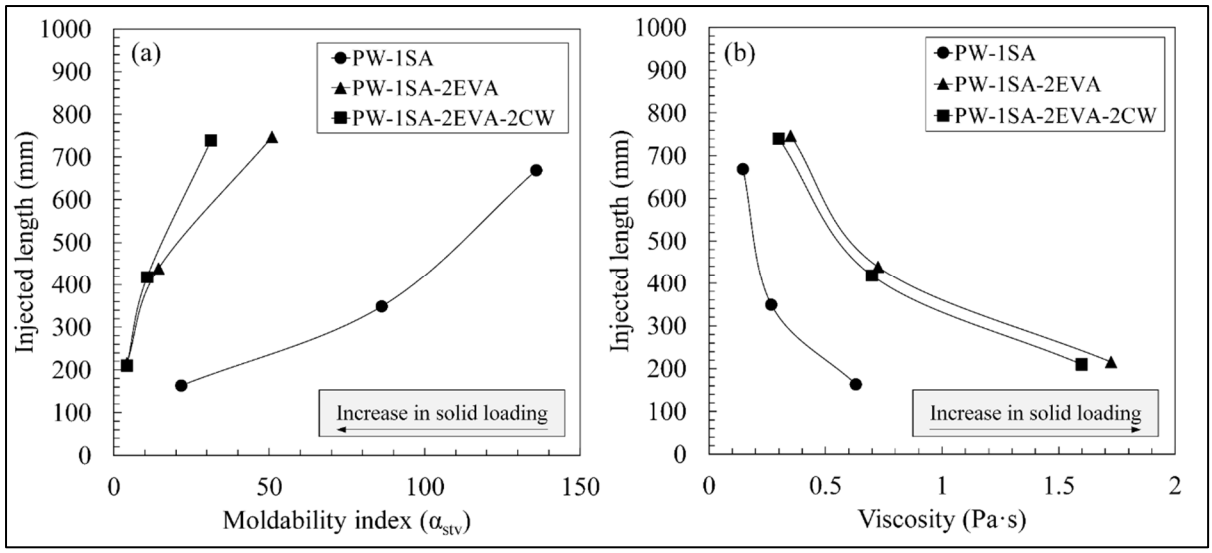

Figure 4.10 Correlation between the injected length with (a) moldability index and (b) viscosity obtained at 90 °C

The injection results illustrated in Figure 4.11a-c confirm the capability of the three feedstock formulations to be injected at a high solids loading (i.e., 58 vol. %) into a typical PIM geometry. The green parts were characterized by smooth surfaces, and an absence of flashing, voids or sink marks. However, the feedstocks containing neither EVA nor CW tended to stick to the mold walls, were difficult to demold, and were quite fragile. In fact, microcracks visible on the injected parts, and probably formed during the ejection stage (visible in Figure 4.11d), did confirm this brittleness. These surface indications confirm a lower green strength of the PW-SA feedstock, which could become a problem for handling the green part through subsequent PIM stages. In this respect, the EVA constituent might be used not only as a segregation prevention component, but also to improve the green strength, as there were no microcracks visible on the parts injected with EVA (see Figure 4.11e). The injected parts containing CW were characterized by smoother surfaces and easy demolding, thus also confirming the positive effect of CW on the molding/demolding properties; no microcracks are visible in Figure 4.11f. Therefore, from an injection perspective, EVA and CW-containing formulations correspond to highly moldable feedstocks. The influence of these binder constituents on the debinding and sintering performances is to be investigated in future work.

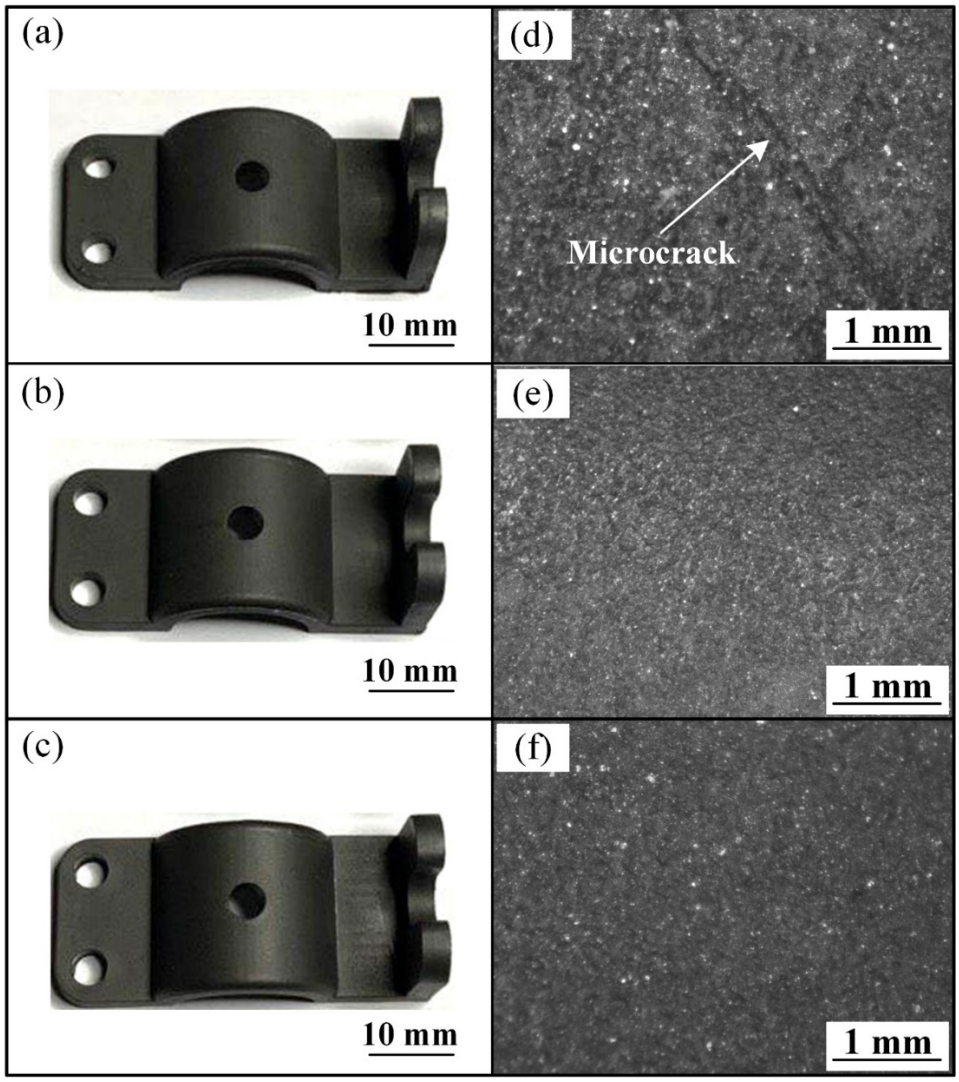

Figure 4.11 Typical green parts injected from the three feedstock formulations: (a) PW-1SA, (b) PW-1SA-2EVA, (c) PW-1SA-2EVA-2CW at 58 vol. % solids loading, and (d–e) the corresponding optical observations of the parts' surface states

4.5 Conclusions

The influence of binder constituents and solids loading on the rheological behavior and molding properties of irregular iron-based low-pressure powder injection molding feedstock was studied. A total of 36 different feedstocks formulated from one irregular iron-based powder (D50 = 16.6 μm) and different wax-based binder systems (paraffin wax combined with

a surfactant, thickening, and shrinking agents) were obtained for three different solids loadings (50, 54, and 58 vol. %). The viscosity profiles were used to quantify the threshold proportions of each binder constituent, to identify the three best feedstock candidates, calculate their moldability indices validated using real-scale injections into a spiral mold, and finally, injected into a typical mold cavity to demonstrate the molding capability of the new feedstock formulations. The conclusions are summarized as follows:

- The viscosity profiles confirmed that all feedstocks exhibit a suitable shear thinning behavior maximizing the feedstock moldability with low viscosity values varying from 0.3 to 3 Pa·s during injection (e.g., at shear rates > 100 s^{-1}), and minimizing segregation with high viscosity values varying from 6 to 20 Pa·s during solidification (i.e., at a shear rate close to zero).
- A threshold proportion as low as 0.2 vol. % stearic acid in paraffin wax-based feedstock was enough to produce the surfactant effect on the irregular iron particle surface. Beeswax generated a significantly smaller surfactant effect: 2 vol. % beeswax must be added in paraffin wax to produce an equivalent effect to that of 0.2 vol. % stearic acid surfactant.
- Used as a thickening agent, a minimum proportion of about 2 vol. % ethylene-vinyl acetate in a paraffin wax-based binder was required to minimize the powder-binder segregation.
- Used as a shrinking agent, up to 2 vol. % carnauba wax added generated no negative impact on viscosity, while facilitating the demolding operation and producing smooth green part surfaces.
- Although Weir's model was successfully used to predict the impact of solids loading on molding properties, the high moldability anticipated with the feedstock containing no ethylene-vinyl acetate or carnauba wax (i.e., PW-1SA producing 3-4 times higher αSTV) was not confirmed with this rheological approach.
- From a molding/demolding perspective, the best feedstock candidate was the mixture formulated with the maximum achievable solids loading (i.e., 58 vol. % powder) containing paraffin wax, stearic acid, ethylene-vinyl acetate, and carnauba wax (i.e.,

PW-1SA-2EVA-2CW). In this respect, the green parts were characterized by smooth surfaces, no apparent flashing, and an absence of cracks, voids or sink marks.

4.6 Acknowledgment

This work was carried out with the financial support of the Natural Sciences and Engineering Research Council of Canada. The authors want to thank Mr. Freddy Salliot, Mrs. Maylis Perre, and Mrs. Emma Darrou for their collaboration in experimental injection tests.

CHAPTER 5

EFFECT OF THERMAL DEBINDING CONDITIONS ON THE SINTERED DENSITY OF LOW-PRESSURE POWDER INJECTION MOLDED IRON PARTS

A. A. Tafti [a], V. Demers [b], Seyed Mohammad Majdi [a], G. Vachon [c], V. Brailovski [b]

[a, b] Department of Mechanical Engineering, École de Technologie Supérieure, 1100 Notre-Dame West, Montreal, Quebec, Canada, H3C 1K3
[c] Research and Development, Rio Tinto Metal Powders, 1625 route Marie-Victorin, Sorel-Tracy, Quebec, Canada, QC J3R 4R4

Paper published in *Metals,* February 2021

5.1 Abstract

Low-pressure powder injection molding (LPIM) is a cost-effective technology for producing intricate small metal parts at high, medium, and low production volumes in applications which, to date, have involved ceramics or spherical metal powders. Since the use of irregular metal powders represent a promising way to reduce overall production costs, this study aims to investigate the potential of manufacturing powder injection molded parts from irregular commercial iron powders using the LPIM approach. To this end, a low-viscosity feedstock was injected into a rectangular mold cavity, thermally wick-debound using three different pre-sintering temperatures, and finally sintered using an identical sintering cycle. During debinding, an increase in pre-sintering temperature from 600 to 850°C decreased the number of fine particles, which resulted in a decrease in the sintered density from 6.2 to 5.1 g/cm3, an increase in average pore size from 9 to 14 μm, and a decrease in pore circularity from 67 to 59 %.

Keywords: Low-pressure powder injection molding (LPIM), debinding, pre-sintering temperature, sintering, iron powder, irregular particles

5.2 Introduction

Powder injection molding (PIM) has been emerging as an alternative technology to conventional powder metallurgy thanks to its numerous strong points, such as high shape complexity and productivity, good precision, and adequate surface quality (German, 2013; German & Bose, 1997; Hamidi et al., 2017). In ceramic injection molding (CIM) or metal injection molding (MIM), ceramic or metallic powders are mixed with a polymeric binder to form molten feedstocks that are injected into a mold cavity at a given injection pressure. During subsequent debinding and sintering processes, the binder is removed from the injected components, which are finally densified to obtain final products (Checot-Moinard, Rigollet, & Lourdin, 2011; M. M. Rueda et al., 2017). Although each processing stage is important, powder-binder formulation and binder removal are critical steps driving the final chemical composition and mechanical properties of PIM parts (Enneti, Onbattuvelli, Gulsoy, Kate, & Atre, 2019; D. F. Heaney, 2019).

In conventional high-pressure powder injection molding (HPIM), the binder, which consists of a blend of low- and high-molecular-weight polymers (also called primary and secondary binders, respectively), is removed in two steps. During the first step, the primary binder is extracted either by a solvent (Hayat et al., 2017; Hayat, Wen, Zulkifli, & Cao, 2015; K. K. Rane & Date, 2020), a supercritical fluid such as supercritical carbon dioxide (Chartier, Ferrato, & Baumard, 1995; Royer et al., 2018), or a catalyst such as highly concentrated nitric acid (Attia et al., 2014; Krug, Evans, & Ter Maat, 2002), depending on the binder system and powder characteristics. During the second step, the secondary binder, acting as a backbone to retain the shape, is removed during a final burnout cycle before the sintering process (Hayat et al., 2018; J. M. Park et al., 2018). During the MIM process, several chemical reactions, such as oxidation, reduction, carburization, and decarburization, may occur during debinding and sintering, which could affect the magnetic, electric, physical, and mechanical properties of the parts. In addition, since the carbon content determines the properties of iron-based systems, debinding, and sintering processes need to be carefully designed to minimize undesirable chemical reactions.

Ho et al. (Ho & Lin, 1995) investigated the decomposition behavior of a carbonyl iron powder (CIP) feedstock using one-step thermal and two-step solvent/thermal debinding routes. Using the same thermal debinding conditions (i.e., debinding at 500°C under a hydrogen atmosphere), they confirmed that the carbon content was better controlled during a two-stage solvent/thermal debinding compared to the one-step thermal debinding route. Applying a similar two-step debinding approach to an iron-based feedstock, Hwang et al. (Hwang, Hsieh, & Shu, 2002) successfully extracted the primary soluble binder through a heptane bath, followed by a final burnout of the backbone polymer during thermal debinding under different N_2-H_2 atmospheres. They highlighted that an increase in the hydrogen proportion significantly affects the carbon content, directly impacting the final sintered densities. Lee et al. (Lee, Choi, Jeung, & Moon, 1999) studied the effect of debinding parameters, such as the temperature and heating rate, on the residual carbon content in different neodymium-iron-boron feedstock formulations. Using a one-step thermal debinding approach, they demonstrated that the use of slower heating rates (<1 K/min) and higher debinding temperatures (from 270 to 500°C) was effective in maintaining a low carbon content which affects the magnetic properties of sintered specimens.

In low-pressure powder injection molding (LPIM), a low-viscosity multi-component binder provides high molding capability while generating suitable powder-binder interactions, feedstock stability, and low segregation occurrence. The binder system, which does not contain a high melting point backbone polymer, is generally composed of wax-based carriers, surfactants, and thickening agents providing a feedstock viscosity typically below 20 Pa·s, which requires an injection pressure below 1 MPa (i.e., 50 to 200 times lower than the pressure required in HPIM) (Sardarian, Mirzaee, & Habibolahzadeh, 2017). This low injection pressure streamlines the production process by decreasing the size of injection machines and the overall tooling size (as compared to reciprocating screw press and massive molds used in conventional HPIM), leading to a cost-effective fabrication of intricate parts, either in low- or high-production volumes (Mangels, 1994; Sajko, Kosmač, Dirscherl, & Janssen, 1997). However, in the absence of a backbone binder, one of the main challenges encountered in the LPIM process is shape retention and a lack of brown strength since all the binder components are

removed in just a single step during a thermal wick debinding stage. For LPIM feedstock, the approach consists of embedding the injected parts into a wicking powder bed (e.g., graphite, alumina, or other inert powders) and heating it up to the pre-sintering temperature under a protective atmosphere. The powder bed acts as a wicking medium to withdraw the molten binder out of the heated part and as a physical support maintaining the weak debound structure up to the pre-sintering of powder particles. In thermal wick debinding, the most critical parameters include a wicking medium pore size, debinding temperature, heating rate, protective atmosphere, and pre-sintering temperature, which must be all set to ensure the proper binder extraction, while avoiding undesirable stresses, distortions, defects, or chemical reactions (Patterson & Aria, 1989).

As a pioneer in this field, German (German, 1987) described the mechanisms governing thermal wick debinding and the two distinct structures of the binder through the powder network. On the one hand, a significant amount of the molten state binder is extracted from the injected parts by capillary forces as a connected liquid (also called the funicular state) within the porous wicking bed. On the other hand, while binder regions become isolated, residual binder remains trapped within the part (also called the pendular state). During a heating ramp-up to the pre-sintering temperature, the binder is completely decomposed regardless of the location (i.e., inside the part, as pendular bonds, or outside of the part within the wicking media). Based on this model, an evolution of binder content is expected at different times of the process (e.g., at different debinding short shots) where the center of the part becomes poorer in binder, while the wicking bed becomes richer in binder. Using an alumina-based LPIM feedstock, Gorjan et al. (Gorjan et al., 2010) experimentally confirmed this evolution in binder content and the formation of distinct rich and poor binder zones within the part using interrupted debinding cycles. Following the binder exudation occurring at the early debinding stage due to a sudden change in binder volume, they suggested that a molten binder could be either mobile or immobile, depending on the part and wicking powder pore sizes. However, other experimental data obtained by some research groups showed few inconsistencies with this model. Somasundram et al. (Somasundram, Cendrowicz, Wilson, & Johns, 2008) studied the mechanisms of thermal wick debinding for a zirconia-based LPIM commercial feedstock

using an experimental approach. They observed a homogenous distribution of the binder through the parts during the debinding stage and concluded that the binder was extracted concurrently from the bigger and smaller pores in the compact regardless of the location within the part. Kim et al. (Kim, Lee, Song, & Kim, 1996) used a commercial silicon nitride-based LPIM feedstock to study the effect of additives on the capillary extraction forces during thermal wick debinding treatment. They observed that binder systems containing ethylene-vinyl acetate behaved differently from those containing polyethylene wax in terms of capillary extraction, weight loss, and debinding rate. The study also concluded that the transition from the funicular to pendular states, as well as the capillary structure, are significantly affected by the binder homogeneity regardless of the location of the binder within the part. According to these approaches used to describe the debinding mechanisms, it seems that there are no universal analytical models that can be directly applied to all powder/binder system to predict the physical phenomena occurring during thermal wick debinding.

As an alternative, thermogravimetric analysis (TGA) has been used extensively to assess the effect of binder constituents and debinding atmosphere on the binder degradation behavior. Combined with other experimental techniques, the decomposition temperature ranges obtained with a TGA can be used directly to design thermal debinding cycles (Hwang & Tsou, 1992; Xianfeng et al., 2019). For instance, Xie et al. (Xie et al., 2020) used TGA analysis coupled with FTIR spectrometry (TG-FTIR analysis) to quantitatively study and design the thermal debinding cycle for HPIM zirconia-based feedstocks and evaluate the effect of binder composition, degradation rate, degradation temperature range, and degradation products on the quality of debound parts. W.-K. You et al. (You et al., 2012) used the TGA approach to design a thermal wick debinding cycle adapted to spherical iron-based feedstocks (i.e., to blends of micrometric and nanometric powders). A few years later, the same research group confirmed the debindability of such HPIM spherical iron-based feedstocks using the thermal wick debinding approach under hydrogen (Choi et al., 2014). Although the last decades have seen the successful development of thermal wick debinding in HPIM using analytical or experimental models, thermal wick debinding of LPIM ceramic-based feedstocks has received very little attention, while that of metal-based feedstocks, containing either spherical or

irregular powders, has been simply ignored. Likewise, to the best of the authors' knowledge, the effect of the pre-sintering temperature on the sintered properties of LPIM metallic parts has not been explored. To start filling this gap, this work aims to demonstrate the capability to debound an irregular iron-based LPIM feedstock using a thermal wick debinding process and investigate the effect of the pre-sintering temperature on the density and pore structure of sintered parts.

5.3 Materials and Methods

The iron powder was provided by Rio Tinto Metal Powders (Sorel-Tracy, QC, Canada). Following the water atomization process, the powder was high-energy milled, screened down using a 325 mesh (-45 μm), and measured using a laser diffraction particle sizing analyzer (Coulter LS13 320 Beckman). The particle size distribution characterized by a D_{10}, D_{50}, and D_{90} of about 1.8, 16.6, and 44.1 μm is reported in Figure 5.1a. The irregular morphology of the dry powder and homogeneity of the powder-binder mixture were observed using a Hitachi 3600 scanning electron microscope (SEM), as illustrated in Figure 5.1b-c.

The feedstock was prepared by blending 55 vol. % of iron powder with a multi-component binder system containing 42 vol. % of paraffin wax (PW) used as the main carrier, 2 vol. % of stearic acid (SA) promoting the surfactant effect, and 1 vol. % of ethylene-vinyl acetate (EVA) used as a thickening agent to avoid the segregation phenomenon. These binder constituents were selected due to their extensive use in LPIM (Leverkoehne et al., 2001; Zaky, Soliman, & Farag, 2009), while the solid loading reached in this study represents a typical value for irregular powders used in LPIM that are mainly reported for ceramic-based feedstocks (Hidalgo et al., 2012; Hnatkova et al., 2019)

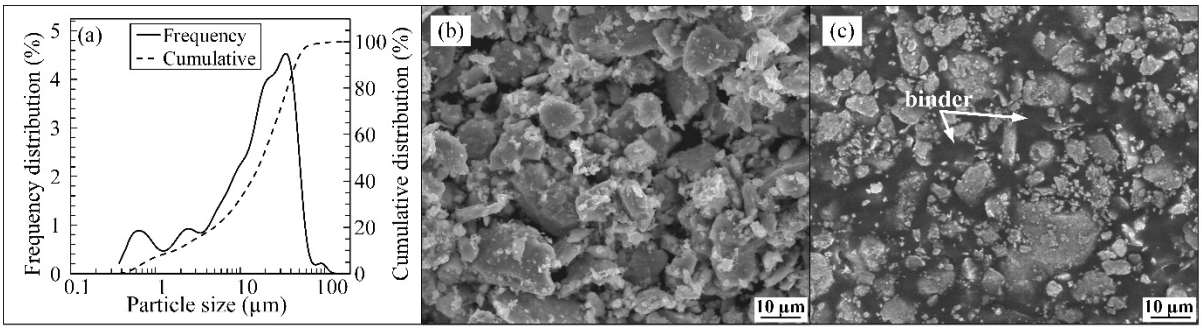

Figure 5.1 (a) Particle size distribution and SEM micrographs of (b) dry powder, and (c) feedstock

The melting point of the feedstock was measured using a Perkin Elmer Pyris 1 differential scanning calorimeter (DSC) according to ASTM D3418 - 03 (ASTM International et al., 2012), and the values for the second heating and cooling cycles are presented. During the test, a specimen of about 10 mg was encapsulated in a standard aluminum pan and heated to temperatures ranging from 20 to 100°C using a heating rate of 10°C/min under a protective atmosphere of dry nitrogen gas flow of 50 ml/min. Based on the DSC measurements, the temperature for the rheological tests and injections was set to about 12°C above the feedstock melting point to ensure its molten state. The feedstock viscosity was measured at 70°C using a rotational rheometer (Anton Paar MCR 302) equipped with a concentric-cylinder geometry (CC-17) and a Peltier temperature-controlled measuring system (C-PTD 200) at shear rates ranging from 0.5 to 1000 s^{-1}. A thermogravimetric analysis (TGA) was performed using a Perkin Elmer Diamond TG/DTA to obtain the decomposition temperatures of the feedstock which were later used to design the debinding cycles. To realize this test, a 10 mg specimen was extracted from the injected part, placed in a standard platinum pan, and heated from 100 to 600°C using a heating rate of 10°C/min under argon gas at a flow rate of 60 ml/min.

Injection molding was performed using the LPIM laboratory injection press specially designed to avoid the segregation that may occur when using a low-viscosity feedstock (Lamarre et al., 2017). During the injections into the rectangular mold illustrated in Figure 5.2a, a constant volumetric flow was maintained at 2.2 cm^3/s, producing a maximum injection pressure of about 0.5 MPa for a mold temperature maintained at 45°C. The injected

parts were then embedded into an inert alpha-phase 99.9% alumina powder bed (Alfa Aesar, Thermo Fisher Scientific, stock # 42572) supported by a stainless-steel boat illustrated in Figure 5.2b. This boat was hermetically sealed within a metallic retort before the air was flushed with argon gas. The retort was placed in a programmable debinding furnace (Nabertherm L3117S) and heated up to different pre-sintering temperatures under an inert atmosphere of argon, using a flow rate of 25 l/min. Three debinding cycles using two distinct stages (debinding and pre-sintering) were used to investigate the effect of pre-sintering temperature on the final sintered properties (debinding cycles are detailed in the section 3.2). A chemical analysis of the as-received powder and debound parts was performed by infrared absorption method, using a LECO TC-500 analyzer for oxygen and a LECO CS-200 analyzer for carbon, while the debound structures were observed using a scanning electron microscope (Hitachi 3600, secondary electron detector).

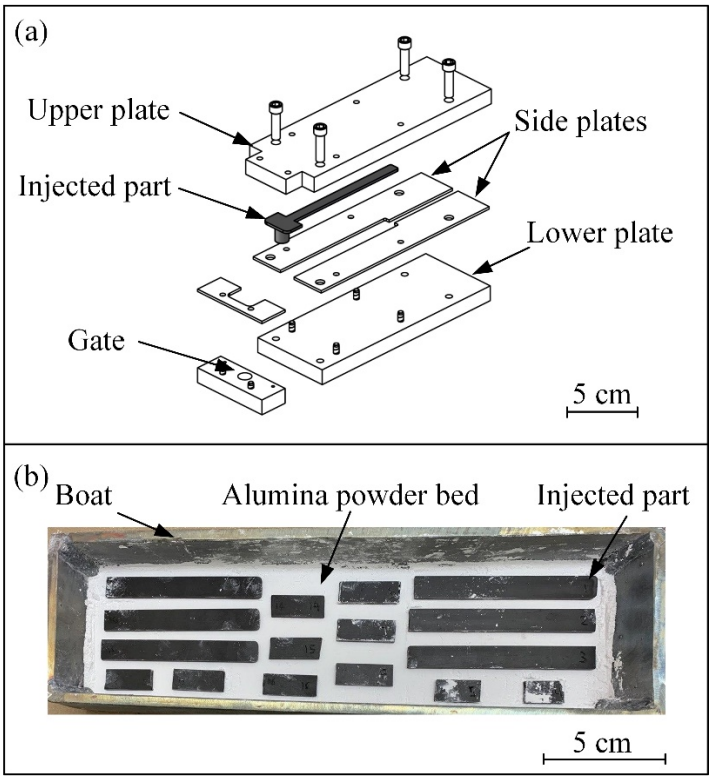

Figure 5.2 (a) Schematic representation of the rectangular mold and (b) typical arrangement of the injected parts settled on an alumina powder bed before debinding (top layer of alumina powder is not shown)

Debound specimens were settled on a dense zirconia plate and sintered in a high-temperature furnace (CM Furnace, model 1516 GSH2FL) using a typical sintering cycle for iron-based MIM parts (You et al., 2012), consisting of heating parts up to a sintering plateau at 1250°C during 90 min under a reactive atmosphere of pure hydrogen (gas flow ~30 l/min). The sintering temperature-time profile is shown in Figure 5.3. The sintered density was measured using the oil-impregnation method based on Archimedes' principle according to MPIF standard 42 (MPIF Standard, 1986). Metallographic analyses were performed on cross-sections of the sintered specimens vacuum-impregnated with epoxy resin, cured at 60°C, mirror-polished, and observed using an optical microscope. A quantitative assessment of average pore size and circularity in sintered specimens was performed using the open-source image processing software ImageJ (Ferreira & Rasband, 2011). For the microstructure observation, the specimens were chemically etched in 2 vol. % Nital solution (2 ml of concentrated nitric acid in 98 ml of ethyl alcohol) and observed using an optical microscope.

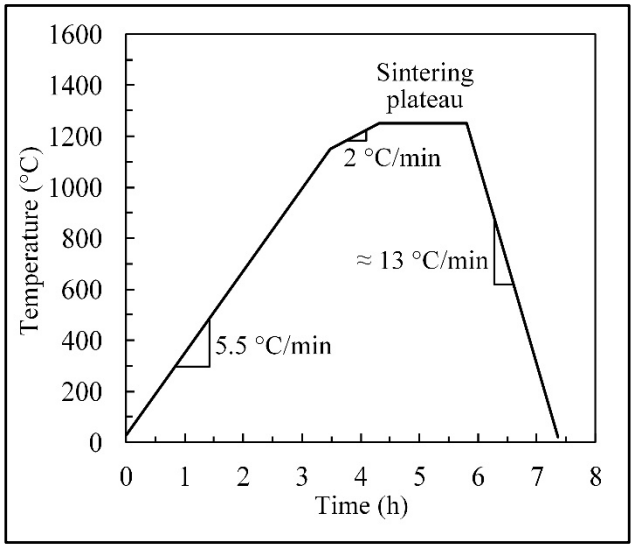

Figure 5.3 Sintering cycle under hydrogen atmosphere

5.4 Results and discussion

5.4.1 Feedstock properties

The DSC curve presented in Figure 5.4a manifests two distinct endothermic peaks corresponding to the melting points of a multi-constituent binder. The feedstock melting point of 57.7°C was determined using the last peak of the curve, as indicated by the black arrow in Figure 5.4a. The feedstock rheological profile measured at 70°C (Figure 5.4b) demonstrated that at this temperature, a range of typical shear strain rates experienced by a powder-binder mixture during the injection (10-100 s^{-1}) corresponds to a feedstock viscosity ranging from 1.5 to 3 Pa·s, which is below 20 Pa·s as recommended for the LPIM processing (Sardarian et al., 2017). This temperature was therefore selected as the feedstock temperature for injections.

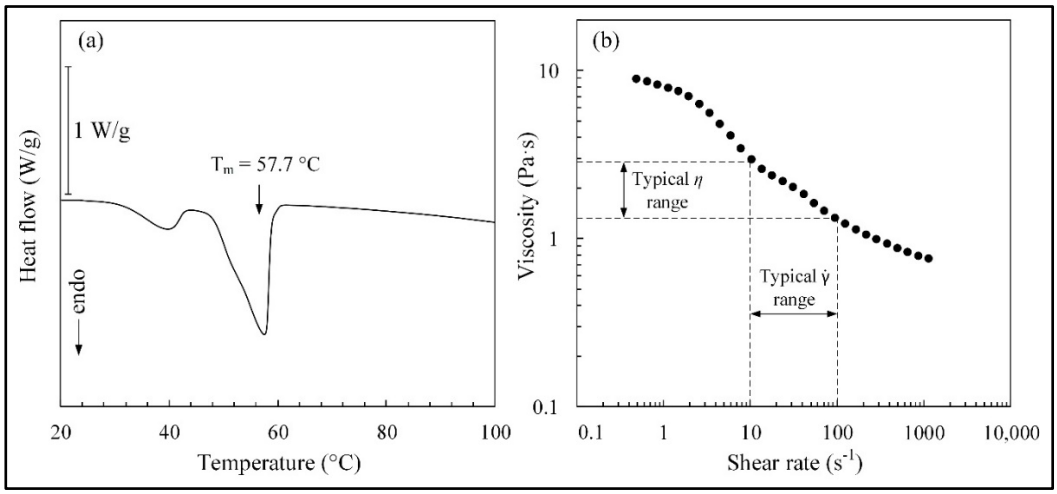

Figure 5.4 (a) DSC profile and (b) viscosity profile of feedstock at 70°C

5.4.2 Debinding

Selection of debinding and pre-sintering temperatures

Figure 5.5a presents the TGA profiles obtained for each binder constituent and the feedstock. The decomposition of individual binders SA, PW, and EVA starts at 150, 160, and 280°C, and

ends at 380, 470, and 480°C, respectively. The EVA decomposition curve exhibits two steps (the first ranging from 280 - 370°C and the second, from 400 - 480°C) corresponding to the thermal degradation of acetic acid and polyethylene-co-acetylene, respectively (Atre, Enneti, Park, & German, 2008). The TGA curves confirm that these three binder constituents are completely decomposed at 480°C. Although the binder is formulated from three constituents, the feedstock's TGA profile exhibits one single but broad decomposition step. This change in the thermal decomposition kinetics between single and multiple binders can be explained by the solubility of the EVA and SA in PW, which has been reported in previous work (Demers et al., 2015). The change in weight fraction corresponds to the initial (TD1) and final (TD2) temperatures of binder burnout at 250 and 380°C, respectively. The TGA profile obtained for the feedstock shows a remaining weight fraction of around 90 wt. %, corresponding to the relative weight of the powder initially contained in the mixture (i.e., a solid loading equivalent of 55 vol. %).

The values obtained from the TGA and DSC profiles were used to define the debinding and pre-sintering temperatures shown in Figure 5.5b. This heat treatment was designed to extract the binder from the injected parts and increase the brown strength (i.e., initiate particle bonding) required for handling and transfer the samples to the sintering treatment. The temperature for the debinding plateau (i.e., the binder removal phase reported as segment #1 in Figure 5.5b) was set at 250°C, i.e., between T_m and T_{D1}, to guarantee the molten state of the binder while avoiding its thermal decomposition. During segment #2, the liquid binder, which was mainly absorbed by the wicking media, was burned out during the temperature ramp-up (over 6 to 12 hours, according to the pre-sintering temperature), starting above T_{D1} and exceeding T_{D2}. In this work, three pre-sintering temperatures with a dwelling time of two hours at 600, 700, and 850°C were used to study the impact of this process parameter on the final sintered density, pore size, and structure (reported as segment #3 in Figure 5.5b). Preliminary debinding tests confirmed that a pre-sintering temperature below 600°C produced a bonding too weak to be handled, i.e., the brown parts were still in a near-loose powder state. In another exploratory trial, a pre-sintering temperature above 850°C induced well-developed neck bonding similar to a fully sintered structure but which did exhibit distortions probably due to

the constrained state inherent to samples embedment into the alumina powder bed. Following the pre-sintering plateau, the specimens were slowly cooled down at approximately 1.6°C/min maintaining an argon protective atmosphere until room temperature was reached (segment #4 in Figure 5.5b). The heating and cooling rates were kept low to create a gradual binder wicking and to minimize the temperature gradients through the green parts, which could cause distortions, cracking, blistering, or other undesirable defects (Thomas-Vielma et al., 2008). Note that the impact of the cooling-heating rates on the quality of parts should be studied further in future work to decrease the total cycle time.

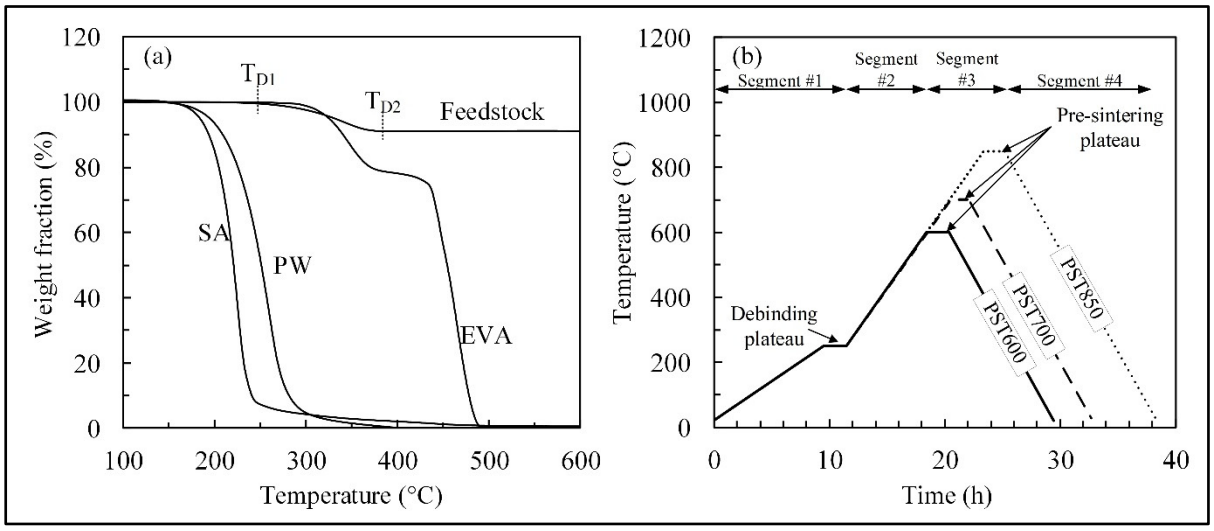

Figure 5.5 (a) TGA profiles of binder constituents (SA: stearic acid; PW: paraffin wax; EVA: ethylene vinyl acetate) and feedstock, and (b) thermal wick debinding cycles performed at different pre-sintering temperatures varying from 600 to 850°C under argon atmosphere

Debound part characterization

The carbon and oxygen contents of the as-received powder and debound parts are compared in Figure 5.6 for different pre-sintering temperatures. As expected, the initial carbon and oxygen levels of the as-received powder are high due to an intrinsic affinity of water-atomized iron powders to oxygen which forms stable iron oxides on particle surfaces (Marucci & Corporation, 2018). After the debinding process, the amount of carbon decreased by a factor 2, while the amount of oxygen decreased by approximately 10 times. Furthermore, a slight

decrease in the carbon and oxygen contents of brown parts was also seen as the pre-sintering temperature increased. The significant decrease in oxygen content can be explained by this element reaction on the surface of the powder, with the carbon alloyed inside and the binder found between the particles. These results show that to design a proper debinding treatment for the MIM iron parts, optimization of the pre-sintering temperature is critical, since shrinkage, structure, and mechanical properties are strongly affected by carbon content (Da Silveira, Wendhausen, & Klein, 2008).

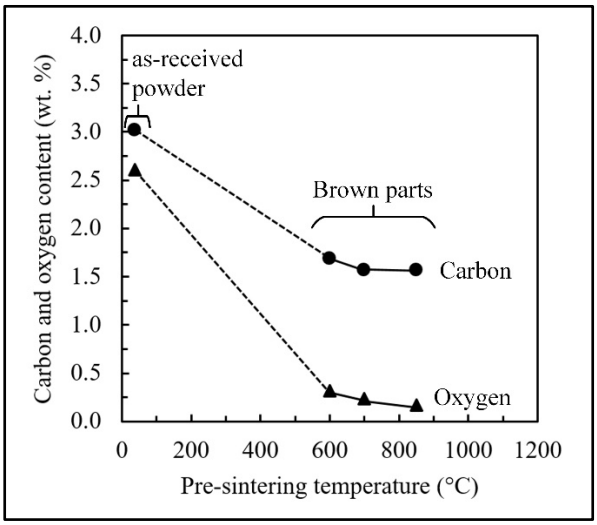

Figure 5.6 Evolution of the carbon and oxygen contents as functions of the pre-sintering temperature

Debound specimens pre-sintered at different temperatures were broken to evaluate the bonding networks as shown in Figure 5.7. After debinding, the center of all the debound parts exhibits a high number of open channels regardless of the pre-sintering temperature used during the debinding cycle (Figure 5.7a-c). An increase in the pre-sintering temperature from 600 to 850°C appears to decrease the amount of fine loose powders which seems to bond on coarse particles. Since these fine particles play an important role in the sintering activation, high pre-sintering temperatures may negatively affect the sintering driving force and, therefore, the final part density. Interestingly, large particles in the center of the debound network do not exhibit

clear and well-defined neck bonding but, rather, a network similar to loose powder particles interlocked together.

Looking at the edge of the debound specimens, the SEM observations shown in Figure 5.7d-f confirm the presence of three distinct zones. Zone #1 is similar to the one observed in the center of the specimens, where no apparent bonding is found. Zone #2 is a sub-surface region where some bonding can be observed under all debinding conditions. Although these two zones are visible regardless of the pre-sintering temperature, a third zone exhibiting a dense layer which can be observed in Figure 5.7e-f was only acknowledged in the specimens debound at high temperatures (i.e., pre-sintered at 700 and 850°C). An explanation for this phenomenon is that an increase in the pre-sintering temperature provides the thermal activation energy sufficient to sinter the surface of the parts. However, some research groups have reported a similar surface phenomenon during the thermal wick debinding of different ceramic-based feedstocks formulated from paraffin wax binders (Da Silveira et al., 2008; Medvedovski & Peltsman, 2012). Zorzi et al. (J. E. Zorzi, Perottoni, & Da Jornada, 2002) and Gorjan et al. (Gorjan, Dakskobler, & Kosmač, 2012) proposed another explanation in which this non-volatile layer was formed during a thermal debinding above 250°C due to an intricate chemical reaction taking place between paraffin wax and alumina powder at the interface of the part and the wicking medium, transforming the hydrocarbon binder into a dense layer. Considering the use of an inert protective atmosphere in our work, this second hypothesis explaining the formation of this dense layer could be linked to the quantity of oxygen and impurities adsorbed, usually in the form of an oxide layer on the particles' surface, which could intensify the formation of such an insoluble layer. Although the study of this phenomenon is beyond the scope of this work, it is interesting to note that the thickness of this dense layer seems to increase with the pre-sintering temperature. Therefore, the strength observed after debinding at different pre-sintering temperatures for this irregular powder seems to be explained by the powder interlocking combined with the occurrence of solid-state bonds when present on the specimen surface.

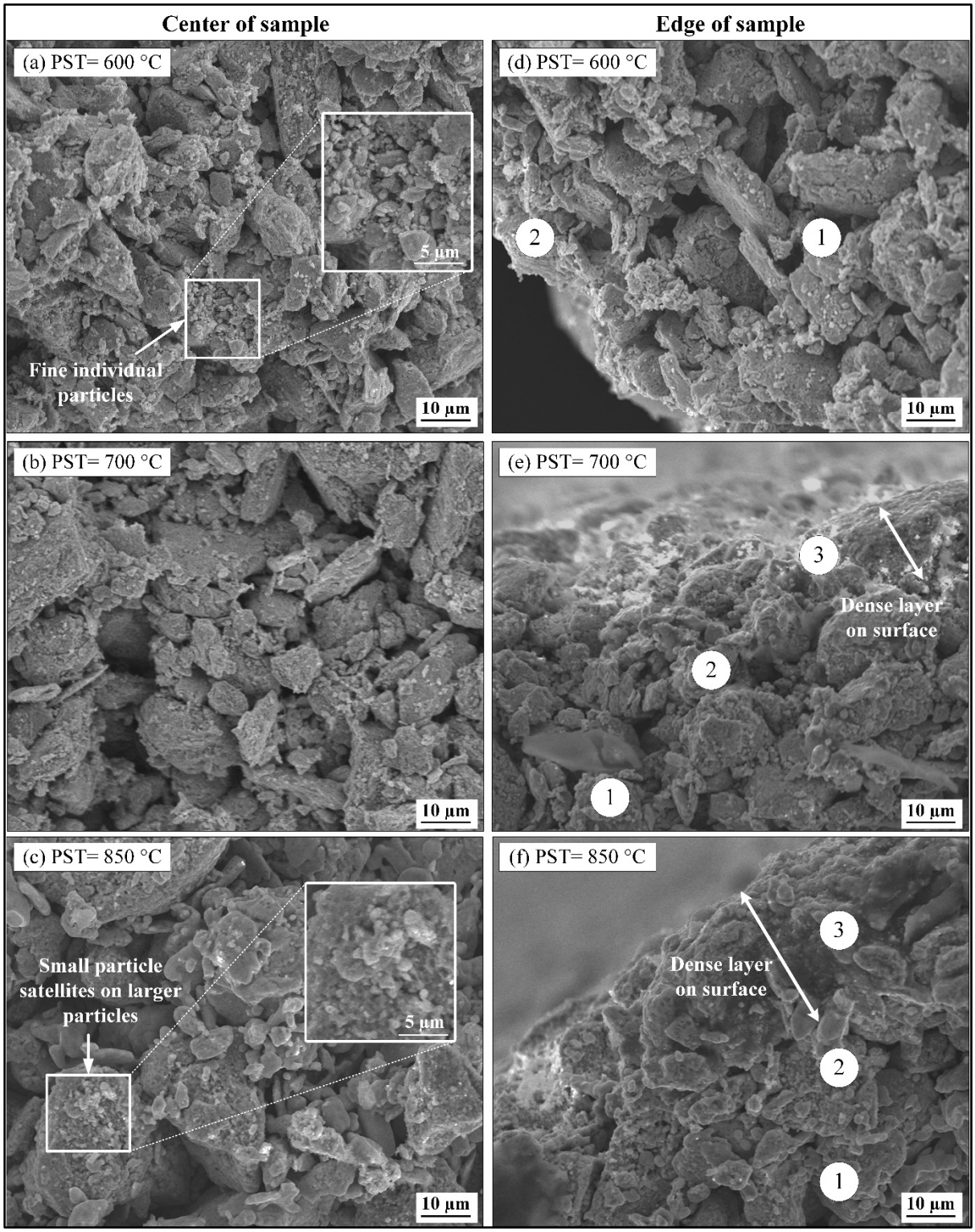

Figure 5.7 SEM observations of the debound specimens (a-c) at the center and (d-f) at the edge of the specimens

5.4.3 Sintered properties

As observed in Figure 5.8a, the debinding stage produces no significant shrinkage as compared to the injected part, since debinding treatment produced no real bonding. After sintering, a linear shrinkage of about 12% was measured. The sintered density of the specimens debound at different pre-sintering temperatures is presented in Figure 5.8b. Globally, the highest final sintered density about 80% of the theoretical value was achieved for the parts debound-pre-sintered at 600°C. As the pre-sintering temperature increases from 600 to 850°C, the sintered density decreases from 6.2 to 5.1 g/cm^3, which is in line with the metallographic analysis presented in Figure 5.9 where the occurrence and size of interconnected pores increase as the pre-sintering temperature increases. In this respect, the smallest volume fraction of pores was obtained with the specimen debound at 600°C, to a smaller extent, at 700°C. The well-distributed isolated pores seen in Figure 9a-b confirm that these low pre-sintering temperatures resulted in a better sinterability that could be explained by the presence of fine particles observed within the debound network of Figure 5.7a-b, combined with the mitigation of undesirable chemical reactions such as contamination, interstitial elements, or surface oxidation.

On the other hand, the optical micrograph of the specimen debound at 850°C (Figure 5.9c) exhibits the highest degree of interconnected pores along with several inter-particle joints. From the metallographic images of sintered microstructures presented in Figure 9d-f, it was observed that regardless of the debinding-pre-sintering temperature (PST), these microstructures manifest a bimodal grain size distribution consisting of small grains with an average size of ~ 6 µm indicated by white arrows in Figure 5.9d-f and large grains with an average size of ~ 30 µm, indicated by red arrows in Figure 5.9d-f. However, for PST of 700°C and 850°C, small grains appear to be located mostly at the pore interfaces on the periphery of the densified clusters, whereas for PST of 600°C, small grains are well-distributed throughout the densified material. The specific small grain distributions observed after high-temperature PST could be due to satellites sintered on large particles after the debinding process, apparently not contributing to the sintering driving force required for further densifying the part.

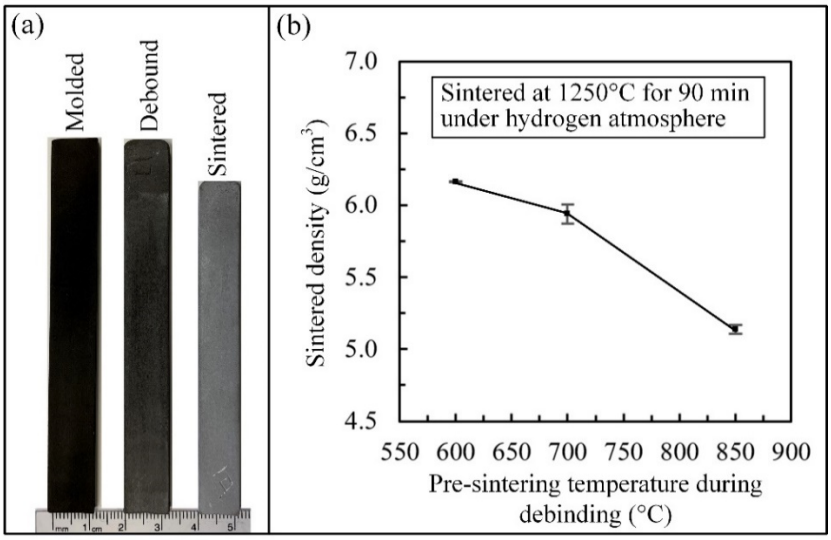

Figure 5.8 (a) Dimensional comparison of injected, debound-pre-sintered at 600°C, and sintered specimens, (b) sintered densities of specimens debound using different pre-sintering temperatures

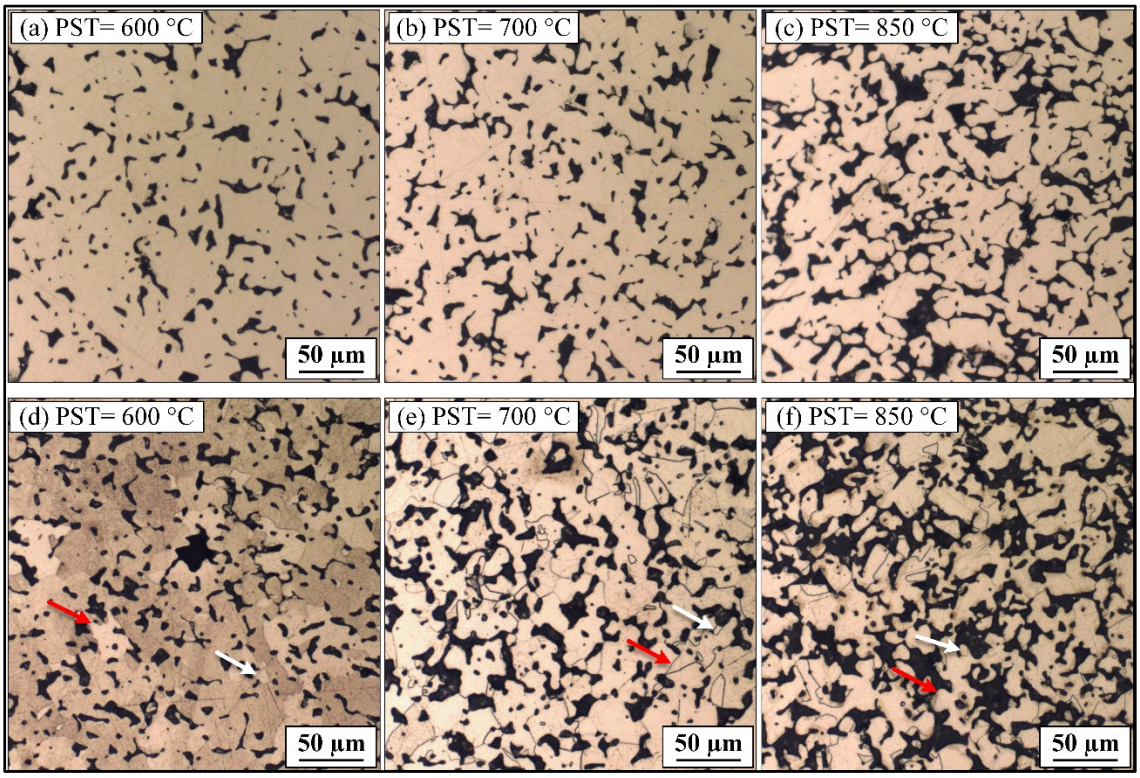

Figure 5.9 Optical micrographs of (a-c) as-polished, (d-f) etched specimens sintered at 1250°C under hydrogen atmosphere following different pre-sintering temperatures

Figure 5.10 illustrates the evolution of an average pore size and circularity as functions of the pre-sintering temperature. It could be observed that the higher the pre-sintering temperature, the larger the pore size (an increase in the average size from 9 to 14 μm) and the lower the pore circularity (a decrease in average circularity from 67 to 59 %). Such kind of increase in pore size and decrease in pore circularity produce decrease in mechanical properties of MIM parts. Moreover, since fine particles observed during debinding-pre-sintering at 600°C can be considered as the major sintering driving force (presented in Figure 5.7a-b), it can be concluded that the pre-sintering temperature must be kept as low as possible to prevent their annihilation, while minimizing undesirable chemical reactions during debinding. In this respect, the sintering process (heating ramp, oxide reduction temperature, sintering temperature, dwell time, etc.) must be optimized in future work to confirm whether the final density can be improved.

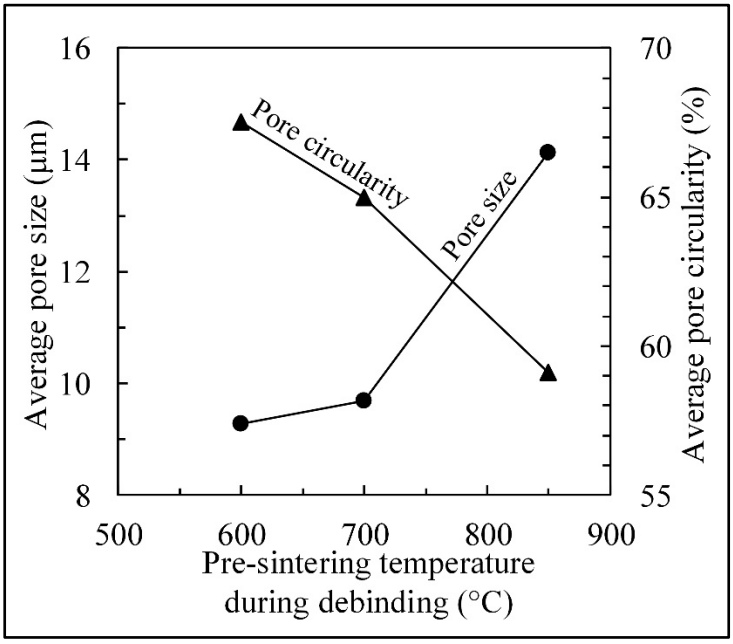

Figure 5.10 Average pore size and circularity as functions of pre-sintering temperature

5.5 Conclusions

A low-pressure powder injection molding (LPIM) approach was used to inject an irregular iron-based feedstock, which was finally debound and sintered. A low-viscosity feedstock was formulated from one irregular iron-based powder (D50 = 16.6 μm) and one wax-based binder system (paraffin wax, stearic acid, and ethylene-vinyl acetate) at a solid loading of 55 vol. % and injected into a rectangular mold cavity. The green parts were thermally wick-debound using three different pre-sintering temperatures (600, 700, and 850°C) and sintered using the same profile at 1250°C under a hydrogen atmosphere for 90 min. The conclusions are summarized as follows:

- The low viscosity (< 3 Pa·s at 10 s^{-1}) and low melting point (~ 58°C) confirm that a powder-binder mixture formulated from irregular iron powder at a solid loading of 55 vol. % is suitable for the LPIM process.
- The debinding process decreased the amount of oxygen by 10 times and the amount of carbon by factor 2 as compared to the as-received powder. Furthermore, a slight decrease in carbon and oxygen content was observed as the pre-sintering temperature increased.
- An increase in pre-sintering temperature from 600 to 850°C decreases the occurrence of fine loose powder distributed within the debound network and promotes the formation of bonding at the surface (dense layer) and the sub-surface (particles bonding) regions. The decrease in sintered density from 6.2 to 5.1 g/cm^3, along with higher degree of interconnected pores observed with an increase in the pre-sintering temperature confirms that this debinding parameter is important and must be kept as low as possible during thermal wick debinding. In this respect, thermal wick debinding using a low pre-sintering temperature produced no clear bonding on this irregular iron powder (i.e., a network similar to loose powder interlocked together), leading to no significant shrinkage, as compared to the as-injected part.
- To the best of the authors' knowledge, this study represents for the first time the capability to debound metallic-based LPIM feedstock using a thermal wick debinding approach that has been presented.

5.6 Acknowledgments

The financial support of Natural Sciences and Engineering Research Council of Canada (NSERC) is gratefully acknowledged.

CHAPTER 6

INFLUENCE OF POWDER SIZE ON THE MOLDABILITY AND SINTERED PROPERTIES OF IRREGULAR IRON-BASED FEEDSTOCK USED IN LOW-PRESSURE POWDER INJECTION MOLDING

A. A. Tafti [a], V. Demers [b], G. Vachon [c], V. Brailovski [b]

[a, b] Department of Mechanical Engineering, École de Technologie Supérieure, 1100 Notre-Dame West, Montréal, Quebec, Canada, H3C 1K3
[c] Research and Development, Rio Tinto Metal Powders, 1625 route Marie-Victorin, Sorel-Tracy, Quebec, Canada, QC J3R 4R4

Paper submitted to *Powder technology,* December 2022

6.1 Abstract

Initially used for shaping irregular ceramic powders, manufacturing metallic parts via low-pressure powder injection molding (LPIM) from irregular powders has received very little attention. This study investigates the processability of irregular powders for fabricating high-density and low-cost metallic parts using the LPIM process. Three irregular iron-based powder lots were mixed with a low-viscosity binder, injected, debound, and sintered to evaluate their molding and sintering performances via viscosity measurements, real-scale injections, metallographic analysis, and tensile tests. The results revealed that feedstocks formulated from fine and coarse powders exhibit good moldability, predicted by their moldability indexes and validated by spiral flow distances. Furthermore, the feedstock formulated with the finer powder (i.e., 1250 mesh providing a powder particle size < 10 μm) produced a homogeneous microstructure along with a low content of oxygen impurities, leading to the highest sintered relative density of ~90%, an ultimate tensile strength of ~225 MPa, and an elongation at break of ~24%. These results confirm that the cost-effective irregular iron powders present a promising alternative to fabricating metallic parts via low-pressure powder injection molding

compared to their relatively high-cost spherical powder counterparts (i.e., carbonyl iron powder).

Keywords: Low-pressure powder injection molding (LPIM), Iron powders, Irregular particles, Feedstock, Melt viscosity, Sintering, Mechanical properties

6.2 Introduction

For more than four decades, low-pressure powder injection molding (LPIM) has represented a cost-effective powder manufacturing (PM) technique for producing near net-shape ceramic components (Mangels & Williams, 1983; Mutsuddy & Ford, 1995; Ritzhaupt-Kleissl, 2009; Xiao et al., 2019). During the last twenty years, this manufacturing approach has been extended to the fabrication of small intricate metallic parts from titanium (Ghanmi & Demers, 2021), tool steel (Liberati et al., 2006), superalloys (Julien & Després, 2006), or stainless steel (Aslam, Ahmad, Sri, et al., 2016). Although this PM technology offers interesting cost reduction advantages related to a decrease in the size of injection machines and mold shells (Gonçalves, 2001; Medvedovski & Peltsman, 2012), current understanding of the fabrication of metallic components via LPIM remains limited to only a few proofs of concept. The LPIM process is a sub-category of the well-known powder injection molding (PIM) technology, where a low viscosity (generally < 20 Pa·s) feedstock is injected using pressure 50 to 200 times lower than that required in conventional PIM (ranging typically from 50 to 700 kPa). In the absence of backbone polymers, the injected parts are debound using a solvent-free single-step thermal wick-debinding process (Gorjan, 2012; Gorjan et al., 2010). Similar to conventional PIM, the debound parts are finally sintered at high temperature under vacuum, protective, or reactive atmospheres to develop a final microstructure producing mechanical properties equivalent or superior to those obtained by press-and-sinter PM or casting (Johnson & Heaney, 2006; Ma et al., 2015, 2014). Although the binder system defines the mixing, injection, and debinding routes in the PIM process, the final properties of metallic parts depend on the powder's sinterability, which depends specifically on its characteristics and surface conditions. As demonstrated by German and Bose (German & Bose, 1997), the discrete particle attributes (e.g., morphology, size, particle size distribution, and surface state), as well as the bulk

properties (e.g., compressibility, cohesion, and packing density), are parameters governing the fundamental aspects of a PIM process, such as the critical solid loading, feedstock moldability, and powder sinterability.

Feedstock moldability is often quantified using Weir's experimental model, which combines different rheological parameters in one molding index (Weir, 1963). To assess the moldability index of ceramic- (Agote et al., 2001; Lenk & Krivoshchepov, 2004; Liu, 1999), composite- (Khakbiz et al., 2005), and metallic-based (Huang & Hsu, 2009) feedstocks, the viscosity at a shear strain rate that corresponds to the molding step, the shear sensitivity index, and the flow activation energy must be extracted from the viscosity profiles obtained at different temperatures. Using this methodology, Claudel et al. (Claudel et al., 2017) studied the effect of particle size on the moldability of four different Inconel powders (D_{50} = 6 – 66 μm). They demonstrated that a decrease in the average particle size increases the surface contact area, promoting interparticle friction and affecting the feedstock moldability, mixing time, and the energy required to homogenize the feedstock. Using a similar approach, Hausnerova et al. (Hausnerova et al., 2017) studied the effect of particle size and shape on the molding properties of eight different spherical and irregular stainless steel powders (D_{50} = 3 – 20 μm). Interestingly, they concluded that the common belief regarding the higher flowability and critical solid loading of gas-atomized (GA) powders as compared to their water-atomized (WA) equivalents is not always true and is mostly applicable to coarser powders (D_{50} > 11 μm) because of their significantly lower sphericity. They also demonstrated that particle size is the dominant factor driving the moldability of fine powders (3 < D_{50} < 8 μm), whereas a slightly higher solid loading and better performance (i.e., lower mixing torque) were obtained for irregular WA powders as compared to GA powders. Furthermore, using the moldability concept, Sotomayor et al. (Sotomayor, Várez, & Levenfeld, 2010) specifically investigated the evolution of the rheological parameters and critical solid loading of five different feedstocks prepared from one fine (D_{50} = 5 μm) and one coarse (D_{50} = 12 μm) GA stainless steel powder and their mixtures (i.e., 25/75, 50/50, and 75/25 ratios, respectively). They demonstrated that adding fine powders increases the mixing time and viscosity and decreases the critical solid loading and that for high solid loading feedstocks, viscosity variations are not driven by the

particle shape but, essentially, by the particle size (i.e., regardless of the particle shape, viscosity increases as particle size decreases). Dihoru et al. (Dihoru, Smith, & German, 2000) extensively studied the moldability (i.e., feedstock homogeneity, stability, and qualitative evaluation of powder/binder separation) of seven feedstocks using different batches of GA and WA stainless steel powders or their mixtures. They demonstrated that bimodal feedstocks exhibited better stability over different shear rates (i.e., lower occurrence of powder/binder separation) than those prepared from coarser unimodal irregular powders. Using a neural network approach, they also proposed a model predicting the feedstock viscosity and optimal solid loading based on powder characteristics, such as the average diameter, the shape and size distributions, and the weight fractions of different powders in powder mixtures.

In addition to the presence of a rich body of moldability analyses, the influence of the particle shape and size on the final sintered microstructures is also significantly addressed in the literature. For instance, Dehghan-Manshadi et al. (Dehghan-Manshadi et al., 2018) investigated the PIM processability of a coarse ($D_{50} \approx 45$ μm) irregular hydride-dehydride titanium powder. They confirmed that despite the lower flowability, packing density, and critical solid loading of such a powder, as compared to its more spherical equivalent, it allowed to obtain decent sintered properties, including a relative density of 96.5%, an ultimate tensile strength of 395 MPa, and an elongation at break of 12.5%. Along with the particle shape and size, the particle size distribution is another important powder characteristic affecting PIM feedstock sinterability. Using three spherical stainless steel powders exhibiting similar particle sizes, Mukund et al. (Mukund & Hausnerova, 2020) highlighted that an increase in the volume fraction of coarse particles produces a decrease in the sintered density and hardness due to an increase in the occurrence of irregular particles. The same research team confirmed that tailoring the powder size distribution can reduce the cost of raw powders without compromising their sintered properties. In (Mukund, Hausnerova, & Shivashankar, 2015), the research group used different PIM grade GA stainless steel powders ($3 < D_{50} < 45$ μm) to demonstrate that a bimodal feedstock formulated from ~6 and ~20 μm powders allows a 10% cost reduction, as compared to similar unimodal powders, without compromising the sintered density of a final product (~7.75 g/cm^3). Similarly, Shu and Hwang (G. J. Shu & Hwang, 2004)

studied the impact of particle size and shape on the powder sinterability by mixing fine spherical carbonyl iron powders (D_{50} = 4 μm) with coarse WA iron powders (D_{50} = 45 μm) in a ratio of 4:6. Using these low-cost powder mixtures, they demonstrated that adding small quantities of α-phase stabilizers (Fe_3P and Mo) inhibits grain growth, thus providing mechanical properties similar to those obtained with more expensive fine spherical powders. It can therefore be stated that even though customizing powder characteristics constitutes a promising approach to maximize the PM molding and sintering performance while saving cost, the selection of the powder particle shape, size, and distributions remains an empirical task where conclusions remain difficult to transfer directly from one powder to another.

Recently, increasing attention has been focused on understanding the impact of powder characteristics on LPIM moldability and sinterability. For example, Trad et al. (Ben Trad, Demers, & Dufresne, 2019) studied the effect of powder shape and size on the molding performance of different LPIM stainless steel powder ($3 < D_{50} < 12$ μm) feedstocks. Using a constant solid loading (60 vol. %), they showed that the molding performance depends on the particle shape and size, with spherical and fine particles being respectively responsible for the lower viscosity and higher stability of the feedstocks. Recently, Moghadam et al. (Moghadam et al., 2021) reported the successful fabrication of LPIM parts from irregular shape titanium-based feedstocks with an acceptable sintered density and hardness, despite a relatively low reported solid loading of 53 vol. %. However, the potential of irregular iron powders as cost-effective LPIM feedstock components has not been sufficiently investigated, notwithstanding that iron powders are one of the main components in pre-alloyed powders, master alloys, and powder mixtures to fabricate ferrous PIM parts (Moon et al., 2021). To the best of the authors' knowledge, only one previous work has studied LPIM moldability of irregular iron-based feedstock, where it was concluded that such a cost-effective powder could be used to fabricate complex shape green parts (Tafti, Demers, Vachon, & Brailovski, 2021). Furthermore, they studied the influence of powder characteristics and LPIM processing conditions on the sintered density using similar irregular iron-based feedstocks (Majdi et al., 2022; Tafti, Demers, Majdi, et al., 2021). However, the impact of powder characteristics and sintering parameters on the mechanical properties of such iron-based components produced by LPIM remains unknown.

Therefore, this work aims to investigate the effect of particle size on LPIM feedstock moldability and the final mechanical performance of parts produced using irregular iron-based powders.

6.3 Experimental procedures

The rheological behavior and moldability of six feedstocks formulated from three powder lots at two solid loadings were studied. Next, feedstocks with the highest solid loadings were used to inject specimens that were then debound and sintered, and the density, microstructure, chemical composition, and mechanical properties of the sintered specimens were finally studied.

6.3.1 Powder characterization

The iron powder used in this work was produced by Rio Tinto Metal Powders (Sorel, QC, Canada) using a three-step workflow comprised of water atomization, high-energy attrition milling, and sieving. To work with the coarse, medium, and fine powders, three different powder lots were identified for the study as -45, -25, and -10 μm (corresponding to a mesh size of 325, 600, and 1250, respectively). Regarding the screening size, powder -45 μm represents a powder lot consisting of particles that have passed through a 45 μm sieve opening. As expected from this fabrication route, the powders observed via scanning electron microscope (Hitachi 3600, SE detector) exhibit an irregular morphology (Figure 6.1a-c).

The particle size distributions (PSD) presented in Figure 6.1d-f were measured using a particle size analyzer (Beckman Coulter LS13 320 XR). Both particle size characteristics extracted from the cumulative PSD and the powder density obtained using a gas pycnometer (Micromeritics AccuPyc II 1340) are reported in Table 6-1. Although the frequency curves generally have a Gaussian distribution, the attrition milling process used to reduce the particle size seems responsible for the bimodal distributions of all three powder lots. Moreover, according to the PSD measurement presented in Figure 6.1e, the -25 μm powder

shows an unexpected third distinct peak in the frequency distribution (also visible on the final plateau of the cumulative distribution). This third peak was discarded from the D_{90} calculations for this powder lot. The results section further discusses this unusual PSD curve.

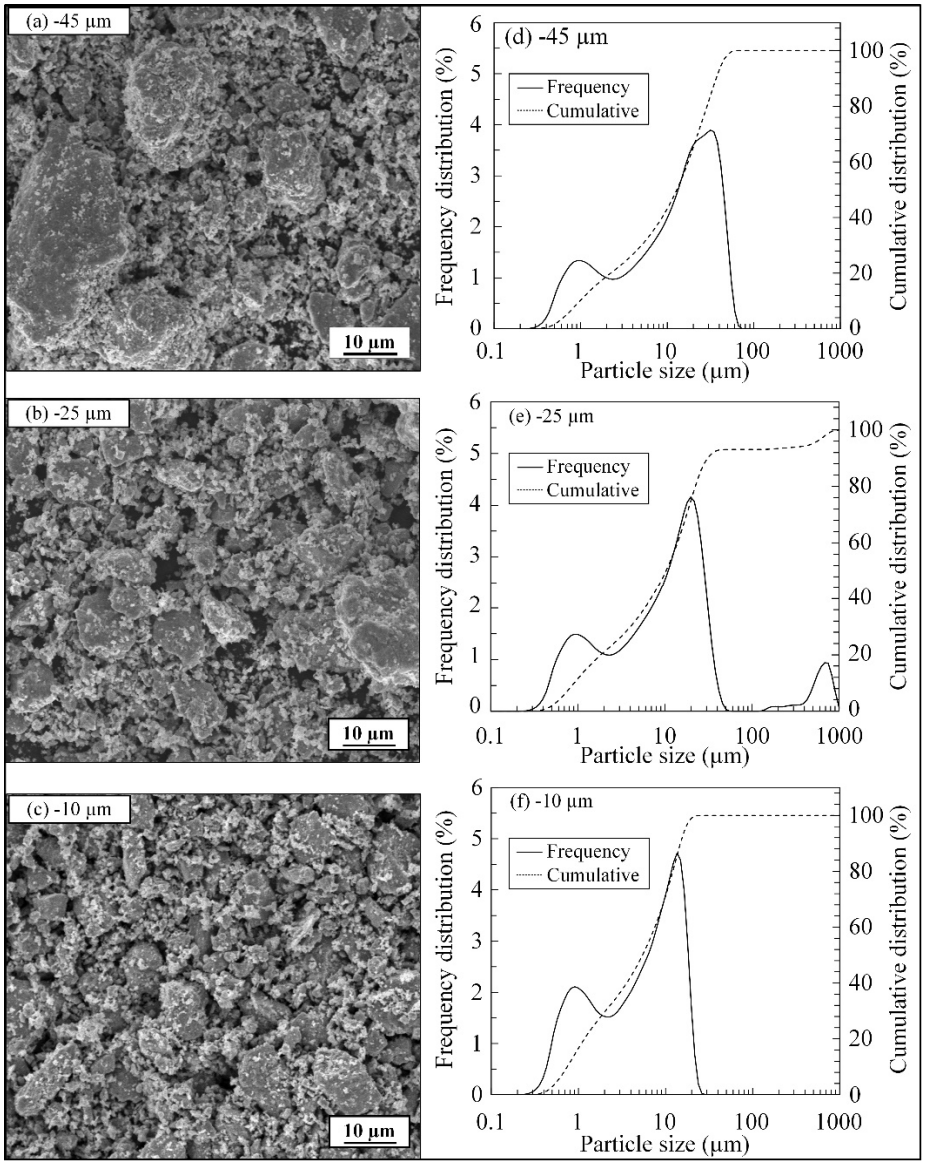

Figure 6.1 SEM micrographs and frequency and cumulative particle size distributions of (a, d) −45 µm, (b, e) −25 µm, (c, f) −10 µm iron-based powder lots

Table 6-1 Physical properties of iron powders.

Powder ID	Particle size (µm)			Span	Distribution slope parameter (S_W)	Pycnometer density (g/cm^3)
	D_{10}	D_{50}	D_{90}	$(D_{90}-D_{10})/D_{50}$		
-45 µm	1.0	13.1	38.6	2.87	1.61	7.4
-25 µm	0.9	10.6	26.0	2.37	1.75	7.1
-10 µm	0.8	5.8	15.6	2.55	1.98	6.9

6.3.2 Feedstock formulation and characterization

A multi-component wax-based binder system formulated from paraffin wax (PW), stearic acid (SA), ethylene-co-vinyl acetate (EVA), and carnauba wax (CW) was mixed with each powder lot. PW was selected as the major binder due to its extensive use in LPIM. SA acts as a surfactant to develop a chemical bridge between the powders and binders, thus improving the powder-binder wettability. EVA improves the green strength and prevents the powder-binder separation during the injection (i.e., during high shear rates injection and zero shear rate idle time). CW facilitates the demolding of injected parts while improving their green strength. The binder properties reported in Table 6-2 were obtained using a differential scanning calorimeter (Perkin Elmer Pyris 1 DSC) and the gas pycnometer described above. Specifically developed for irregular iron-based powders in a previous study (Tafti, Demers, Vachon, et al., 2021), the binder composition (vol. %) corresponds to 1% of SA, 2% of EVA, 2% of CW, and 36-38% of PW, the latter value depends on the solid loadings used for each feedstock.

Table 6-2 Characteristics of binder constituents

Constituent	Melting point (°C)	Density (g/cm^3)	Source
Paraffin wax (PW)	54.0	0.9	Sigma-Aldrich
Stearic acid (SA)	75.0	0.9	Sigma-Aldrich
Ethylene-co-vinyl acetate (EVA)	99.0	1.0	DuPont Elvax, MFI=52 g/10 min, VA comonomer content=40%
Carnauba wax (CW)	84.5	1.0	Sigma-Aldrich

Two approaches were used to evaluate the molding behavior of the feedstocks prepared from the powder lots (Table 6-3). During stage 1, to assess the impact of the particle size on the feedstock viscosity, a common solid loading for all the powder lots was set to 57 vol. %. This

value corresponds to the maximum workable solid loading of the finest powder used in this study (i.e., -10 µm). During stage 2, to investigate the overall performance of each powder lot during the LPIM process (i.e., primarily the moldability and sinterability), the maximum solid loading of each powder lot was used in the feedstock formulation. This powder loading varied from 57 to 59 vol. %, with a higher solid loading observed as the powder got coarser (Table 6-3). An example of maximum solid loading quantification using pycnometer density measurement is demonstrated in (Majdi et al., 2022).

Table 6-3 Feedstocks for two phases of moldability analysis

phases	Feedstock ID	Maximum solid loading (vol. %)	Feedstock identification
Phase 1	-45 µm	57	38PW-1SA-2EVA-2CW
	-25 µm	57	38PW-1SA-2EVA-2CW
	-10 µm	57	38PW-1SA-2EVA-2CW
Phase 2	-45 µm	59	36PW-1SA-2EVA-2CW
	-25 µm	58	37PW-1SA-2EVA-2CW
	-10 µm	57	38PW-1SA-2EVA-2CW

The feedstocks' melt viscosity was quantified using a rotational rheometer (Anton Paar MCR 302 equipped with a C-PTD200 cell and a Peltier temperature controller) at shear rates ranging from 0.5 to 1000 s^{-1} and temperatures of 80, 90, and 100°C. The experimental Weir model (Weir, 1963) described in Equation 6.1 was used to assess the feedstock moldability index (α_{STV}), gathering the melt viscosity (η_{ref}) at a reference shear rate, the flow behavior index (n), and the flow activation energy (E) extracted from the viscosity profiles (where R is the gas constant). Preliminary results obtained on three repetitions (not shown in this study) confirmed negligible viscosity variations of ±0.01 Pa·s, where all the variations outside these limits were considered measurable differences.

$$\alpha_{STV} = \frac{|n-1|}{\eta_{Ref}.{}^{E}/_{R}} \tag{6.1}$$

6.3.3 Injection, debinding, and sintering

A laboratory-scale injection press (as schematized in Figure 6.2a) was used to validate the moldability index and fabricate rectangular sub-products for tensile tests and density

measurements. First, injections in the standard spiral mold illustrated in Figure 6.2b were performed to quantify the injected length by calculating the spiral flow distance (SFD), Equation 6.2.

$$L = \int_0^{c.2\pi} \sqrt{(a + b \cdot \theta)^2 + b^2}\, d\theta \tag{6.2}$$

where a is the starting point of the Archimedean spiral (a = 4.7 mm), b is the spiral increment divided by 2π (b = 1.51 mm), c is the number of turns, and θ is the angle in radians. Second, the mold illustrated in Figure 6.2c was used to produce rectangular specimens (160 × 13 × 3 mm) for metallographic and chemical analyses and tensile tests. All the injections were performed using a constant volumetric flow of 2 cm^3/s, a mold temperature of 45°C, and a feedstock temperature of 90°C according to previous works with the injection system and feedstock melting point measurements using a differential scanning calorimeter (DSC) quantified previously in (Tafti, Demers, Majdi, et al., 2021).

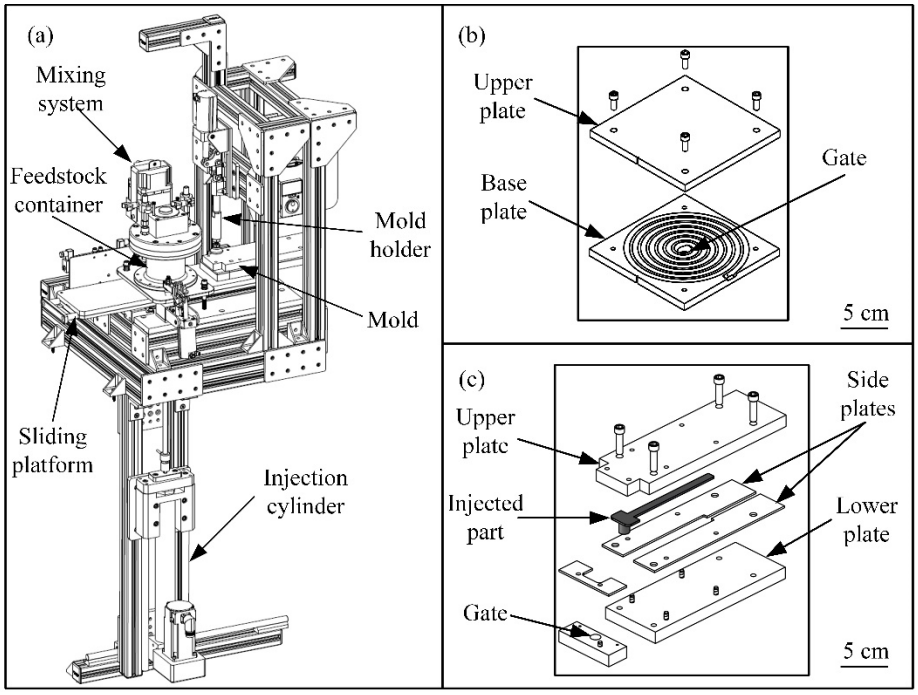

Figure 6.2 Schematic illustrations of the (a) injection press and mold cavities for (b) spiral and (c) rectangular geometries

The rectangular injected specimens were then debound and sintered using the thermal cycles presented in Figure 6.3. The binder was removed following the thermal cycle of Figure 6.3a. Using a thermal wick-debinding approach, the injected parts were placed into a debinding cell, introduced in a Nabertherm debinding furnace (model L3117S, Lilienthal, Germany), and heated under argon gas flow (25 L/min). The debinding cell consists of a stainless steel container supporting an inert alpha-phase 99.9% alumina powder bed (Alfa Aesar, Thermo Fisher Scientific, stock # 42572) sealed into a hermetic metallic retort purged with argon. During the first stage of this heat treatment (dwell time 2 h), alumina used as a wicking medium extracts the melted binder out of the part using capillary forces (segment (i) in Figure 6.3a). To activate thermal pyrolysis, the furnace temperature is increased to the pre-sintering temperature for which alumina acts as a support during the binder burnout and pre-sintering steps (dwell time 2 h) indicated by segment (ii) in Figure 6.3a. After cooling, debound specimens were taken off the alumina bed, air-cleaned, and settled on a dense zirconia plate before being sintered at 1280°C using a high-temperature furnace (CM Furnace, model 1516 GSH2FL, Bloomfield) under a pure hydrogen gas flow (30 L/min) for three sintering times of 30, 90, and 270 min (segment (iii) in Figure 6.3b), and then cooled down.

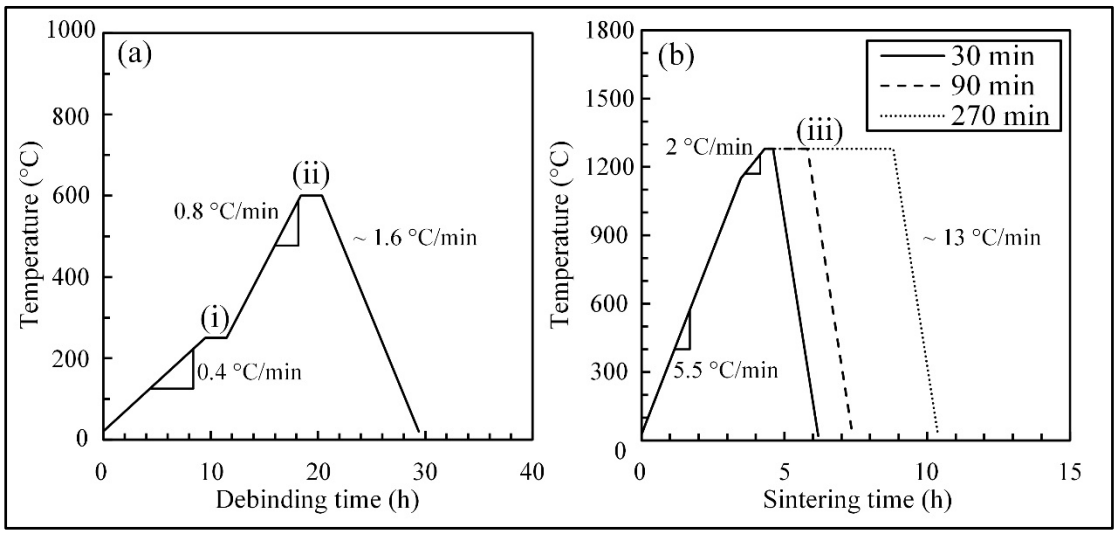

Figure 6.3 Thermal wick-debinding cycle under the protective atmosphere of pure argon and (b) sintering cycles under the reactive atmosphere of pure hydrogen

Figure 6.4a-c presents the injected, debound, and sintered rectangular sub-product parts. The X-ray radiography inspection on all the injected, debound, and sintered specimens using an XT H225 X-ray µ-CT (computed tomography) system (Nikon, MI, USA) with an effective pixel size of 56 µm (i.e., 1 pixel= 56 µm) confirmed the absence of internal defects such as cracks and voids larger than 56 µm. An example of X-ray inspection is presented in Figure 6.4d for one sintered part. The rectangular sintered bars sub-products were machined to obtain flat dog bone tensile specimens (Figure 6.4e) as per the MPIF Standard 10 ("Standard Test Methods for Metal Powders and Powder Metallurgy Products," 2016).

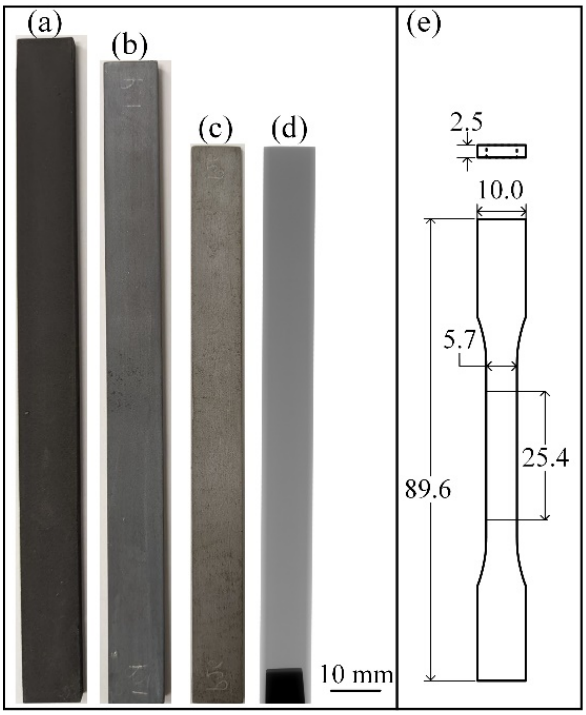

Figure 6.4 (a) Injected, (b) debound, (c) sintered, (d) X-ray radiography specimens, and (e) sketch of the tensile test specimen (dimensions in mm)

Density measurements, metallographic and chemical analyses, and mechanical tests were performed on the sintered specimens. First, the sintered density was measured according to Archimedes' principle using an analytical balance (Sartorius SECURA324-1S readability 0.1 mg) and the oil-impregnation method described in the MPIF Standard 42 ("Standard Test

Methods for Metal Powders and Powder Metallurgy Products," 2016). Next, metallographic analysis of the specimen cross-sections was performed to evaluate the pore size, shape, and distribution. For this purpose, the specimens were mounted in Bakelite, mirror polished, and then observed with an optical microscope (Leica Microsystems Wetzlar GmbH, Wetzlar, Germany) at low magnification (×100). Next, to quantify the pores' morphology (occurrence and equivalent diameters), these unetched microstructures were post-processed using Dragonfly software (Object Research Systems, Montreal, QC, Canada) (Chandra & Vishal, 2021; Moro, Francioso, & Velay-Lizancos, 2021; Scheffer, Méheust, Carvalho, Mauricio, & Paciornik, 2021). Finally, following the thresholding procedure and from the segmented data, the surface area (A) of every pore was evaluated, and Equation 6.3 was used to calculate the equivalent diameter (d_{eq}).

$$d_{eq} = (4A/\pi)^{1/2} \tag{6.3}$$

Next, the metallographic specimens were chemically etched in Nital (2 mL of concentrated nitric acid in 98 mL of ethanol) and observed using the scanning electron microscope described above at a magnification of ×600. Then, the evolution of the oxygen and carbon contents was measured in as-received powders and on debound, pre-sintered, and sintered specimens by infrared absorption using oxygen and carbon analyzers (TC-500 and CS-200 LECO, St. Joseph, MI, USA, respectively). The phase state after debinding was assessed on -25 μm specimen using a PANalytical X-ray diffractometer with Cobalt Kα radiation (scanned angles from 30° to 120°, step size 0.033°, generator voltage 45 kV, and tube current 40 A). A second XRD scan was performed from 30° to 65° 2θ using a smaller step size of 0.008° in order to identify the oxide phases. Finally, the mechanical properties were quantified by tensile tests performed up to fracture at a crosshead speed of 0.15 mm/min using an Alliance RF/200 electromechanical machine (MTS, Eden Prairie, MN, USA) equipped with an extensometer (MTS 634.12e-54) and a 10 kN load cell (p/n 4501030). The tests at each condition (powder and sintering time) were repeated three times for 27 specimens.

6.4 Results

6.4.1 Rheological behavior

Figure 6.5 shows viscosity profiles obtained at 90°C for the three feedstocks produced from the same binder formulation (1SA-2EVA-2CW-38PW) and solid loading (57 vol. %). This test with an identical solid loading was performed to capture the influence of particle size on the feedstock viscosity. At very low shear rates (i.e., $\dot{\gamma} < 2$ s^{-1}, identified as zone 1 in Figure 6.5), the viscosity values remain high due to significant interparticle friction and/or agglomerations when feedstocks are formulated near its critical solid loading (Hausnerová, 2010; Metzner, 1985). In this respect, viscosity values are significantly higher for -10 µm feedstocks due to their smaller particle size, which results in greater interparticle interactions. As the shear rate increases (i.e., $\dot{\gamma} > 2$ s^{-1}), the hydrodynamic interaction between the powder and binder becomes predominant, and the viscosity decreases. This well-known shear thinning effect, designated as zone 2 in Figure 6.5, is due to the reorientation of molecular chains and particles with the flow. Note that the feedstock viscosity decreases by about ten times in this zone. At high shear rates ($\dot{\gamma} > 200$ s^{-1}, identified as zone 3 in Figure 6.5), any further increase in shear rate produces almost no effect on the viscosity. Generally, this viscosity stabilization corresponds to the state where all polymer molecular chains become aligned, and the viscosity profiles tend to become quasi-Newtonian (Zu, Chiou, & Lin, 1996). At typical LPIM shear rates experienced by the feedstock during an injection (i.e., $10 < \dot{\gamma} < 1000$ s^{-1}, between zones 2-3), it is interesting to note that the viscosity values are quite similar, regardless of the particle size. This reflects the fact that for these irregular powders with very wide size distribution, viscosity values at higher shear rate are less affected by the particle size. However, it should be noted that for very high shear rates (> 670 s^{-1}), the -10 µm feedstock exhibits a slight increase in viscosity of ~0.15 Pa·s. As confirmed by Fareh et al. (Fareh et al., 2017), this measurement artifact is often due to powder-binder separation occurring during rheological tests with powders exhibiting high fluidity. This powder separation (also known as segregation phenomenon) produces a powder-rich area at the middle and bottom regions of the rheometer cup resulting in an increase in the viscosity values.

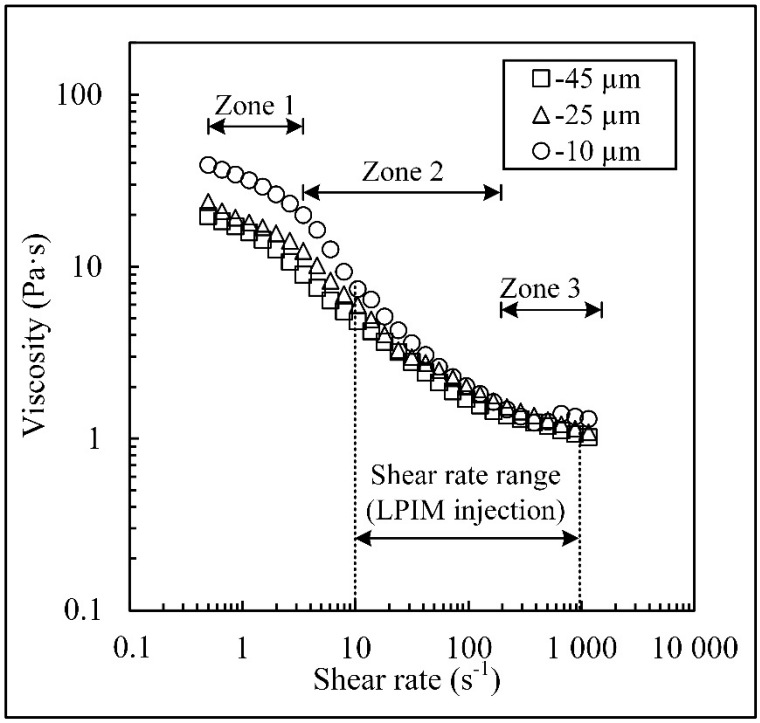

Figure 6.5 Influence of particle size on the feedstock viscosity (all feedstocks formulated with an identical solid loading of 57 vol. % and tested at 90°C)

In this work, the effect of particle size distribution on moldability and sinterability was also studied using solid loadings varying from 57 to 59 vol. % (see Table 6-3). The viscosity profiles presented in Figure 6.8 were obtained at 80, 90, and 100°C to assess their moldability indexes. All the viscosity profiles shown in Figure 6.8a-c exhibit the three zones highlighted above at low, medium, and high shear rates, in addition to the expected decrease in viscosity when the feedstock temperature is increased. Within an effective LPIM shear rate of 10 to 1000 s^{-1}, these three feedstocks exhibit similar rheological behavior for a given temperature, regardless of the powder size and solid loading. However, at high shear rates (> 100 s^{-1}) and high temperatures (90-100°C), the viscosity of the -45 µm feedstock becomes unexpectedly higher than that of

the two other feedstocks. As mentioned above, this measurement artifact reported in Figure 6.6b-c is possibly due to the powder-binder separation.

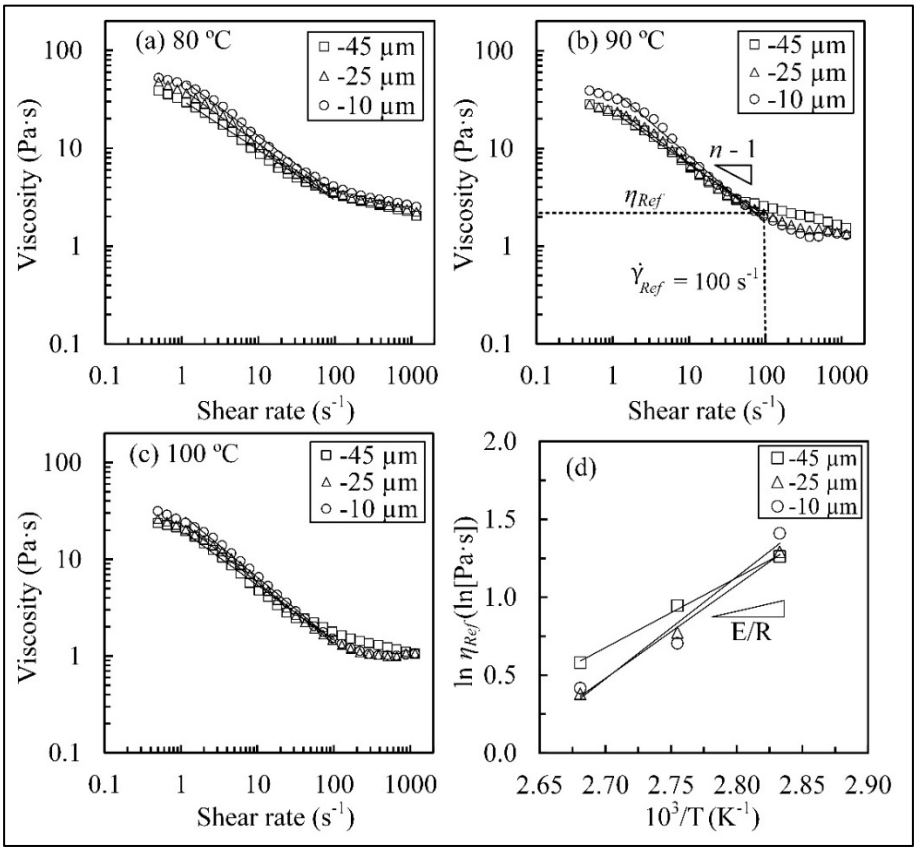

Figure 6.6 (a-c) Feedstock viscosity profiles at 80, 90, and 100°C and (d) influence of temperature on the feedstock viscosity (feedstocks formulated from their maximum solid loadings)

The moldability indexes were then calculated from the viscosity profiles of all the feedstock obtained at 90°C. As illustrated in Figure 6.6b, the shear rate sensitivity indexes *n* and reference viscosities (η_{ref}) were extracted from the slope of a log-log plot of the viscosity profiles and at a reference shear rate of 100 s^{-1}. The reference viscosities were extracted from all other viscosity profiles and plotted in Figure 6.6d in an *ln η* vs. *1/T* graph. The flow activation energy (*E*) was obtained from the slope of these curves and is reported in Table 6-4, along with the *n* and η_{ref} values. These three rheological parameters were finally combined together to calculate the moldability index (α_{stv}) using Equation 6.1. From a rheological perspective, a

feedstock with lower flow index *(n)* and flow activation energy (*E)* values generally exhibits a better filling performance and stability during the injection molding process.

It can be seen in Table 6-4 and Figure 6.6d that the -45 μm feedstock exhibits the highest viscosity, but the lowest shear thinning and temperature sensitivities. For the -10 μm feedstock, however, the trend is the opposite, where we see the lowest viscosity and the highest shear thinning and temperature sensitivities, even if this mixture has 2 vol. % less powder. Moreover, for the -25 μm feedstock, the trend lies somewhere between the other two cases, with a sensitivity to temperature changes (i.e., the *E* value) close to that of the -10 μm feedstock. Since the three rheological parameters used in Weir's model have the same weight in the equation, the results presented in Figure 6.7 confirm that this combination of factors results in an unexpected decrease in the α_{stv} value for the -25 μm feedstock as compared to the other two feedstocks. Therefore, from the moldability analysis, the -10 μm feedstock manifests the best molding potential thanks to its higher feedstock homogeneity and a slightly lower solid loading (57 vol. %).

Table 6-4 Values of the rheological parameters η_{Ref}, n, and E

Feedstock ID	Solids loading (vol. %)	η_{Ref} (Pa·s)	n	E (kJ/mol)
-45 μm	59	2.6	0.46	37.3
-25 μm	58	2.2	0.41	49.8
-10 μm	57	2.0	0.37	54.5

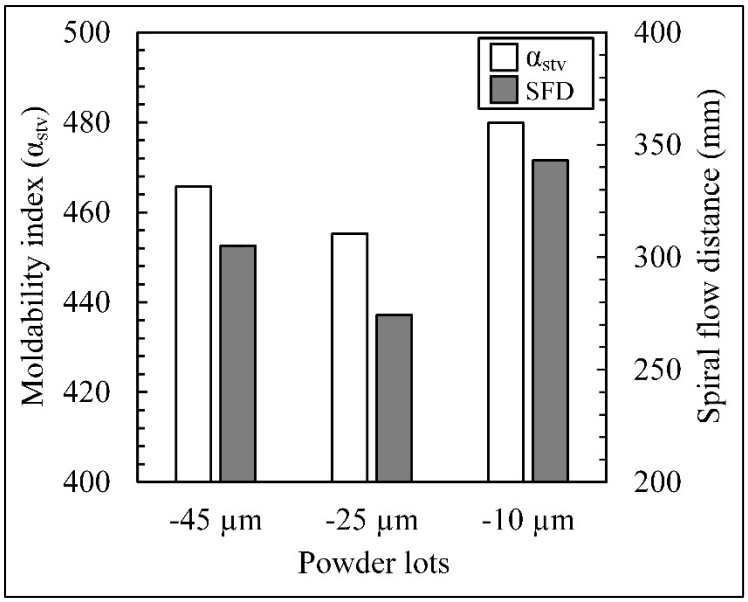

Figure 6.7 Comparison between the moldability index and the spiral flow distance

Ironically, the -25 µm feedstock has the lowest molding capability. As presented earlier for this specific powder lot, the PSD analysis shown in Figure 6.1e reveals a third distinct peak of very coarse particles (~ 700 µm). Considering that all the powder lots were initially sieved to their particle size fractions (i.e., 45, 25, and 10 µm), the presence of particles larger than 100 µm can be discarded. Also, from the size distribution span (i.e., $(D_{90}-D_{10})/D_{50}$), the -25 µm powder lot appears to have a narrower size distribution than the other two powders, which may be due to the relocation of some particle fractions from the PSD curve through agglomerations. To confirm this idea, a sample of the -25 µm powder lot was first sieved using a mesh opening of 75 µm to break down the agglomerates; it was then observed using SEM, and its PSD was obtained again using a particle size analyzer. At low magnification (×25), the SEM image reported in Figure 6.8a confirms an important agglomeration of -25 µm powder after sieving as compared to the -45 and -10 µm powders shown in Figure 6.8b-c. Also, a new PSD curve (dashed line in Figure 6.8d) showed a reoccurrence of the third peak on the right-hand side of Figure 6.1e, but with a lower intensity. Based on these observations and the moldability analysis, it can be concluded that the -25 µm powder exhibits a high propensity for agglomeration, which is impossible to break down by mixing, contributing to a relatively lower molding capability of this powder lot.

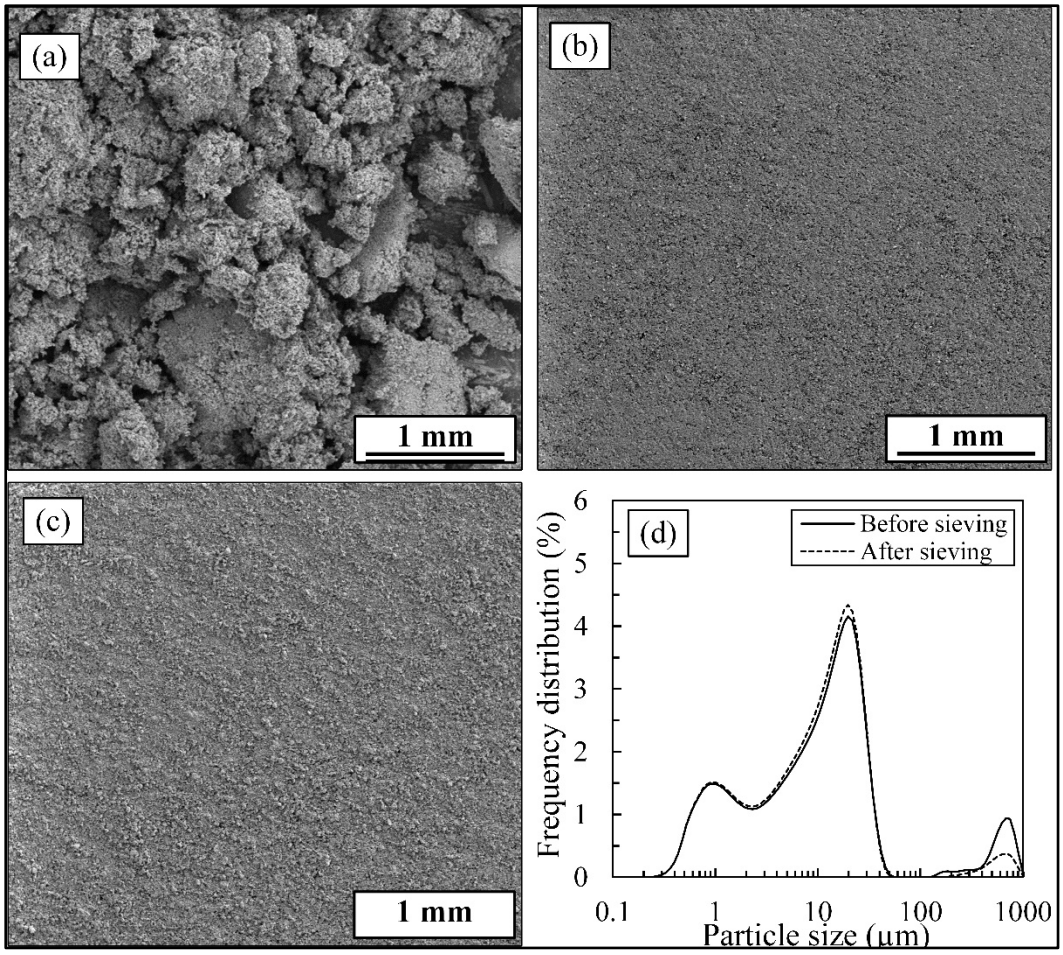

Figure 6.8 (a) Low magnification SEM images of sieved powders (a) -25 μm, (b) -10 μm, (c) -45 μm, and (d) PSD curves of the -25 μm powder before and after sieving

The moldability predictions realized using Weir's model agreed well with the experimental results. That indicates that simple rheological tests can be effectively used during the development phases to predict the flow behavior of such irregular powders before performing time-consuming and costly real-scale injections. Generally speaking, and as demonstrated by German and Bose (German & Bose, 1997), for irregular powders such as ceramics (unlike spherical powders), a narrower size distribution allows easier molding, while a wide size distribution may contribute to molding difficulties. Therefore, for these powder lots, the rheological performance would appear to depend mostly on the slightly different solid loadings, feedstock homogeneity, and binder quantities.

6.4.2 Sintered density and porosity analyses

Figure 6.9 presents the evolution of the specimens' density sintered at 1280ºC for 30, 90, and 270 min. The longer the sintering time, the higher the sintered density of all the powder lots. For the -45 µm specimens, an increase in sintering time from 30 to 90 min leads to an increase in density from 5.6 to 6.1 g/cm^3, but any further increase produces no significant changes, where a value of about 6.2 g/cm^3 is obtained for three-time longer sintering at 270 min. For relatively short sintering times (30 and 90 min), the -25 µm powder behaves similarly to the -45 µm one, but despite their lower moldability and solid loading, after 270 minutes of sintering, the density of -25 µm specimens reaches 6.5 g/cm^3. This result confirms that for such irregular powders, the particle size remains one of the main driving forces for sintering, as can particularly be seen in the -10 µm specimens. Indeed, a relatively low density of about 6.3 g/cm^3 after 30 min of sintering transforms to 7.1 g/cm^3 after 270 min. This value represents the highest sintered density obtained in this work, using the feedstock containing the lowest solid loading of the finest powder particles. Following sintering, a linear shrinkage of about 15, 17, and 20 % was respectively measured for the -45, -25, and -10 µm powders.

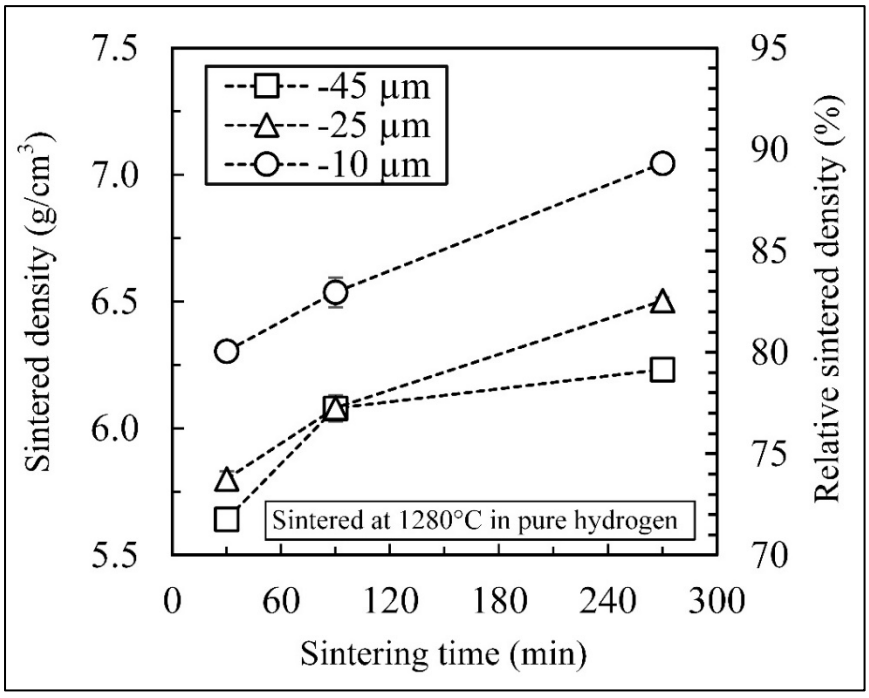

Figure 6.9 Sintered density as a function of sintering time

Note that the maximum relative density of about 90% obtained in this work can be considered a low value because metallic parts produced by MIM usually target a density ranging from 95-99% of the theoretical density. This could be due to the suboptimal sintering conditions used in this study. Previous works on carbonyl iron powder (Hayashi & Lim, 1991) and irregular iron-based powder (Rishmawi, Salarian, & Vlasea, 2018) suggest that this material could be fully densified by increasing the sintered temperature to ~1400°C, which means that the sintered density of these irregular iron-based powders could be improved via the optimization of sintering conditions including the heating rates, sintering times and temperatures. Specifically, this could be expected for the -10 μm specimens, since the sintered density of these specimens exhibits a sharp increase with an increase in the sintering time.

Next, Figure 6.10 shows the morphology and distribution of porosities within the sintered samples for the different powder lots (-45, -25, and -10 μm) and sintering times (30, 90, and 270 min). Note that in Dragonfly software, the 2D measurement of the aspect ratio is defined as the proportional relationship between the minor axis length and the major axis length, where 1.0 corresponds to a proportionate particle, while a value close to 0.1 designates a very elongated pore. In Figure 6.10, elongated pores are highlighted in the yellow to green color range, while the particles ranging from blue to purple are more proportioned. Therefore, it can be observed that an increase in sintering time and a decrease in particle size improve the pore aspect ratio (meaning pores are more circular) and decrease the pore interconnectivity.

For the -45 μm powder, an increase in sintering time from 30 to 90 min changes the morphology and occurrence of porosities significantly (Figure 6.10a-b), while a further increase in sintering time to 270 min produces almost no effect on the porosities network (Figure 6.10b-c). This finding was also previously pointed out from the density measurements presented in Figure 6.9. For the -25 μm powder, a continuous increase in sintering temperature from 30 to 90, and finally to 270 min, results in a significant decrease in the number of pores (Figure 6.10d-f). This was also captured by a continuous increase in density with an increase in the sintering time, as shown in Figure 6.9. However, the aspect ratio and pore interconnectivity remain respectively low and high even after long sintering. The porosity decreases significantly for the -10 μm powder, and pores become more circular as the sintering time increases (Figure 6.10g-i). The latter result confirms a continuous increase in density with

increased sintering time and the highest density obtained with this fine powder, see Figure 6.9.

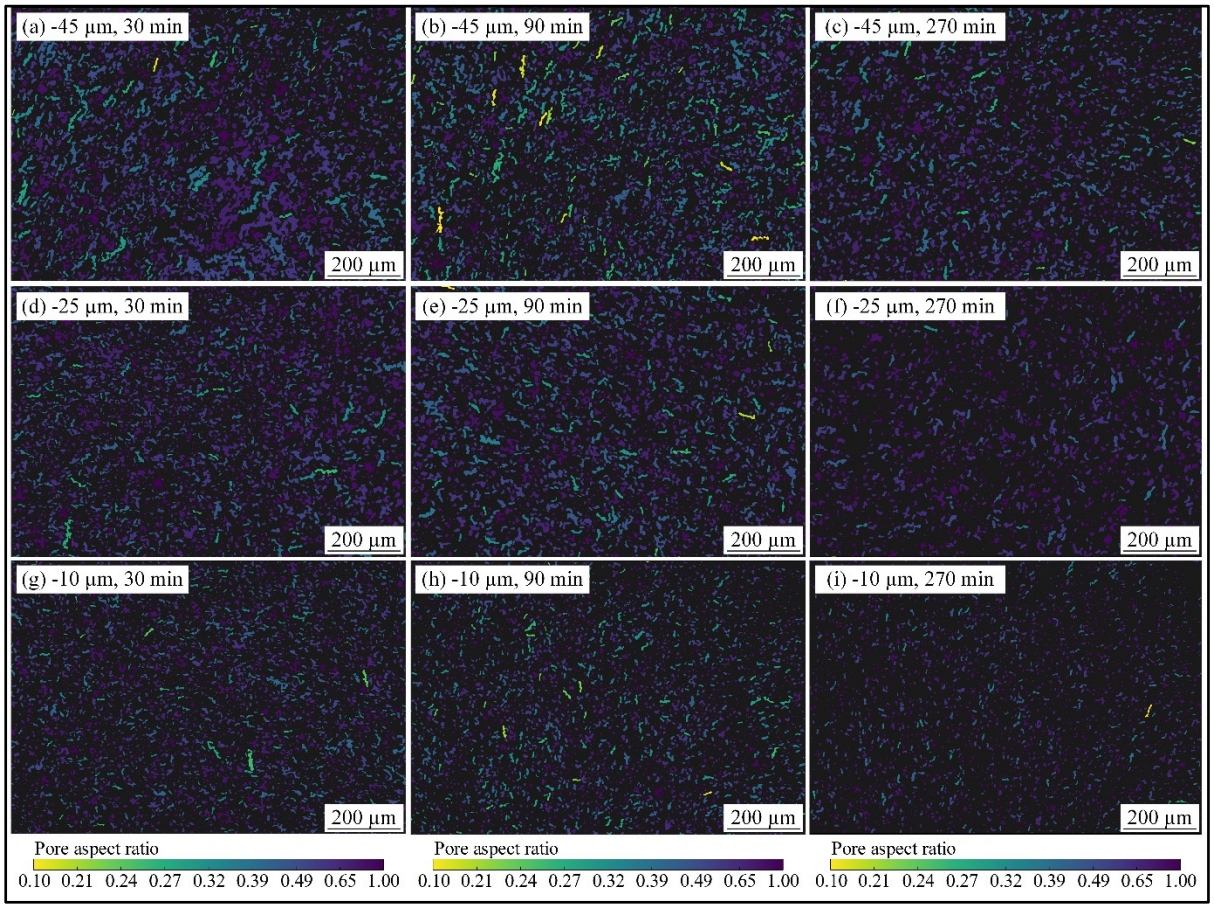

Figure 6.10 Morphology and distribution of porosities within the sintered specimens for (a-c) -45 µm, (d-f) -25 µm, and (g-i) -10 µm according to the sintering time

Figure 6.11 presents the pore equivalent diameter distributions for specimens sintered at different conditions. For the -45 µm powder, the largest equivalent diameter of pores is above 78 µm for specimens sintered for 30 min, whereas the values for the -25 and -10 µm powders are ~38 and ~30 µm, respectively. The average pore equivalent diameter values of all specimens are below 10 µm. It should be noted that although the average pore equivalent sizes are relatively small, the pores have different shapes, ranging from near-circular to highly elongated (discussed above in Figure 6.10), and the larger the pore diameter, the more elongated and irregular its shape; the latter phenomena being responsible for a lower sintered

density and potentially lower mechanical properties.

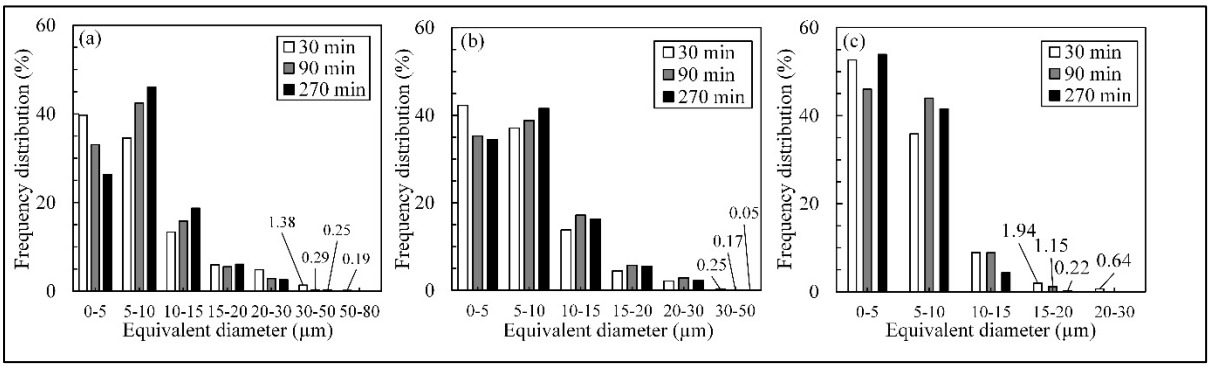

Figure 6.11 Histograms of the pores size distribution of (a) -45 µm, (b) -25 µm, (c) -10 µm sintered for 30, 90, and 270 min

6.4.3 Carbon and oxygen contents

Lowering carbon and oxygen impurity levels in iron components is essential to obtain the desired carbon content and the highest lot-to-lot consistency, stabilizing the final part density and improving mechanical properties. Figure 6.12 shows the oxygen and carbon contents of as-received powders and their evolution during the thermal wick-debinding and sintering processes. As expected from the water atomization production route, the as-received powders presented in Figure 6.12a exhibit a significant oxygen content ranging from 4 to 6 wt. %, with the coarsest (-45 µm) and finest (-10 µm) powders manifesting the lowest and highest oxygen levels, respectively. As detailed by Hariramabadran (Hariramabadran Anantha, 2012), the oxygen content of water-atomized powders is derived entirely from two main sources, namely, the oxygen already present in the liquid metal prior to its atomization in the form of discrete impurity oxides and from surface oxidation caused by the interaction of water vapor with melt during atomization. Both sources are responsible for the high oxygen level in the powder lots used in this project.

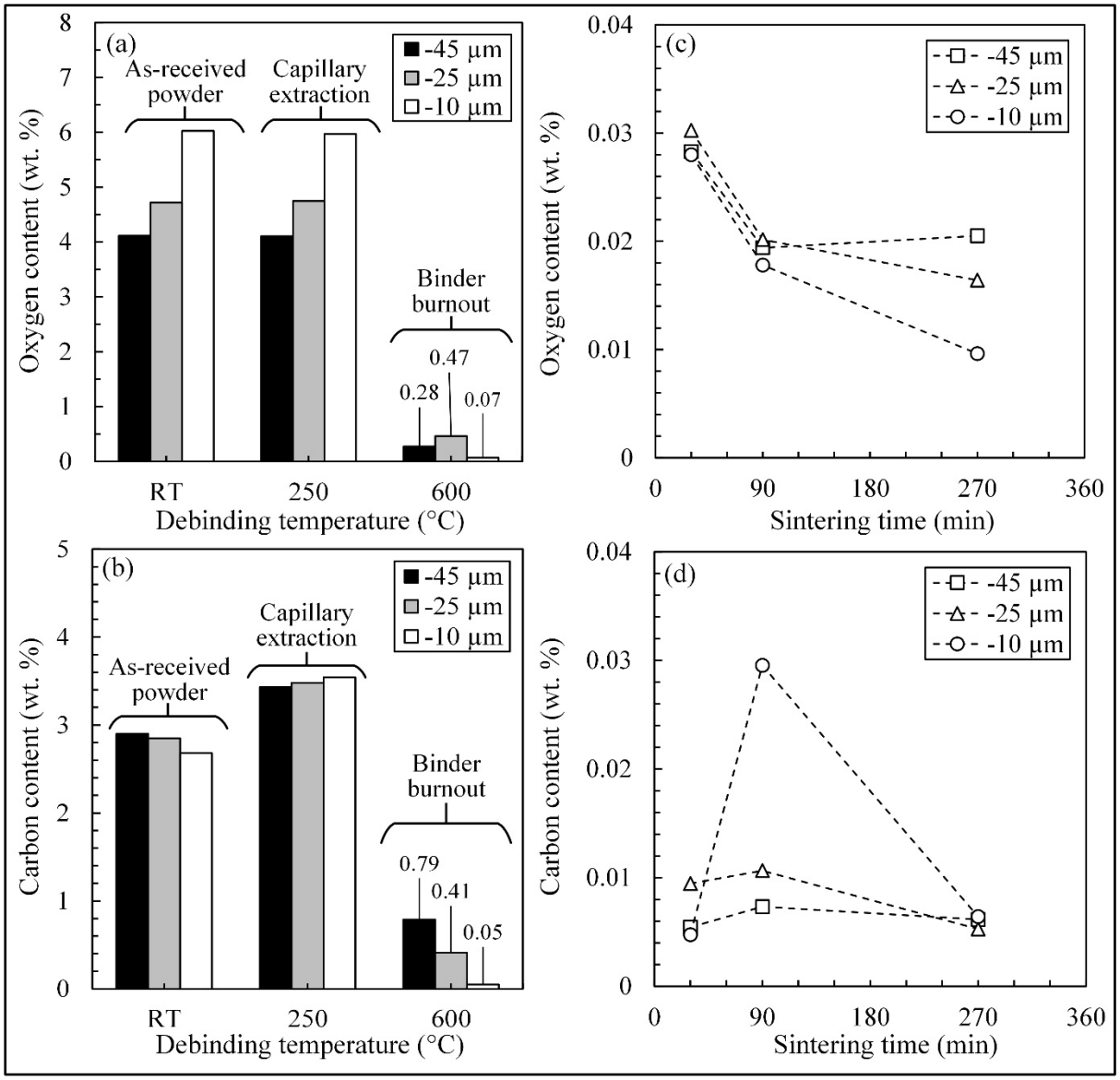

Figure 6.12 Evolution of the oxygen and carbon contents during (a-b) debinding and (c-d) sintering processes

Debinding

During its run, the thermal wick-debinding process was interrupted following the capillary binder extraction phase performed at 250°C to confirm that there had been no changes in oxygen content during that specific stage (identified in Figure 6.12a as the debinding conditions RT vs. 250). However, a Leco analysis performed on the pre-sintered specimens confirmed that an increase in the debinding temperature from 250 to 600°C significantly

decreases the oxygen content to 0.07-0.47 wt. %. Note that this temperature range represents the minimum value needed to promote the final binder burnout stage (around 450°C) and the pre-sintering of powders (around 600°C) required to promote the brown strength for removal of the specimens from the debinding cell. On one hand and similarly observed by another research group (J. Y. Park et al., 2020), a decrease in oxygen content during the debinding process may partially be explained by a reduction of iron-rich oxides (i.e., surface oxidation) in the argon atmosphere since the oxygen's partial pressure is lower than the dissociation pressure of the oxide. On the other hand, oxygen level reduction during the debinding process could be caused by carbon already present in powder (D. F. Heaney, 2019). In this context, for the -25 μm samples, a relatively higher oxygen level (i.e., 0.47 wt. %) probably indicates the presence of more thermodynamically stable oxides that cannot be easily reduced in an inert atmosphere of the debinding furnace.

The X-ray diffraction pattern obtained on the debound -25 μm specimen is plotted in Figure 6.13a ($30° < 2\theta < 120°$; step size of 0.033°). Three sharp diffraction peaks at $2\theta = 52.42°$, 77.31° and 99.82° indicate the existence of α-Fe (RC 04-014-0171). Also, the low intensity peaks corresponding to Fe_3O_4, FeO, and SiO_2 oxides are clearly seen. A second XRD scan obtained at higher resolution in b ($30° < 2\theta < 65°$; step size of 0.008°) confirms the presence of these oxides (RC 04-012-7038, 01-086-8047, and 01-089-8937), which is inline with the LECO analysis reporting more stable oxides in Fig. 12a. Although the presence of magnetite and iron oxides is expected after debinding, the presence of silicon oxide could explain the issues observed during the PSD measurements as well as the difficulties occurring during injection and sintering of the feedstock containing this specific powder.

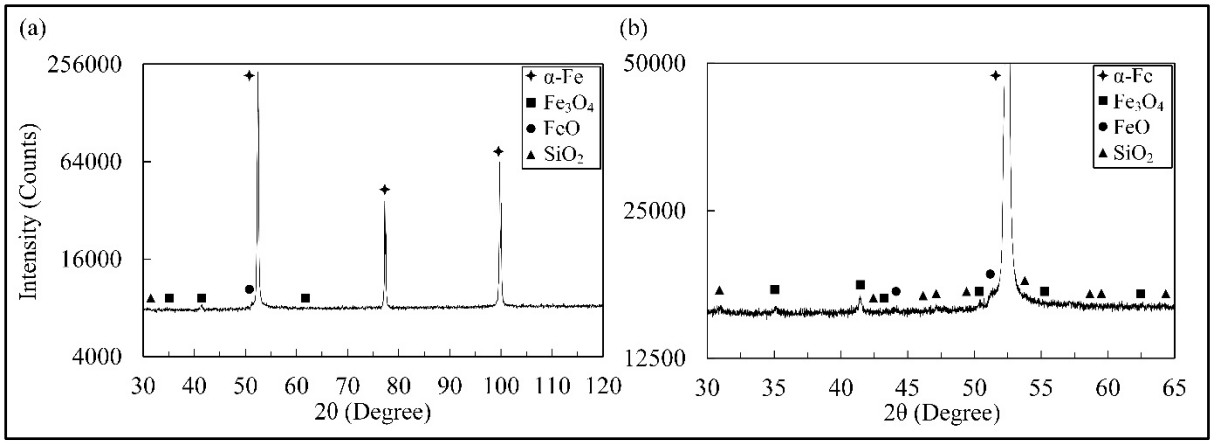

Figure 6.13 XRD analysis of -25µm debound part of (a) 30° < 2θ < 120° with step size of 0.033° and (b) 30° < 2θ < 65° with step size of 0.008°

Figure 6.12b shows a relatively constant carbon content value ranging from 2.7 to 2.9 wt. % that was measured from the as-received powders. Despite a slight increase of about 0.5-0.6 wt. % of carbon during the binder extraction stage (i.e., at 250°C), a downward trend in the carbon content similar to that observed with the oxygen content occurred during the high-temperature debinding stage (i.e., at 600°C). On the one hand, an increase in carbon content after capillary extraction is probably due to carbon residues from the pendular binder captured within the powder network during the first debinding step. However, a significant decrease in oxygen and carbon contents following the final burnout stage suggests that carbon in the powder reduces oxygen, similar to the mechanism described in (D. F. Heaney, 2019).

Sintering

The evolution of the oxygen and carbon contents measured in the sintered specimens is also shown in Figure 6.12c-d. Taking the oxygen/carbon levels measured after the second debinding stage as the input value before sintering (values obtained at 600°C in Figure 6.12a-b), it can be concluded that sintering under a hydrogen atmosphere for only 30 min reduced the oxygen content by 2 to 16 times, and the carbon content by 10 to 80 times, depending on the powder lot. An increase in sintering time from 30 to 90 min promotes oxygen reduction, decreasing the oxygen content from 300 to 200 ppm. For the -45 µm powder, an increase in

sintering time up to 270 min produces almost no measurable changes in the oxygen content but appears to have a positive impact on the oxygen levels in the -25 µm and -10 µm powders, with a decrease to 170 and 100 ppm, respectively. Nevertheless, all specimens sintered for 90 min exhibit slightly higher carbon contents, that reaches 300 ppm for the -10 µm specimens. Although these carbon contents remain within the specifications for this material, the unexpected variations in the carbon content might be due to variations in sintering conditions, which are more critical for fine powder feedstock. Excluding an outlier value obtained after a 90 min sintering, the carbon content in sintered parts for all conditions reported in Figure 6.12d is below 100 ppm. A high carbon content value of about 300 ppm in the -10 µm powders after 90 min sintering is discussed below, along with the tensile properties.

To sum up, it was observed that the carbon and oxygen contents of all sintered specimens were within acceptable ranges for pure sintered iron. However, interestingly, the high oxygen and carbon contents of such low-cost water-atomized powders were reduced to levels equivalent to those required for pure iron (Konttinen et al., 2014). In this context, and since the sintered density exhibited an increasing trend with increasing sintering time, it could be reasonably concluded that an increase in sintering time and/or temperature may improve the density and subsequent mechanical performance of sintered products produced using these irregular shape powders.

6.4.4 Microstructure

Figure 6.14 shows the microstructure of specimens sintered for 30, 90, and 270 min; due to the strong reducing effect of hydrogen at high temperatures, the presence of C and O impurities was significantly reduced. However, as indicated by white arrows in Figure 6.14a-c, all parts show original particle boundaries, angular pores, and small inclusions inside the round pores. These inclusions may be due to the incomplete reduction of oxides or incomplete sintering of smaller particles for all samples sintered for 30 min. As the sintering time increases from 30 to 90 min, the pore distribution homogeneity increases, and thanks to pore closure, the number of round pores decreases (Figure 6.14d-f). Microstructures obtained after a 270 min sintering

time exhibit a higher material densification and continuity for the -25 and -10 μm powders (Figure 6.14h-i). In addition, fine particles in small pores (indicated in Figure 6.14i by white arrows) could be used as a sintering driving force for further densification of -10 μm powders. As previously seen in the low magnification optical images presented in Figure 6.10, the -45 μm specimens (Figure 6.14g) still exhibit large and almost interconnected pores, which are certainly responsible for a small density increase (from ~ 6.1 to 6.2 g/cm3), corresponding to a three-fold increase in sintering time (from 90 to 270 min). Finally, and regardless of the sintering time, these high-magnification SEM observations confirm that the microstructures obtained with the -10 μm powder exhibit a more spherical and finer pore network than that obtained with the other powders used in this work. Likewise, fine-grained structure and the presence of pores at the grain boundaries in the -10 μm specimens suggest that sintering temperature could be possibly increased to complete the microstructure formation and to increase the density and mechanical properties. These optimum sintering conditions still need to be determined.

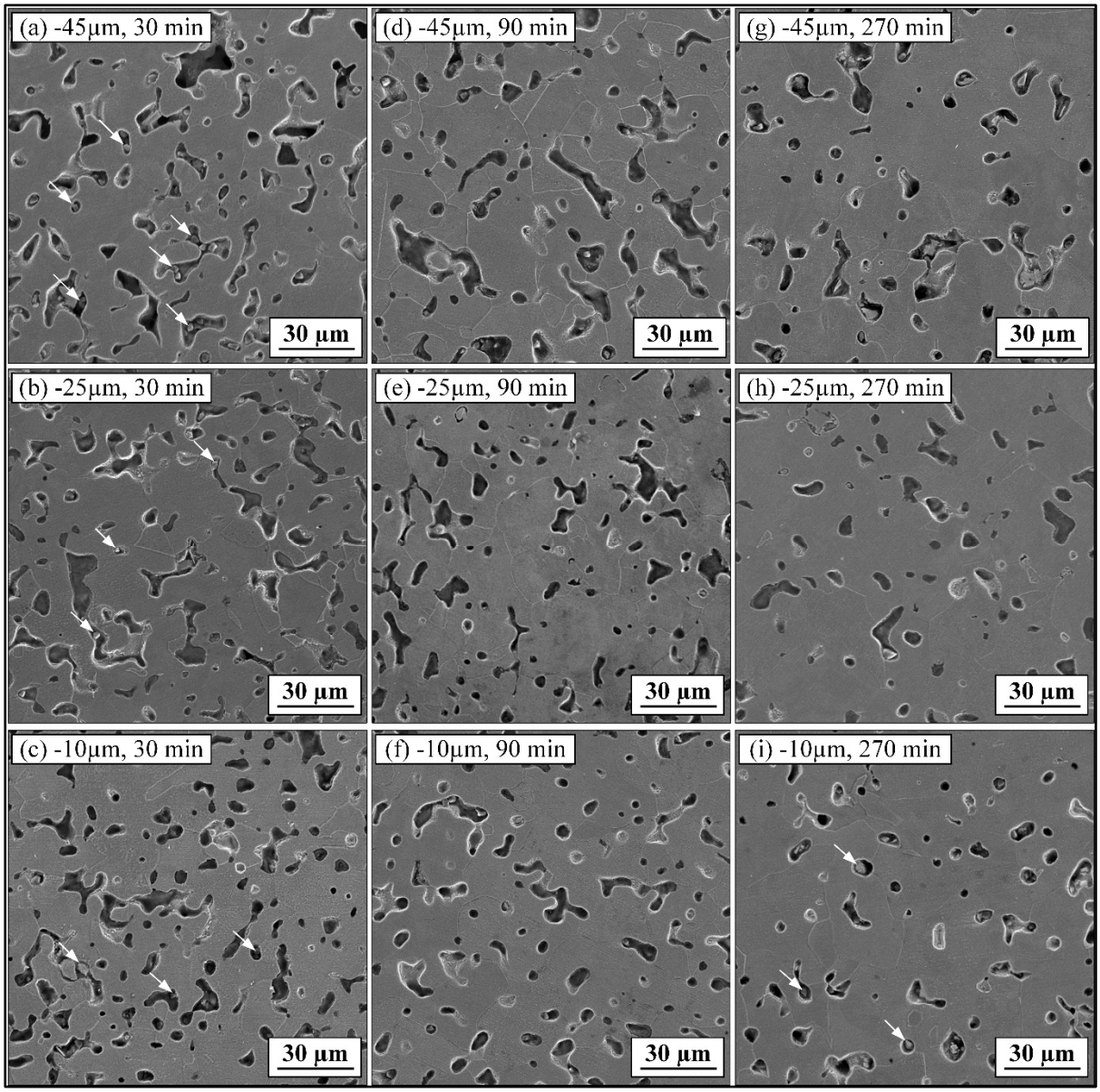

Figure 6.14 Effect of sintering time (a-c) 30 min, (d-f) 90 min, and (g-i) 270 min on the microstructures of sintered samples (arrows show fine unsintered particles)

6.4.5 Tensile properties

The ultimate tensile strength (UTS), the yield strength (YS), and the elongation at break (EL%) were evaluated for different conditions (3 powder lots and 3 sintering times) and are reported in Figure 6.15 (average values and standard deviations). Consistent with the density values

obtained in Figure 6.9, an increase in sintering time led to increased material strength (UTS and YS) and ductility (EL%). This result, often observed in MIM, is directly related to a combined growth of the interparticle bonds and changes in the pore structure (D. F. Heaney, 2019). Using the maximum 270 min sintering time on -10 μm powders, a UTS value of ~225 MPa and an EL% value of 23% were obtained in this work.

However, the YS values are more complex to analyze. The YS values trend in Figure 6.15b is, in fact, similar to that observed for the UTS in Figure 6.15a, except for the 90 min-sintered -10 μm specimen. To better understand these inconsistencies, the stress-strain curves of the -10 μm specimens were plotted in Figure 6.15d for the three sintered times. It can be observed that the specimens sintered for 30 and 270 min both exhibit smooth elastic-plastic transitions, but the one sintered for 90 min reveals a clear discontinuity in this region of the curve, well-known as the yield point phenomenon. Mariot et al. (Mariot et al., 2016) reported the same phenomenon for iron-based MIM, and Letenneur et al. (Letenneur, Brailovski, Kreitcberg, Paserin, & Bailon-Poujol, 2017) also observed upper and lower proportional limits for pure iron manufactured using the press-and-sinter and laser powder bed fusion technologies. Since the yield point phenomenon generally results from small atom clusters interfering with a dislocation slip, the higher carbon content noted above as a non-standard value in Figure 6.15d could contribute to producing this artifact in the observed YS properties trend. Note that all other stress-strain curves obtained with other powders and sintering conditions exhibit a smooth elastic-plastic transition similar to those observed in Figure 6.15d for 270 min.

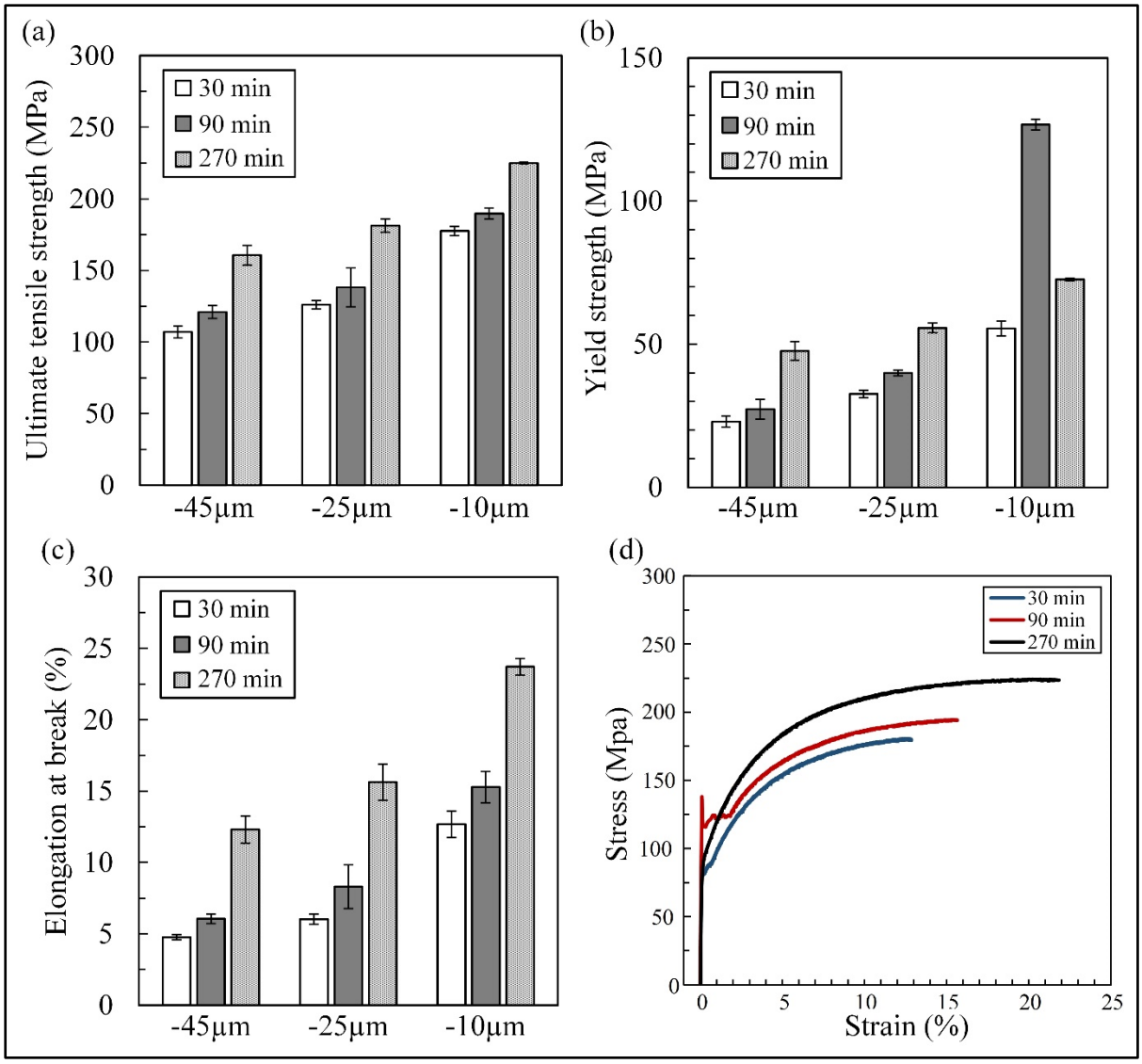

Figure 6.15 Effect of sintering time on the mechanical properties of sintered specimens: (a) UTS, (b) YS, (c) EL%, and (d) typical stress-strain curves of the -10 µm powders sintered during 30, 90, and 270 min

To summarize, the -45µm specimens sintered at 1280ºC for 270 min exhibited a final density of 6.2 g/cm^3, a UTS of 161 ± 7 MPa, a YS of 48 ± 3 MPa, and an EL% of 12%, while the -10 µm specimens sintered using the same conditions demonstrated a density of 7.1 g/cm^3, a UTS of 225 ± 1 MPa, YS of 73 ± 3 MPa, and an EL% of 24%. The density and mechanical properties of the -25 µm specimens were closer to those obtained with their -45 µm equivalents. These

mechanical properties were similar to those obtained with the MIM parts produced from fine spherical iron powders (Mariot et al., 2016; Tavares, Mariot, Costa, & Schaeffer, 2019).

6.5 Conclusion

This study demonstrated the feasibility of using economical water-atomized iron powders for MIM applications, and the conclusions are summarized as follows:

- For feedstocks of this work produced from three irregular iron-based powders with wide particle size distributions, the moldability is mostly affected by small solid loading variations, not particle size distribution variations.
- As observed for the -25 μm powder, the tendency to form agglomerations could create difficulties when mixing and debinding water-atomized powders and may also affect the oxygen content of debound parts.
- For the iron-based powders used in this study, the debinding process performed under pure argon could change the chemical composition of the as-received powder through oxide reduction and oxygen and carbon removal and continue to reduce them under a pure hydrogen atmosphere during the sintering process.
- Among the three powders used in this study, the -10 μm powder showed the best moldability (mostly from a lower solid loading) and sinterability (higher density and mechanical properties).
- Although an increase in sintering time from 30 to 270 min resulted in increased densification and improved mechanical properties, especially for the -25 and -10 μm powders, further investigation is needed to define the sintering envelope (i.e., the maximum sintering time) and to study the effect of sintering temperature and heating rate on the densification and mechanical properties of a sintered product.

6.6 Funding

This work was carried out with the financial support of the Natural Sciences and Engineering Research Council of Canada (Grant CRDPJ505289-16).

6.7 Acknowledgments

The authors would like to express their utmost gratitude and thanks to Danny Plamondon, Francis Ares, Salah Eddine Brika, Raphaël Côté, Alena Kreitcberg, Etienne Moquin, Lounes Ouarab, and Rémi Recoquille for their assistance during this project.

CONCLUSION

In this project, the processability of under development iron-based powders for LPIM processing technique was evaluated based on feedstock moldability, debindability, and sinterability of injected parts. The conclusions are summarized as follows:

A total of 36 different feedstocks formulated from one irregular iron-based powder (D_{50} =16.6 μm) and the influence of different binder additives (i.e., surfactants, shrinkers, and thickeners) and their proportions in a wax-based binder system on molding properties and solid loading of irregular iron-based feedstock was studied. The viscosity profiles were used to quantify the threshold proportions of each binder constituent, and the feedstock pycnometer density was used to identify maximum solid loading to identify the three best feedstock formulations. As a result, PW-1SA, PW-1SA-2EVA, and PW-1SA-2EVA-2CW were selected as the best binder candidates to prepare the feedstocks with three different solid loadings (50, 54, and 58 vol. %) to calculate their moldability indices validated using real-scale injections into a spiral mold. Finally, feedstocks with maximum solid loadings (58 vol. %) were injected into a typical mold cavity to demonstrate the molding capability of these feedstock formulations, where the green parts showed smooth surfaces and no apparent defects. It was concluded that from the molding perspective, the feedstock prepared from PW-1SA-2EVA-2CW with solid loading of 58 vol. % is the optimal formulation for this irregular iron powder that exhibits the optimization for further experiments.

To demonstrate the debindability of the irregular iron-based powder, the feedstock was prepared from one irregular iron-based powder (D_{50} = 16.6 μm) and one wax-based binder system consisting of 42 vol. % of PW as the main carrier, 2 vol. % of SA promoting the wettability, and 1 vol. % of EVA as a thickener, at a solid loading of 55 vol. %. The feedstock was injected into a rectangular mold cavity to obtain green parts that were subsequently debound and sintered. The thermal wick debinding was selected based on the low-viscosity LPIM binder system, where three different pre-sintering temperatures (600, 700, and 850°C)

were used to evaluate the effect of debinding parameters on final sintered properties. It was observed that the wick thermal debinding process under inert gas (i.e., argon) considerably decreased the oxygen and carbon contents. Also, an increase in pre-sintering temperature from 600 to 850°C decreases the occurrence of fine loose powder distributed in the debound structure. Finally, the sintering was performed at 1250°C under a hydrogen atmosphere for 90 min. The density measurement and metallographic observation confirm that an increase in the pre-sintering temperature results in a higher degree of pore interconnectivity and reduced sintered density. As a result, the presintering temperature of 600°C laid the highest sintered density, where the porosity level in metallographic observations was also in line with this density value.

To assess the full potential of the LPIM technique using the irregular iron-based powders and evaluate the effect of particle size distribution on mechanical properties, three coarse, medium, and fine powders (i.e., D_{50} of about 13, 11, and 6 μm, respectively) were used to prepare feedstocks with the previously optimized binder formulation. The injected rectangular bars were then debound using thermal wick debinding with a debinding cycle developed earlier in this project and sintered at 1280 °C under a hydrogen atmosphere for 30, 90, and 270 min to evaluate the effect of sintering time on physical and mechanical properties of sintered parts. The sintered bar subsequently machined to produce tensile specimens to study the mechanical properties where an increase in sintering time from 30 to 270 min resulted in increased mechanical properties, especially for the fine powder.

New information has been developed regarding the processability of relatively cheap iron-based powders for complex metallic components. To improve its competitiveness in powder production, Rio Tinto Metal Powder will use this new knowledge to define the molding, debinding, and sintering performance of its powders for PIM. This will allow them to design new powders specifically designed for PIM processing. Furthermore, company engineers evaluated the flowability, moldability, and density relationship for typical powder lots they produce based on the research results.

RECOMMENDATIONS

The results obtained in this research demonstrated the processability of irregular powders via LPIM. It is, therefore, interesting to direct future research on this subject through the following recommendations in LPIM of irregular shape metal powder as follows:

- There is a lack of knowledge of the numerical simulation of the injection phase of LPIM of irregular metal powders and the effect of powder characteristics on defect generation and segregation occurrence. It could be an interesting topic for further study.
- The thermal wick-debinding of complex shape parts could open up new research opportunities and challenges since the ultimate goal is to fabricate defect-free intricate parts in LPIM.
- The effect of sintering parameters such as atmosphere, temperature, heating rate, and holding time could be further studied to achieve improved sinter properties.
- A detailed and comprehensive study on shrinkage and densification of the irregular iron-based powder during LPIM could be ideal for improving repeatability, predictability, dimensional tolerance, and, therefore, the quality of the final product.

To sum up, to acquire more in-depth knowledge about how and why the powder behaves the way it does during the mixing, injection, debinding, and sintering, more extensive investigation should be done.

LIST OF BIBLIOGRAPHICAL REFERENCES

Agote, I., Odriozola, A., Gutierrez, M., Santamaría, A., Quintanilla, J., Coupelle, P., & Soares, J. (2001). Rheological study of waste porcelain feedstocks for injection moulding. *Journal of the European Ceramic Society*, *21*(16), 2843–2853. https://doi.org/10.1016/S0955-2219(01)00210-2

Ahn, S., Park, S. J., Lee, S., Atre, S. V., & German, R. M. (2009). Effect of powders and binders on material properties and molding parameters in iron and stainless steel powder injection molding process. *Powder Technology*, *193*(2), 162–169. https://doi.org/10.1016/j.powtec.2009.03.010

Ali, G., Demers, V., Côté, R., & Demarquette, N. R. (2020). Threshold concentration of surfactant agent in feedstocks used for low-pressure powder injection molding. *Materials Performance and Characterization*, *9*(4). https://doi.org/10.1520/MPC20190149

Ali, M., & Ahmad, F. (2020). Influence of powder loading on rheology and injection molding of Fe-50Ni feedstocks. *Materials and Manufacturing Processes*, *35*(5), 579–589. https://doi.org/10.1080/10426914.2020.1734616

Ali, M., Ahmad, F., Melor, P. S., Yahya, N., Altaf, K., Omar, M. A., & Aslam, M. (2019). Binder removal by a two-stage debinding process for powder injection molding Fe-50Ni alloy parts. *Materials Research Express*, *6*(8). https://doi.org/10.1088/2053-1591/ab239b

Amin, S. Y. M., Jamaludin, K. R., & Muhamad, N. (2009). Rheological Properties of Ss316L Mim Feedstock Prepared With Different Particle Sizes and Powder Loadings. *The Institution of Engineers, Malaysia*, *71*(2), 59–63.

Aslam, M., Ahmad, F., Sri, P., Binti, M., Yusoff, M., Altaf, K., … Raza, M. R. (2016). Investigation of Rheological Behavior of Low Pressure Injection Molded Stainless Steel Feedstocks. *Advances in Materials Science and Engineering*, *2016*, 1–9. https://doi.org/10.1155/2016/5347150

Aslam, M., Ahmad, F., Yusoff, P. S. M. B. M., Altaf, K., Omar, M. A., & German, R. M. (2016). Powder injection molding of biocompatible stainless steel biodevices. *Powder Technology*, *295*, 84–95. https://doi.org/10.1016/j.powtec.2016.03.039

ASTM B923-16. (2016). Standard Test Method for Metal Powder Skeletal Density by Helium or Nitrogen. *ASTM International*, *02*(Reapproved 2008), 3–6. https://doi.org/10.1520/B0923-10

ASTM B923 - 16. (2016). Standard Test Method for Metal Powder Skeletal Density by Helium or Nitrogen Pycnometry. *ASTM International*, 3–6. https://doi.org/10.1520/B0923-10

ASTM International, Materials, A. S. for T. and, & ASTM International. (2012). Standard Test

Method for Transition Temperatures and Enthalpies of Fusion and Crystallization of Polymers by Differential Scanning. In *ASTM Standard* (Vol. D4318-21, pp. 1–7). Conshohocken, PA: ASTM International. https://doi.org/10.1520/D3418-21.

Atre, S. V., Enneti, R. K., Park, S. J., & German, R. M. (2008). Master decomposition curve analysis of ethylene vinyl acetate pyrolysis: Influence of metal powders. *Powder Metallurgy*, *51*(4), 368–375. https://doi.org/10.1179/174329008X286622

Attia, U. M., Hauata, M., Walton, I., Annicchiarico, D., & Alcock, J. R. (2014). Creating movable interfaces by micro-powder injection moulding. *Journal of Materials Processing Technology*, *214*(2), 295–303. https://doi.org/10.1016/j.jmatprotec.2013.09.012

Auscher, M. C., Fulchiron, R., Fougerouse, N., Périé, T., & Cassagnau, P. (2017). Zirconia based feedstocks: Influence of particle surface modification on the rheological properties. *Ceramics International*, *43*(18), 16950–16956. https://doi.org/10.1016/j.ceramint.2017.09.100

Bandyopadhyay, G., & French, K. W. (1993). Injection-molded ceramics: Critical aspects of the binder removal process and component fabrication. *Journal of the European Ceramic Society*, *11*(1), 23–34. https://doi.org/10.1016/0955-2219(93)90055-V

Bao, Q., Yang, Y., Wen, X., Guo, L., & Guo, Z. (2021). The preparation of spherical metal powders using the high-temperature remelting spheroidization technology. *Materials and Design*, *199*(30), 109382. https://doi.org/10.1016/j.matdes.2020.109382

Ben Trad, M. A., Demers, V., & Dufresne, L. (2019). Effect of Powder Shape and Size on Rheological, Thermal, and Segregation Properties of Low-Pressure Powder Injection Molding Feedstocks. *Journal of Materials Engineering and Performance*, *28*(9), 5551–5562. https://doi.org/10.1007/s11665-019-04276-9

Bhowmick, M., Sengodan, T., & Thangavel, S. (2014). Evaluation and Characterization of Transdermal Therapeutic Systems: an Exhaustive Pictorial and Figurative Review. *Journal of Drug Delivery and Therapeutics*, *4*(6), 9–22. https://doi.org/10.22270/jddt.v4i6.664

Boisvert, M., Christopherson, D., Beaulieu, P., & L'Espérance, G. (2017). Treatment of ferrous melts for the improvement of the sphericity of water atomized powders. *Materials and Design*, *116*, 644–655. https://doi.org/10.1016/j.matdes.2016.12.059

Chan, T., & Lin, S. (1995). Effects of stearic acid on the injection molding of alumina. *Journal of the American Ceramic Society*, *78*(10), 2746–2752.

Chandra, D., & Vishal, V. (2021). A critical review on pore to continuum scale imaging techniques for enhanced shale gas recovery. *Earth-Science Reviews*, *217*(April), 103638. https://doi.org/10.1016/j.earscirev.2021.103638

Chartier, T., Ferrato, M., & Baumard, J. F. (1995). Supercritical Debinding of Injection Molded

Ceramics. *Journal of the American Ceramic Society*, *78*(7), 1787–1792. https://doi.org/10.1111/j.1151-2916.1995.tb08890.x

Checot-Moinard, D., Rigollet, C., & Lourdin, P. (2011). Powder injection moulding PIM of feedstock based on hydrosoluble binder and submicronic powder to manufacture parts having micro-details. *Powder Technology*, *208*(2), 472–479. https://doi.org/10.1016/j.powtec.2010.08.045

Chen, G., Zhao, S. Y., Tan, P., Wang, J., Xiang, C. S., & Tang, H. P. (2018). A comparative study of Ti-6Al-4V powders for additive manufacturing by gas atomization, plasma rotating electrode process and plasma atomization. *Powder Technology*, *333*, 38–46. https://doi.org/10.1016/j.powtec.2018.04.013

Choi, J. P., Lyu, H. G., Lee, W. S., & Lee, J. S. (2014). Densification and microstructural development during sintering of powder injection molded Fe micro-nanopowder. *Powder Technology*, *253*, 596–601. https://doi.org/10.1016/j.powtec.2013.11.048

Choi, J. P., Park, J. S., Hong, E. J., Lee, W. S., & Lee, J. S. (2017). Analysis of the rheological behavior of Fe trimodal micro-nano powder feedstock in micro powder injection molding. *Powder Technology*, *319*, 253–260. https://doi.org/10.1016/j.powtec.2017.06.056

Claudel, D., Mohamed, S., Thierry, B., & Jean-Claude, G. (2017). Influence of particle-size distribution and temperature on the rheological properties of highly concentrated Inconel feedstock alloy 718. *Powder Technology*, *322*, 273–289. https://doi.org/10.1016/j.powtec.2017.08.049

Da Silveira, W., Wendhausen, P. A. P., & Klein, A. N. (2008). Study of the Debinding rate on MIM parts using Plasma Assisted Debinding. *Materials Science Forum*, *591–593*, 229–234. https://doi.org/10.4028/www.scientific.net/msf.591-593.229

Dehghan-Manshadi, A., Bermingham, M. J., Dargusch, M. S., StJohn, D. H., & Qian, M. (2017). Metal injection moulding of titanium and titanium alloys: Challenges and recent development. *Powder Technology*. https://doi.org/10.1016/j.powtec.2017.06.053

Dehghan-Manshadi, A., StJohn, D., Dargusch, M., Chen, Y., Sun, J. F., & Qian, M. (2018). Metal injection moulding of non-spherical titanium powders: Processing, microstructure and mechanical properties. *Journal of Manufacturing Processes*, *31*, 416–423. https://doi.org/10.1016/j.jmapro.2017.12.004

Demers, V., Fareh, F., Turenne, S., Demarquette, N. R., & Scalzo, O. (2018). Experimental study on moldability and segregation of Inconel 718 feedstocks used in low-pressure powder injection molding. *Advanced Powder Technology*, *29*(1), 180–190. https://doi.org/10.1016/j.apt.2017.10.025

Demers, V., Turenne, S., & Scalzo, O. (2015). Impact of binders on viscosity of low-pressure powder injection molded Inconel 718 superalloy. *Journal of Materials Science*, *50*(7),

2893–2902. https://doi.org/10.1007/s10853-015-8853-z

Demétrio, K. B., Klein, A. N., Schaeffer, L., Consoni, D. R., Martinelli, A. E., & Bendo, T. (2013). Sinterability and microstructure evolution during sintering of ferrous powder mixtures. *Materials Research*, *16*(5), 1030–1038. https://doi.org/10.1590/S1516-14392013005000078

Deng, L., Qiao, L., Zheng, J., Ying, Y., Yu, J., Li, W., … Cai, W. (2019). Injection molding, debinding and sintering of ZrO2 ceramic modified by silane couping agent. *Journal of the European Ceramic Society*, *40*(September), 1566–1573. https://doi.org/10.1016/j.jeurceramsoc.2019.11.069

Dihoru, L. V., Smith, L. N., & German, R. M. (2000). Experimental analysis and neural network modelling of the rheological behaviour of powder injection moulding feedstocks formed with bimodal powder mixtures. *Powder Metallurgy*, *43*(1), 31–36. https://doi.org/10.1179/pom.2000.43.1.31

Edirisinghe, M. J., & Evans, J. R. G. (1986). Review: Fabrication of engineering ceramics by injection moulding. I. Materials selection. *International Journal of High Technology Ceramics*, *2*(1), 1–31. https://doi.org/10.1016/0267-3762(86)90002-0

Enneti, R. K. K., Onbattuvelli, V. P. P., Gulsoy, O., Kate, K. H. H., & Atre, S. V. V. (2019). 4 - Powder-binder formulation and compound manufacture in metal injection molding (MIM). In D. F. B. T.-H. of M. I. M. (Second E. Heaney (Ed.), *Woodhead Publishing Series in Metals and Surface Engineering* (2nd ed., pp. 57–88). Woodhead Publishing. https://doi.org/https://doi.org/10.1016/B978-0-08-102152-1.00005-2

Eshel, G., Levy, G. J., Mingelgrin, U., & Singer, M. J. (2004). Critical Evaluation of the Use of Laser Diffraction for Particle-Size Distribution Analysis. *Soil Science Society of America Journal*, *68*(3), 736–743. https://doi.org/10.2136/sssaj2004.7360

Exner, H. E. E., & Weinbruch, S. (2004). Scanning Electron Microscopy. In G. F. Vander Voort (Ed.), *Metallography and Microstructures* (Vol. 9, pp. 355–367). ASM International. https://doi.org/10.31399/asm.hb.v09.a0003755

Fan, J. L., Han, Y., Liu, T., Cheng, H. C., Gao, Y., & Tian, J. M. (2013). Influence of surfactant addition on rheological behaviors of injection-molded ultrafine 98W-1Ni-1Fe suspension. *Transactions of Nonferrous Metals Society of China (English Edition)*, *23*(6), 1709–1717. https://doi.org/10.1016/S1003-6326(13)62652-7

Fareh, F., Demers, V., Demarquette, N. R., Turenne, S., & Scalzo, O. (2017). Influence of segregation on rheological properties of wax-based feedstocks. *Powder Technology*, *320*, 273–284. https://doi.org/10.1016/j.powtec.2017.07.056

Fedorchenko, I. M., & Skorokhod, V. V. (1967). Theory and practice of sintering. *Soviet Powder Metallurgy and Metal Ceramics*, *6*(10), 790–805.

https://doi.org/10.1007/BF00773720

Ferreira, T., & Rasband, W. (2011). The ImageJ 1.44 User Guide. *Manager*, 1–199.

Foong, M. L., & Tam, K. C. (1998). Application of Polymer Technology to Metal Injection Molding (MIM) Processing. In *Advanced polymer processing operations* (pp. 213–280). Elsevier.

Friederang, A. W., & Schlegel, R. (1999). BASF continues to evolve carbonyl iron powders. *Metal Powder Report*, *54*(3), 18–20. https://doi.org/10.1016/S0026-0657(99)80339-7

Gelin, J. C., Barriere, T., & Song, J. (2009). Processing Defects and Resulting Mechanical Properties After Metal Injection Molding. *Journal of Engineering Materials and Technology*, *132*(1), 011017. https://doi.org/10.1115/1.2931155

German, R. M. (1987). THEORY OF THERMAL DEBINDING. *International Journal of Powder Metallurgy (Princeton, New Jersey)*, *23*(4), 237–245.

German, R. M. (2003). *Powder injection molding: design and applications*. Innovative Material Solutions, Inc.

German, R. M. (2013). Progress in titanium metal powder injection molding. *Materials*, *6*(8), 3641–3662. https://doi.org/10.3390/ma6083641

German, R. M. (2016). Sintering Simplified: Surface Area, Density, and Grain Size Relations. *Materials Science Forum*, *835*(January), 50–75. https://doi.org/10.4028/www.scientific.net/MSF.835.50

German, R. M., & Bose, A. (1997). *Injection Molding of Metals and Ceramics*. *Metal Powder Industries Federation, Princeton, NJ*. Princeton: Metal powder industries federation Princeton.

Ghanmi, O., & Demers, V. (2021). Molding properties of titanium-based feedstock used in low-pressure powder injection molding. *Powder Technology*, *379*, 515–525. https://doi.org/10.1016/j.powtec.2020.10.068

Gonçalves, A. C. (2001). Metallic powder injection molding using low pressure. *Journal of Materials Processing Technology*, *118*(1–3), 193–198. https://doi.org/10.1016/S0924-0136(01)00916-5

González-gutiérrez, J., Beulke Stringari, G., Emri, I., Stringari, G. B., & Emri, I. (2012). Powder Injection Molding of Metal and Ceramic Parts. *Some C*.

González-gutiérrez, J., Stringari, G. B., & Emri, I. (2012). Powder Injection Molding of Metal and Ceramic Parts, Some Critical Issues for Injection Molding. *Some Critical Issues for Injection Molding*, 65–88. https://doi.org/10.1126/science.1094581

Gorjan, L. (2012). Wick Debinding - An Effective Way of Solving Problems in the Debinding Process of Powder Injection Molding. *Some Critical Issues for Injection Molding*. https://doi.org/10.5772/34969

Gorjan, L., Dakskobler, A., & kosmač, T. (2010). Partial wick-debinding of low-pressure powder injection-moulded ceramic parts. *Journal of the European Ceramic Society*, *30*(15), 3013–3021. https://doi.org/10.1016/j.jeurceramsoc.2010.07.011

Gorjan, L., Dakskobler, A., & Kosmač, T. (2012). Strength evolution of injection-molded ceramic parts during wick-debinding. *Journal of the American Ceramic Society*, *95*(1), 188–193. https://doi.org/10.1111/j.1551-2916.2011.04872.x

Habibnejad-korayem, M., Zhang, J., & Zou, Y. (2021). Effect of particle size distribution on the flowability of plasma atomized Ti-6Al-4V powders. *Powder Technology*, *392*, 536–543. https://doi.org/10.1016/j.powtec.2021.07.026

Hamidi, M. F. F. A., Harun, W. S. W., Samykano, M., Ghani, S. A. C., Ghazalli, Z., Ahmad, F., & Sulong, A. B. (2017). A review of biocompatible metal injection moulding process parameters for biomedical applications. *Materials Science and Engineering: C*, *78*, 1263–1276. https://doi.org/10.1016/j.msec.2017.05.016

Hariramabadran Anantha, K. (2012). *Study of Total Oxygen Content and Oxide Composition Formed During Water Atomization of Steel Powders Due To Manganese Variation*. Royal Institute of Technology (KTH).

Hartwig, T., & Schroeder, R. M. (2012). Analysing Debinding and Sintering of Iron Feedstocks by Mass Spectrometry. *Proceedings of Powder Metallurgy World Congress 2012*, (May).

Hausnerová, B. (2010). Rheological characterization of powder injection molding compounds. *Polimery/Polymers*, *55*(1), 3–11. https://doi.org/10.14314/polimery.2010.003

Hausnerova, B., Kasparkova, V., & Hnatkova, E. (2016). Rheological and thermal performance of newly developed binder systems for ceramic injection molding. *AIP Conference Proceedings*, *1736*(November), 2–7. https://doi.org/10.1063/1.4949695

Hausnerova, B., Mukund, B. N., & Sanetrnik, D. (2017). Rheological properties of gas and water atomized 17-4PH stainless steel MIM feedstocks: Effect of powder shape and size. *Powder Technology*, *312*, 152–158. https://doi.org/10.1016/j.powtec.2017.02.023

Hayashi, K., & Lim, T. W. (1991). Role of equilibrium pressure of gas in sintering densification of carbonyl iron powder for metal injection molding. *Materials Transactions, JIM*, *32*(4), 383–388. https://doi.org/10.2320/matertrans1989.32.383

Hayat, M. D., Goswami, A., Matthews, S., Li, T., Yuan, X., & Cao, P. (2017). Modification of PEG/PMMA binder by PVP for titanium metal injection moulding. *Powder Technology*, *315*, 243–249. https://doi.org/10.1016/j.powtec.2017.04.004

Hayat, M. D., Jadhav, P. P., Zhang, H., Ray, S., & Cao, P. (2018). Improving titanium injection moulding feedstock based on PEG/PPC based binder system. *Powder Technology*, *330*, 304–309. https://doi.org/10.1016/j.powtec.2018.02.043

Hayat, M. D., Wen, G., Zulkifli, M. F., & Cao, P. (2015). Effect of PEG molecular weight on rheological properties of Ti-MIM feedstocks and water debinding behaviour. *Powder Technology*, *270*(Part A), 296–301. https://doi.org/10.1016/j.powtec.2014.10.035

Heaney, D. F. (2019). *Handbook of Metal Injection Molding*. Woodhead Publishing.

Hens, K. F., Lin, S. T., German, R. M., & Lee, D. (1989). The effects of binder on the mechanical properties of carbonyl iron products. *JOM*, *41*(8), 17–21.

Herranz, G., Nagel, R., Levenfeld, B., & Zauner, R. (2004). Powder Injection Moulding: Influence of the Powder Surface Treatment with Stearic Acid on Powder Injection Moulding of M2 HSS Using a HDPE Based Binder. *European Congress and Exhibition on Powder Metallurgy. European PM Conference Proceedings*.

Hidalgo, J., Jiménez-Morales, A., & Torralba, J. M. (2012). Torque rheology of zircon feedstocks for powder injection moulding. *Journal of the European Ceramic Society*, *32*(16), 4063–4072. https://doi.org/10.1016/j.jeurceramsoc.2012.06.023

Hnatkova, E., Hausnerova, B., & Filip, P. (2019). Evaluation of powder loading and flow properties of Al2O3 ceramic injection molding feedstocks treated with stearic acid. *Ceramics International*, *45*(16), 20084–20090. https://doi.org/10.1016/j.ceramint.2019.06.273

Ho, Y. L., & Lin, S. T. (1995). Debinding variables affecting the residual carbon content of injection-molded Fe-2 Pct Ni steels. *Metallurgical and Materials Transactions A*, *26*(1), 133–142. https://doi.org/10.1007/BF02669799

Hrubovčáková, M., & Harvanová, J. (2011). Influence of carbon content on oxides' reduction during sintering of Cr-Mo-C prealloyed steel. *Powder Metallurgy Progress*, *11*(1–2), 115–122.

Hsu, K. C., Lin, C. C., & Lo, G. M. (1996). The effect of wax composition on the injection molding of carbonyl iron powder with LDPE. *Canadian Metallurgical Quarterly*, *35*(2), 181–187. https://doi.org/10.1179/cmq.1996.35.2.181

Hu, F., Liu, W., & Xie, Z. (2016). Surface modification of alumina powder particles through stearic acid for the fabrication of translucent alumina ceramics by injection molding. *Ceramics International*, *42*(14), 16274–16280. https://doi.org/10.1016/j.ceramint.2016.07.164

Huang, M. S., & Hsu, H. C. (2009). Effect of backbone polymer on properties of 316L stainless steel MIM compact. *Journal of Materials Processing Technology*, *209*(15–16), 5527–5535. https://doi.org/10.1016/j.jmatprotec.2009.05.011

Hwang, K. S., Hsieh, C. H., & Shu, G. J. (2002). Comparison of mechanical properties of Fe-1.75Ni-0.5Mo-1.5Cu-0.4C steels made from PIM and press and sinter processes. *Powder Metallurgy*, *45*(2), 160–166. https://doi.org/10.1179/003258902225002569

Hwang, K. S., & Tsou, T. H. (1992). Thermal debinding of powder injection molded parts: Observations and mechanisms. *Metallurgical Transactions A*, *23*(10), 2775–2782. https://doi.org/10.1007/BF02651756

Industry Research. (2022). Iron Powder Market Size. Retrieved June 30, 2022, from https://www.globenewswire.com/en/news-release/2022/06/30/2471856/0/en/Iron-Powder-Market-Size-2022-2028-Global-Research-Business-Strategy-Industry-Share-Supply-Demand-Growth-Statistics-Growing-Trends-Top-Manufactures-Opportunity-Challenges-Regional-F.html

Japka, J., & German, R. (1992). Research development in carbonyl iron powders for MIM. *Metal Powder Report*, (May).

Ji, C. H., Loh, N. H., Khor, K. A., & Tor, S. B. (2001). Sintering study of 316L stainless steel metal injection molding parts using Taguchi method: Final density. *Materials Science and Engineering A*, *311*(1–2), 74–82. https://doi.org/10.1016/S0921-5093(01)00942-X

Johnson, J. L., & Heaney, D. F. (2006). Metal injection molding of Co-28Cr-6Mo. *Medical Device Materials III - Proceedings of the Materials and Processes for Medical Devices Conference 2005*, *2006*, 99–103.

Julien, B., & Després, M. M. (2006). *Metal Injection Moulding: A Near Net Shape Fabrication Method for the Manufacture of Turbine Engine Component*. *Cost Effective Manufacture via Net-Shape Processing*. Maetta Sciences Boucherville Quebec (Canada).

Kang, T. G., Ahn, S., Chung, S. H., Chung, S. T., Kwon, Y. S., Park, S. J., & German, R. M. (2012). *Handbook of Metal Injection Molding*. *Handbook of Metal Injection Molding*. https://doi.org/10.1533/9780857096234.2.197

Karatas, C., Kocer, A., Ünal, H. I., & Saritas, S. (2004). Rheological properties of feedstocks prepared with steatite powder and polyethylene-based thermoplastic binders. *Journal of Materials Processing Technology*, *152*(1), 77–83. https://doi.org/10.1016/j.jmatprotec.2004.03.009

Khakbiz, M., Simchi, A., & Bagheri, R. (2005). Analysis of the rheological behavior and stability of 316L stainless steel-TiC powder injection molding feedstock. *Materials Science and Engineering A*, *407*(1–2), 105–113. https://doi.org/10.1016/j.msea.2005.06.057

Kim, S. W., Lee, H. W., Song, H., & Kim, B. H. (1996). Pore structure evolution during solvent extraction and wicking. *Ceramics International*, *22*(1), 7–14. https://doi.org/10.1016/0272-8842(95)00025-9

Konttinen, Y. T., Milošev, I., Trebše, R., Van Der Linden, R., Pieper, J., Sillat, T., … Valdoltra, H. (2014). Metals for joint replacement. In *Joint replacement technology* (pp. 81–151). Elsevier. https://doi.org/10.1016/B978-1-84569-245-2.50006-8

Krindges, I., Andreola, R., Perottoni, C. A., & Zorzi, J. E. (2008). Low-pressure injection molding of ceramic springs. *International Journal of Applied Ceramic Technology*, *5*(3), 243–248. https://doi.org/10.1111/j.1744-7402.2008.02226.x

Krug, S., Evans, J. R. G., & Ter Maat, J. H. H. (2002). Reaction and transport kinetics for depolymerization within a porous body. *AIChE Journal*, *48*(7), 1533–1541. https://doi.org/10.1002/aic.690480716

Lamarre, S. G., Demers, V., & Chatelain, J. F. (2017). Low-pressure powder injection molding using an innovative injection press concept. *International Journal of Advanced Manufacturing Technology*, *91*(5–8), 2595–2605. https://doi.org/10.1007/s00170-016-9889-1

Lee, S. H., Choi, J. W., Jeung, W. Y., & Moon, T. J. (1999). Effects of binder and thermal debinding parameters on residual carbon in injection moulding of Nd(Fe, Co)B powder. *Powder Metallurgy*, *42*(1), 41–44. https://doi.org/10.1179/pom.1999.42.1.41

Leng, Y. (2008). *Materials Characterisation: Introduction to Microscopic and Spectroscopic Methods*. *Materials Characterization*. https://doi.org/10.1002/9780470823002.ch2

Lenk, R., & Krivoshchepov, A. (2004). Effect of Surface-Active Substances on the Rheological Properties of Silicon Carbide Suspensions in Paraffin. *Journal of the American Ceramic Society*, *83*(2), 273–276. https://doi.org/10.1111/j.1151-2916.2000.tb01184.x

Letenneur, M., Brailovski, V., Kreitcberg, A., Paserin, V., & Bailon-Poujol, I. (2017). Laser powder bed fusion of water-atomized iron-based powders: Process optimization. *Journal of Manufacturing and Materials Processing*, *1*(2), 1–17. https://doi.org/10.3390/jmmp1020023

Leverkoehne, M., Coronel-Hernandez, J., Dirscherl, R., Gorlov, I., Janssen, R., & Claussen, N. (2001). Novel binder system based on paraffin-wax for low-pressure injection molding of metal-ceramic powder mixtures. *Advanced Engineering Materials*, *3*(12), 995–998. https://doi.org/10.1002/1527-2648(200112)3:12<995::AID-ADEM995>3.0.CO;2-D

Li, Y., Huang, B., & Qu, X. (1999). Viscosity and melt rheology of metal injection moulding feedstocks. *Powder Metallurgy*, *42*(1), 86–90. https://doi.org/10.1179/pom.1999.42.1.86

LI, Y. min, LIU, X. quan, LUO, F. hua, & YUE, J. ling. (2007). Effects of surfactant on properties of MIM feedstock. *Transactions of Nonferrous Metals Society of China (English Edition)*, *17*(1), 1–8. https://doi.org/10.1016/S1003-6326(07)60039-9

Liberati, J. F., Araujo Filho, O. O., Monteiro, W. A., Esposito, I. M., Nogueira, R. A.,

Ambrosio Filho, F., & Ambrozio Filho, F. (2006). Low-Pressure Injection Molding Processing of AISI T15 High Speed Steel Powders. *Materials Science Forum*, *514–516*(PART 1), 569–573. https://doi.org/10.4028/www.scientific.net/MSF.514-516.569

Lin, S. T., & German, R. M. (1994). Interaction between binder and powder in injection moulding of alumina. *Journal of Materials Science*, *29*(19), 5207–5212.

Liu, D. M. (1999). Control of yield stress in low-pressure ceramic injection moldings. *Ceramics International*, *25*(7), 587–592. https://doi.org/10.1016/S0272-8842(98)00066-2

Ma, J., Qin, M., Tian, L., Zhang, L., Khan, D. F., Ding, X., … Zhang, H. (2015). Effect of Fe3P addition on magnetic properties and microstructure of injection molded iron. *Journal of Magnetism and Magnetic Materials*, *397*, 240–246. https://doi.org/10.1016/j.jmmm.2015.08.103

Ma, J., Qin, M., Wang, X., Zhang, L., Tian, L., Zhang, X., … Qu, X. (2014). Microstructure and magnetic properties of Fe-79%Ni-4%Mo alloy fabricated by metal injection molding. *Powder Technology*, *253*, 158–162. https://doi.org/10.1016/j.powtec.2013.11.011

Ma, J., Qin, M., Zhang, L., Zhang, R., Tian, L., Zhang, X., … Khan, D. F. (2013). Magnetic properties of Fe-50%Ni alloy fabricated by metal injection molding. *Materials and Design*, *51*, 1018–1022. https://doi.org/10.1016/j.matdes.2013.05.017

Ma, J., Qin, M., Zhang, L., Zhang, R., Tian, L., Zhang, X., & Qu, X. (2013). Preparation of high performance sintered soft magnetic alloy by metal injection molding. *Materials Chemistry and Physics*, *138*(2–3), 444–448. https://doi.org/10.1016/j.matchemphys.2012.12.083

Majdi, S. M., Tafti, A. A., Demers, V., Vachon, G., & Brailovski, V. (2022). Effect of powder particle shape and size distributions on the properties of low-viscosity iron-based feedstocks used in low-pressure powder injection moulding. *Powder Metallurgy*, *65*(2), 170–180. https://doi.org/10.1080/00325899.2021.1959696

Mangels, J. A. (1994). Low-pressure injection molding. *American Ceramic Society Bulletin;(United States)*, *73*(5).

Mangels, J. A., & Williams, R. M. (1983). Injection molding ceramics to high green densities. *American Ceramic Society Bulletin*, *62*(5), 601–606.

Mariot, P., Leeflang, M. A., Schaeffer, L., & Zhou, J. (2016). An investigation on the properties of injection-molded pure iron potentially for biodegradable stent application. *Powder Technology*, *294*, 226–235. https://doi.org/10.1016/j.powtec.2016.02.042

Marucci, M. L., & Corporation, H. (2018). Production of Powder Metallurgy Carbon and Low-Alloy Steels. *Powder Metallurgy*, *7*, 311–321. https://doi.org/10.31399/asm.hb.v07.a0006081

Materials, A. S. for T. and. (2015). *Standard test method for transition temperatures and enthalpies of fusion and crystallization of polymers by differential scanning calorimetry*. ASTM International.

Medvedovski, E., & Peltsman, M. (2012). Low pressure injection molding of advanced ceramic components with complex shapes for mass production. In *Advanced Processing and Manufacturing Technologies for Structural and Multifunctional Materials VI* (pp. 35–51). John Wiley & Sons, Inc. Hoboken, NJ, USA.

Metzner, A. B. (1985). Rheology of Suspensions in Polymeric Liquids. *Journal of Rheology*, *29*(6), 739–775. https://doi.org/10.1122/1.549808

Moghadam, M. S., Fayyaz, A., & Ardestani, M. (2021). Fabrication of titanium components by low-pressure powder injection moulding using hydride-dehydride titanium powder. *Powder Technology*, *377*, 70–79. https://doi.org/10.1016/j.powtec.2020.08.075

Moon, A. P., Dwarapudi, S., Sista, K. S., Kumar, D., & Sinha, G. R. (2021). Opportunity and challenges of iron powders for metal injection molding. *ISIJ International*. https://doi.org/10.2355/isijinternational.ISIJINT-2021-050

Moro, C., Francioso, V., & Velay-Lizancos, M. (2021). Modification of CO2 capture and pore structure of hardened cement paste made with nano-TiO2 addition: Influence of water-to-cement ratio and CO2 exposure age. *Construction and Building Materials*, *275*, 122131. https://doi.org/10.1016/j.conbuildmat.2020.122131

MPIF Standard. (1986). Determination of Density of Compacted or Sintered Metal Powders, 42. *Princeton, NJ*, 2–6.

Mukund, B. N., & Hausnerova, B. (2020). Variation in particle size fraction to optimize metal injection molding of water atomized 17–4PH stainless steel feedstocks. *Powder Technology*, *368*, 130–136. https://doi.org/10.1016/j.powtec.2020.04.058

Mukund, B. N., Hausnerova, B., & Shivashankar, T. S. (2015). Development of 17-4PH stainless steel bimodal powder injection molding feedstock with the help of interparticle spacing/lubricating liquid concept. *Powder Technology*, *283*, 24–31. https://doi.org/10.1016/j.powtec.2015.05.013

Mutsuddy, B. C., & Ford, R. G. (1995). *Ceramic injection molding* (Vol. 1). New York: Springer New York.

Neto, F. C., Giaretton, M. V., Neves, G. O., Aguilar, C., Tramontin Souza, M., Binder, C., & Klein, A. N. (2022). An Overview of Highly Porous Titanium Processed via Metal Injection Molding in Combination with the Space Holder Method. *Metals*. https://doi.org/10.3390/met12050783

Novak, S., Vidovič, K., Sajko, M., & Kosmač, T. (1997). Surface modification of alumina powder for LPIM. *Journal of the European Ceramic Society*, *17*(2–3), 217–223.

https://doi.org/10.1016/S0955-2219(96)00171-9

Omar, M. A., Ibrahim, R., Sidik, M. I., Mustapha, M., & Mohamad, M. (2003). Rapid debinding of 316 L stainless steel injection moulded component. *Journal of Materials Processing Technology*, *140*(1-3 SPEC.), 397–400. https://doi.org/10.1016/S0924-0136(03)00772-6

Pachauri, P., & Hamiuddin, M. (2016). Optimization of Debinding Process Parameters in Metal Injection Molding (MIM) for High Density of Sintered Parts. *Cloud Publications International Journal of Advanced Materials and Metallurgical Engineering*, *2*(1), 585. Retrieved from http://technical.cloud-journals.com/index.php/IJAMME/article/view/Tech-585

Park, J. M., Han, J. S., Gal, C. W., Oh, J. W., Kate, K. H., Atre, S. V., … Park, S. J. (2018). Effect of binder composition on rheological behavior of PMN-PZT ceramic feedstock. *Powder Technology*, *330*, 19–26. https://doi.org/10.1016/j.powtec.2018.02.027

Park, J. Y., Park, K. B., Kang, J. W., Kim, H. G., Hwang, N. M., & Park, H. K. (2020). Spheroidization behavior of water-atomized 316 stainless steel powder by inductively-coupled thermal plasma. *Materials Today Communications*, *25*(January), 101488. https://doi.org/10.1016/j.mtcomm.2020.101488

Patterson, B. R., & Aria, C. S. (1989). Debinding injection molded materials by melt wicking. *Jom*, *41*(8), 22–25. https://doi.org/10.1007/BF03220297

Rak, Z. S., & Z. S. Rak. (1999). New trends in powder injection moulding. *Powder Metallurgy and Metal Ceramics*, *38*(3), 126–132.

Rane, K. K., & Date, P. P. (2020). A dimensional analysis based model to predict completion of solvent debinding step for Metal Injection Moulded parts. *Advances in Materials and Processing Technologies*, *00*(00), 1–21. https://doi.org/10.1080/2374068X.2020.1759317

Rane, Kedarnath K., & Date, P. P. (2014). Rheological Investigation of MIM Feedstocks for Reducing Frictional Effects during Injection Moulding. In *Advanced Materials Research* (Vol. 966–967, pp. 196–205). https://doi.org/10.4028/www.scientific.net/amr.966-967.196

Rei, M., Milke, E. C., Gomes, R. M., Schaeffer, L., & Souza, J. P. (2002). Low-pressure injection molding processing of a 316-L stainless steel feedstock. *Materials Letters*, *52*(4–5), 360–365. https://doi.org/10.1016/S0167-577X(01)00422-0

Rishmawi, I., Salarian, M., & Vlasea, M. (2018). Tailoring green and sintered density of pure iron parts using binder jetting additive manufacturing. *Additive Manufacturing*, *24*(July), 508–520. https://doi.org/10.1016/j.addma.2018.10.015

Ritzhaupt-Kleissl, H. J. (2009). Ceramics Processing in Microtechnology. In *Applied Particle*

Technology Proceedings of an International Seminar (p. 7).

Royer, A., Barriere, T., & Bienvenu, Y. (2018). Influence of supercritical debinding and processing parameters on final properties of injection-moulded Inconel 718. *Powder Technology*, *336*, 311–317. https://doi.org/10.1016/j.powtec.2018.05.047

Rueda, M., Fulchiron, R., Cassagnau, P., Prebé, A., & Martin, G. (2016). Structuring of non-Brownian ferrite particles in molten polypropylene: Viscoelastic analysis. *Journal of Rheology*, *60*(6), 1245–1255. https://doi.org/10.1122/1.4963801

Rueda, M. M., Auscher, M. C., Fulchiron, R., Périé, T., Martin, G., Sonntag, P., & Cassagnau, P. (2017). Rheology and applications of highly filled polymers: A review of current understanding. *Progress in Polymer Science*, *66*, 22–53. https://doi.org/10.1016/j.progpolymsci.2016.12.007

Sajko, M., Kosmač, T., Dirscherl, R., & Janssen, R. (1997). Microstructure and mechanical properties of low-pressure injection-moulded reaction-bonded alumina ceramics. *Journal of Materials Science*, *32*(10), 2647–2654. https://doi.org/10.1023/A:1018618921415

Sardarian, M., Mirzaee, O., & Habibolahzadeh, A. (2017). Influence of injection temperature and pressure on the properties of alumina parts fabricated by low pressure injection molding (LPIM). *Ceramics International*, *43*(6), 4785–4793. https://doi.org/10.1016/j.ceramint.2016.11.208

Scheffer, K., Méheust, Y., Carvalho, M. S., Mauricio, M. H. P., & Paciornik, S. (2021). Enhancement of oil recovery by emulsion injection: A pore scale analysis from X-ray micro-tomography measurements. *Journal of Petroleum Science and Engineering*, *198*(June 2020). https://doi.org/10.1016/j.petrol.2020.108134

Shaw, C., Ph, D., Kulkarni, V. S., & Shaw, C. (2015). *Essential chemistry for formulators of semisolid and liquid dosages*. *Essential Chemistry for Formulators of Semisolid and Liquid Dosages*. Academic Press. https://doi.org/10.1016/c2013-0-18871-x

Shu, G. J., & Hwang, K. S. (2004). High density powder injection molded compacts prepared from a feedstock containing coarse powders. *Materials Transactions*, *45*(10), 2999–3004. https://doi.org/10.2320/matertrans.45.2999

Shu, J., & Koehler, L. (2017). The changing landscape of carbonyl iron and nickel powder production, 39–48.

Somasundram, I. M., Cendrowicz, A., Wilson, D. I., & Johns, M. L. (2008). Phenomenological study and modelling of wick debinding. *Chemical Engineering Science*, *63*(14), 3802–3809. https://doi.org/10.1016/j.ces.2008.04.040

Song-lin, L. I., Bai-yun, H., Yi-min, L. I., Du-xin, L. I., Jin-lian, F. A. N., & Feng, J. (2003). Effects of sintering atmosphere on the microstructure and mechanical property of sintered 316L stainless steel Experimental procedures tents of the thermal-debound and, *10*(1), 1–

6.

Song, S., & Peng, C. (2008). Viscosities of binary and ternary mixtures of water, alcohol, acetone, and hexane. *Journal of Dispersion Science and Technology*, *29*(10), 1367–1372. https://doi.org/10.1080/01932690802313006

Sotomayor, M. E., Várez, A., & Levenfeld, B. (2010). Influence of powder particle size distribution on rheological properties of 316L powder injection moulding feedstocks. *Powder Technology*, *200*(1–2), 30–36. https://doi.org/10.1016/j.powtec.2010.02.003

Standard, M., & Methods, T. (2016). *Standard Test Methods for Metal Powders and Powder Metallurgy Products*.

Standard Test Methods for Metal Powders and Powder Metallurgy Products. (2016). *Metal Powder Industries Federation*, 75–78.

Tafti, A. A., Demers, V., Majdi, S. M., Vachon, G., & Brailovski, V. (2021). Effect of Thermal Debinding Conditions on the Sintered Density of Low-Pressure Powder Injection Molded Iron Parts. *Metals* , *11*(2), 1–14. https://doi.org/10.3390/met11020264

Tafti, A. A., Demers, V., Vachon, G., & Brailovski, V. (2021). Effect of Binder Constituents and Solids Loading on the Rheological Behavior of Irregular Iron-Based Feedstocks. *Journal of Manufacturing Science and Engineering, Transactions of the ASME*, *143*(3), 1–12. https://doi.org/10.1115/1.4048268

Tavares, A. C., Mariot, P., Costa, L. L., & Schaeffer, L. (2019). Metal Injection Molding for Production of Biodegradable Implants : An Analysis of the Potential of Pure Iron for Application in Stents, *9*(2), 36–43. https://doi.org/10.5923/j.materials.20190902.02

Thomas-Vielma, P., Cervera, A., Levenfeld, B., & Várez, A. (2008). Production of alumina parts by powder injection molding with a binder system based on high density polyethylene. *Journal of the European Ceramic Society*, *28*(4), 763–771. https://doi.org/10.1016/j.jeurceramsoc.2007.08.004

Toy, Ç., Palaci, Y., & Baykara, T. (1995). A new ceramic thread-guide composition via low-pressure injection molding. *Journal of Materials Processing Tech.*, *51*(1–4), 211–222. https://doi.org/10.1016/0924-0136(94)01607-3

Tseng, W. J., Liu, D. M., & Hsu, C. K. (1999). Influence of stearic acid on suspension structure and green microstructure of injection-molded zirconia ceramics. *Ceramics International*, *25*(2), 191–195. https://doi.org/10.1016/S0272-8842(98)00024-8

Wallner, S. (2019). Powder Production Technologies. *BHM Berg- Und Hüttenmännische Monatshefte*, *164*(3), 108–111. https://doi.org/10.1007/s00501-019-0832-2

Wang, J. S., & Hon, M. H. (1999). Effect of amount of carbonyl iron powders on the sintering microstructure, and mechanical properties of Fe-4 Cu alloy synthesized using metal

injection molding. *Materials and Manufacturing Processes*, *14*(3), 435–446. https://doi.org/10.1080/10426919908914838

Wang, Q., Yin, H., Qu, X., & Johnson, J. L. (2009). Effects of mold dimensions on rheological of feedstock in micro powder injection molding. *Powder Technology*, *193*(1), 15–19. https://doi.org/10.1016/j.powtec.2009.02.001

Weir, F. E. (1963). Moldability of Plastics Based on Melt Rheology. Part 1-Theoretical Development. *Polymer Engineering and Science*, *3*(1), 32–36. https://doi.org/10.1002/pen.760030108

Wen, J., Liu, W., Xie, Z., Lou, C., & Yang, X. (2018). Effects of the binder compositions on the homogeneity of ceramic injection molded compacts. *Ceramics International*, *44*(3), 3218–3225. https://doi.org/10.1016/j.ceramint.2017.11.093

Williams, B. (2018). WORLDPM2018 Congress: Global MIM markets show healty grow. *Powder Injection Moulding International*, (Vol.12 No.4), 67–75. Retrieved from https://www.pim-international.com/powder-injection-moulding-international-magazine-archive/

Xianfeng, Y., Hehan, X., Qinglong, H., Zhe, Z., Xiewen, X., Li, Z., & Zhipeng, X. (2019). Study of thermal degradation mechanism of binders for ceramic injection molding by TGA-FTIR. *Ceramics International*, *45*(8), 10707–10717. https://doi.org/10.1016/j.ceramint.2019.02.142

Xiao, J., Zeng, X., Li, M., Dong, P., Wu, H., Xu, M., … Zhang, Y. (2019). Effect of pre-calcined ceramic powders at different temperatures on Ni-YSZ anode-supported SOFC cell/stack by low pressure injection molding. *Ceramics International*, *45*(16), 20066–20072. https://doi.org/10.1016/j.ceramint.2019.06.270

Xie, H., Jiang, J., Yang, X., He, Q., Zhou, Z., Xu, X., & Zhang, L. (2020). Theory and practice of rapid and safe thermal debinding in ceramic injection molding. *International Journal of Applied Ceramic Technology*, *17*(3), 1098–1107. https://doi.org/10.1111/ijac.13349

Yoon, T. S., Lee, Y. H., Ahn, S. H., Lee, J. H., & Lee, C. S. (2003). Effects of sintering conditions on the mechanical properties of metal injection molded 316L stainless steel. *ISIJ International*, *43*(1), 119–126. https://doi.org/10.2355/isijinternational.43.119

You, W. K., Choi, J. P., Yoon, S. M., & Lee, J. S. (2012). Low temperature powder injection molding of iron micro-nano powder mixture. *Powder Technology*, *228*, 199–205. https://doi.org/10.1016/j.powtec.2012.05.016

Zaky, M. T., Soliman, F. S., & Farag, A. S. (2009). Influence of paraffin wax characteristics on the formulation of wax-based binders and their debinding from green molded parts using two comparative techniques. *Journal of Materials Processing Technology*, *209*(18–19), 5981–5989. https://doi.org/10.1016/j.jmatprotec.2009.07.018

Zhang, L., Li, D., Chen, X., Qu, X., Qin, M., He, X., … Wang, J. (2015). Microstructure and mechanical properties of MIM213 superalloy. *Materials Chemistry and Physics*, *168*, 18–26. https://doi.org/10.1016/j.matchemphys.2015.09.043

Zhang, Y., Feng, E., Mo, W., Lv, Y., Ma, R., Ye, S., … Yu, P. (2018). On the microstructures and fatigue behaviors of 316L stainless steel metal injection molded with gas-and water-atomized powders. *Metals*, *8*(11). https://doi.org/10.3390/met8110893

Zorzi, J. E., Perottoni, C. A., & Da Jornada, J. A. H. (2002). Hard-skin development during binder removal from Al2O3-based green ceramic bodies. *Journal of Materials Science*, *37*(9), 1801–1807. https://doi.org/10.1023/A:1014949923939

Zorzi, Janete Eunice, Perottoni, C. A., & Jornada, J. A. H. da. (2003). Wax-based binder for low-ressure injection molding and the robust production of ceramic parts.

Zu, Y. S., Chiou, Y. H., & Lin, S. T. (1996). Performance of powder-injection-molded W-4.9Ni-2.1Fe components. *Journal of Materials Engineering and Performance*, *5*(5), 609–614. https://doi.org/10.1007/BF02646090